Transient Oxygen Consumption Rate Measurements with the BD™ Oxygen Biosensor System

by

CLARKE ALAN LOW

B.S., Chemical Engineering, Brigham Young University, 2005

Submitted to the Department of Chemical Engineering in partial fulfillment of the requirements for the degree of

Master of Science in Chemical Engineering

at the

Massachusetts Institute of Technology

August, 2008

Signature of Author .....
Department of Chemical Engineering
August 29, 2008

Certified by .....
Clark K. Colton
Professor of Chemical Engineering
Thesis Supervisor

Accepted by .....
William M. Deen
Professor of Chemical Engineering
Chairman, Departmental Committee for Graduate Students

Transient Oxygen Consumption Rate Measurements with the BD™ Oxygen Biosensor System

by

Clarke Alan Low

Submitted to the Department of Chemical Engineering on
August 29, 2008, in partial fulfillment of the requirements for the
Degree of Master of Science in Chemical Engineering

Oxygen consumption rate (OCR) is a reliable indicator of tissue health. Recently, the OCR of isolated human islets has been shown to predict transplant outcome in diabetic mice. The Oxygen Biosensor System (OBS) is a high-throughput, convenient assay that indirectly measures oxygen consumption by measuring oxygen partial pressure, pO_2, adjacent to tissue loaded into the OBS multiwell plate. Solving the general species transport equations for a steady-state solution has not accurately converted pO_2 measurements to OCR. Furthermore, the time to reach steady-state is prohibitively long (at least 5 hr). Transient OBS experiments have been conducted and the rate of pO2 change has been shown to correlate with the amount of viable tissue, however, no direct relation with OCR has been established.

The overall objective of this thesis was to accurately measure OCR using transient OBS measurements. I fabricated flat OBS plates to simplify the geometry for theoretical models, but theoretical simulations did not match well with experimental data. Furthermore, fabricated flat OBS plates did not behave experimentally as would be expected from 1-D, slab geometry. Simplified theoretical models were developed to qualitatively understand the effects of silicone rubber thickness, medium volume, and OCR density on the transient behavior of the OBS. It was shown that medium volume and OCR density should be increased as much as well-volume and tissue constraints allow. Commercial OBS plates were used for subsequent experiments, so it was unable to actively control silicone rubber thickness. Transient OBS measurements with both INS-1 cells and islets were correlated with stirred chamber OCR measurements conducted in parallel. The two measurements were linearly related and a calibration curve was developed so that OBS transient measurements could be converted to OCR. The relationship between the two measurements were similar enough for both cells and islets that the calibration curve seems to be independent of tissue geometry. Increased variability of islet tissue caused greater uncertainty about the islet prediction curve. This variability was compared with stirred chamber islet variability and islet sampling is hypothesized to be the underlying cause of high measurement variability with islets.

Acknowledgements

I would like to thank my advisor Clark Colton for requiring me to stay on for a few more months in the summer to conduct more research. Those last few months were an incredible learning experience for me and I am grateful that he did not let me take the easy way out by graduating prematurely. I am grateful for his willingness to meet regularly with me to help me learn how to analyze data without jumping to premature conclusions. I am grateful for his patience with me and that we finally hit our stride together and made it a very fruitful relationship for the last few months. I learned a lot over those final months and am amazed that the bulk of this thesis came from research over that time frame.

I am tremendously indebted to my fellow labmates in the Colton lab. Mike Rappel and Anna Pisania helped to introduce me to the world of islet research. Mike was particularly instrumental, together with Shenghan Yan (an MIT UROP), in introducing me to OBS. Kevin Brower, Michelle Lewis, and Jin Zhou always made coming to lab an enjoyable experience. I am especially indebted to Jeff Millman, my unofficial advisor, who entered the Colton lab together with me. Jeff is an extremely talented researcher and I am simply grateful that I sat across from him and learned from him how to design experiments and think about the scope of any project of experiment. I am grateful how willingly he spoke about his own research and used me as a sounding board because that really taught me to not rely entirely upon my own thinking, but to ask around for other's perspectives to strengthen my research.

I must briefly mention a few members of the chemical engineering department who helped in various technical aspects. I could ask Steve Wetzel any kind of question and he would usually have the answer for me. I am grateful for both his expertise and willingness to share it with students. Professor Daniel Blankschtein helped me better understand and appreciate surface tension forces. Andy Miller and Sal Bauxama helped with the surface modification of polystyrene. Bill Deen and Klaus Jensen helped me with some personal issues and I am grateful for their listening ears and their willingness to act to support me during my years at MIT.

Members of the Rubener / Cohen group trained me to use the video contact angle measurement equipment, camera, and software. Tadd Truscott, a Ph.D. candidate in ocean engineering helped with photography of meniscus profiles. Peter Morley in the MIT Machine Shop was a wonderful source of technical know-how as I searched for methods to characterize OBS geometry and fabricate flat OBS plates.

I am grateful to all of the islet centers and the ICR for shipped human islet tissue. I am especially grateful to Dr. Gordon Weir and Jennifer Hollister-Lock at Joslin diabetes center for providing me with rat islets at a moment's notice at the very last minute.

My parents, Gordon and Laurie, were instrumental in guiding me to graduate school and I am grateful for their continued support throughout the process. Their love, encouragement, and wisdom have been invaluable to me during some of the most difficult moments. I am grateful for their

continued confidence in me when I doubted myself. I also owe my dad an apology for not believing that a management consultant who last practiced engineering 25 years ago could help me finish my thesis in a different field of engineering. He helped me to see and focus on the big picture and almost all of the time was right on in his analysis.

Lastly, I am forever indebted to my dear wife, Anna, for her support. She has seen me through some of the most challenging years of my life and never lost faith in me. At times when I just wanted to quit, she believed in me and encouraged me to reach deep within myself to continue moving forward. And all the while she did this, she gave birth to our two wonderful children, Grant and Audrey. She happily lived in a 600ft^2 apartment and truly made it into a home where I could come to find refuge from the frustrations and uncertainty of research. Her sacrifices were tremendous over the past three years and she shares an equal (if not greater) part of the accomplishment of completing this thesis. Thank you Anna for helping (and sometimes even carrying) me through this and for recognizing that it was important for me personally to finish my thesis.

Contents

List of Figures

List of Tables

1. Introduction

Measurement of tissue oxygen consumption rate (OCR) gives information on the respiratory activity of a tissue sample and is a reliable indicator of mitochondrial function. Measurements of mitochondrial function, including OCR, have been shown to be sensitive to some of the earliest events in the cell-death process [1]. The ability to discriminate tissue that is not yet dead from viable tissue gives OCR a powerful predictive capability of future tissue viability. Measurement of OCR in islets of Langerhans is of great importance as it has been shown that OCR of human islets can be used to predict transplantation outcome in mice [2].

Islets are micro-organs embedded within the pancreas' exocrine tissues. There are approximately 1 million islets within the human pancreas and they account for 1-2% of the pancreas' volume. They are comprised of four primary cell types: α, β, γ-, and PP-cells as well as an extensive vasculature network. Islets are spheroid aggregates of cells that range in size from 30 - 400μm. By convention, an islet equivalent (IE) is defined as a perfectly spherical islet with 150 um diameter. Islets are micro-organs and efforts to characterize them do best to keep islets intact. Unfortunately, many techniques suitable for single cells are inapplicable for islets because of their 3-D geometry.

Islet transplantation is a promising treatment that has the potential to confer normoglycemia and insulin independence to type 1 diabetes mellitus (T1DM) patients. The establishment of the Edmonton protocol in 2000 marked a major breakthrough in clinical islet transplantation as an effective and feasible treatment and has since been implemented by 43 institutions worldwide [3, 4]. Widespread application requires standardized quality assessment measures to ensure *in vivo* efficacy [5, 6]. This is especially true because islet mass and viability is compromised during the somewhat harsh conditions from pancreas procurement to islet transplantation [7].

Early OCR measurements of islets were used to study glucose-stimulated insulin secretion. Because islets were scarce, sensitive Cartesian-divers were used to make measurements [8-11]. Subsequently Clark-type electrodes were used to make measurements in either perifusion systems [12-14] or continuously-stirred chambers [15]. The electrochemical sensor in microelectrode form was unstable and required frequent calibration, which rendered the procedure tedious. Large polarographic

sensors were stable but too large for islet measurements. The development of optical fiber sensors that rely on the effect of oxygen in altering the decay of fluorescent intensity following irradiation made possible rapid continuous, stable measurements of oxygen in solution [16]. Applications of fiber optic oxygen sensors have developed in three different directions: (1) perifusion bioreactors, (2) continuously stirred chambers, and (3) static culture devices.

Perifusion bioreactors and continuously-stirred chambers directly measure OCR by monitoring the partial pressure of oxygen, pO_2, at either different locations in a flow path for a perifusion reactor or over time in a stirred chamber and applying simple mass conservation equations to determine the rate of reaction of oxygen. Because both of these methods directly solve for OCR they are accurate and it is simple to determine OCR from pO_2 measurements. Perifusion systems have been employed to continuously monitor OCR over time together with measurements of insulin secretion and the redox state of cytochromes in the islet tissue [17]. While a perifusion system enables long-term culture and OCR tracking, it is an inherently complex system that requires considerable expertise and experience with its equipment, and is inefficient when multiple samples or replicates need to be measured in a short period of time. A stirred chamber was developed and tested with islets to yield rapid, precise, and accurate OCR measurements [18]. However, despite these advantages of stirred chamber measurements, it is still challenging to make multiple measurements in a short period of time unless multiple chambers are used in parallel.

Static culture devices do not remove tissue to an enclosed chamber, but rather maintain them in a micro-culture plate open to their culture environment. OCR measurements are made indirectly by directly measuring pO_2 in the bottom of the micro-culture plate and using oxygen diffusion equations to relate pO_2 to the flux of oxygen consumed by tissue. Monitoring of oxygen in microplate cultures has been an area of recent interest [19-28]. These platforms for measuring OCR in static culture are promising because they offer a platform for measuring oxygen consumption rates where multiple tissue samples can be assayed simultaneously (high throughput) and they typically utilize a fluorescent plate reader, which is equipment common and familiar to biological laboratories and researchers.

The BD™ Oxygen Biosensor Device (OBS) was developed for the measurement of OCR in static culture [29] and has been used for measurement of OCR for different cells lines [29, 30] and islet preparations [30, 31]. The OBS utilizes an oxygen sensitive fluorophor embedded in silicone rubber at the bottom of a well in a cell culture plate (typically a 96-well plate) upon which cells or tissue is placed

(Figure 1). A plate reader is used to determine the intensity of fluorescence at the bottom of each well, which is then related to the partial pressure of oxygen (pO_2) using the Stern-Volmer equation (Eq. 1).

(Eq. 1) $$\frac{I}{I_0} = 1 + K_{SV} pO_2$$

The tissue OCR is determined by applying the oxygen species conservation equation with two known boundary conditions: (1) pO2 at the gas-liquid interface, and (2) pO_2 at the bottom of each well based on fluorescence intensity. To enable computation of the OCR from only these two boundary conditions, several simplifying assumptions are necessary including (1) the system is at steady state, (2) the well geometry is perfectly cylindrical, (3) the wells are fabricated from oxygen impermeable material, (4) the medium is completely stagnant, (5) there is a uniform and infinitely thin cell layer, and (6) the sensor-embedded silicone rubber is uniform and infinitely thin.

Measurements by the OBS for islet tissue resulted in an OCR of approximately 800 fmol/min IE [32] or about 0.5 fmol/min cell (1560 cell per IE [1]), which is much lower than average values for islets measured in our laboratory using the stirred-chamber system. Similarly, values for CHO cells of 0.5 fmol/min cell measured in the OBS are an order of magnitude lower than what is found in a commercial respirometer [33].

Rappel investigated several of the assumptions invoked in the OBS to determine whether inaccurate assumptions were leading to inaccurate OCR calculations [34]. Theoretical models were constructed to evaluate the sensitivity of oxygen transport to relaxing assumptions about tissue and oxygen sensor thickness, and oxygen impermeability of polystyrene sidewalls and bottom. Experiments demonstrated that medium is not stagnant and that the assumption of quiescent medium introduces a significant error into OCR measurement. The use or larger-diameter culture wells also significantly improved the accuracy of OCR measurements, although the underlying basis for this effect was not determined. Although Rappel was able to improve the accuracy of OCR measurements using the OBS plate, the method was cumbersome and took 2 days to complete. Previous data from our lab suggested that the time to reach steady-state is at least 5 hours and this is a significant inconvenience.

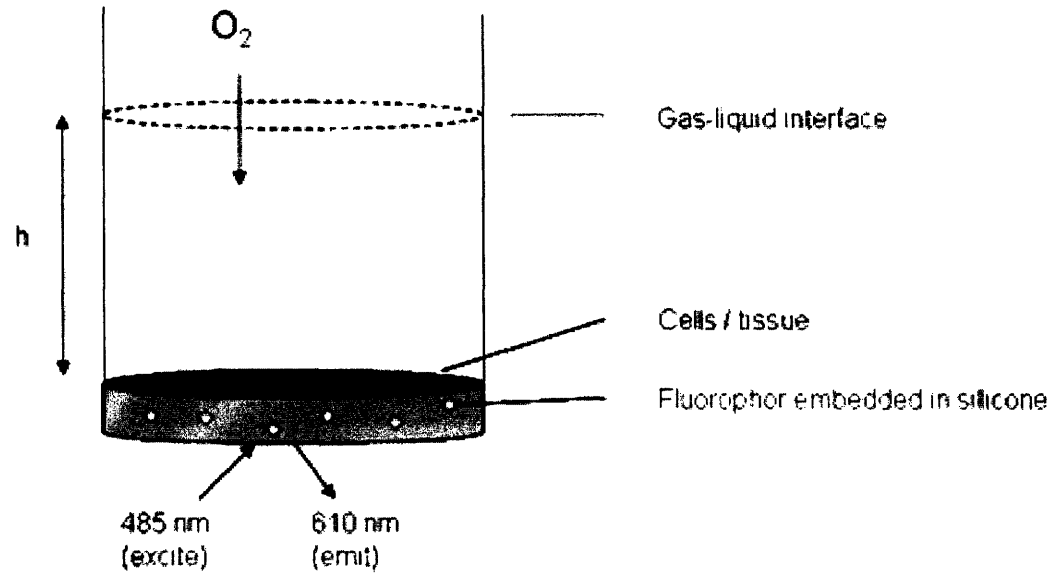

Figure 1.1. Diagram of OBS device.

The OBS has also been used for transient studies of cells [30] and islets [31] where it is not necessary for the system to reach steady-state conditions. Such transient experiments offer the conveniences of a high-throughput platform and can be performed in typically less than 2 hr. The rate of pO_2 decrease when tissue is added has been correlated with the amount of tissue loaded and taken to be a marker of tissue OCR. However, it is important to mention that this empirically-observed decrease in pO_2 has not been directly linked via oxygen transport theory to the physical phenomenon of tissue consuming oxygen. Therefore this rate of pO_2 decrease is an experimental measure that does not relate to any other methods of OCR measurement and can only be used for measuring viability relative to a control or another sample.

This research project was based on the hypothesis that transient OBS measurements of cells and islet tissue could accurately measure oxygen respiration as a marker of tissue viability in a high-throughput, convenient manner. The transient measurement was chosen because the long time necessary to reach steady-state in the OBS device makes steady-state measurements prohibitive for everyday use.

The first section of this thesis further characterizes OBS geometry to determine whether deviations from 1-D geometry introduce significant errors and hinder the capability of theoretical models to accurately simulate or predict transient experimental results. Additionally, we will discuss

efforts to construct flat OBS plates that would have 1-D geometry and be more amenable to theoretical modeling.

The second section utilizes theoretical models to explore the effect of various OBS parameters and their effect on transient behavior. The models are not intended to accurately match experimental data, rather qualitatively describe behavior so that parameters may be tuned so as to improve transient measurements and make them more amenable to data analysis.

The last section describes a new, systematic approach to analyzing transient OBS data and compares it with an established method. Transient OBS data will also be correlated with an accurate measurement of OCR using the stirred chamber to investigate any relationship that may enable the conversion of transient OBS measurements into absolute OCR measurements.

2. Characterization and Evaluation of OBS Plate Geometry

2.1 Introduction

The initial intended use of the OBS was to measure tissue OCR at steady-state conditions [29]. In order to easily compute OCR using Fick's Second Law several simplifying assumptions are required including (1) the system is at steady-state, (2) the wells are fabricated from oxygen impermeable material, (3) the medium is completely stagnant, (4) there is a uniform and infinitely thin cell layer, at the bottom, overlaying (5) a uniform infinitely thin oxygen sensor material. When these assumptions are invoked the OBS well is simplified to a 1-D slab of quiescent medium through which oxygen diffuses. The flux of oxygen through the medium can be easily computed from the known ambient pO_2 and the pO_2 measurement obtained via the oxygen sensitive fluorophor at the bottom of the OBS well. The degree to which these assumptions are valid affects the accuracy of OCR estimation using the OBS system.

Rappel [34] evaluated several of these assumptions for the steady-state case and showed that the medium is not completely stagnant and that assuming quiescent medium introduces a large error in OCR estimates. Experimental data showed that increasing well radius affected the OCR estimation, which initially indicated oxygen transport through the polystyrene bottom and sidewalls, however, subsequent experiments with glass wells did not confirm this reasoning. Tissue and oxygen sensor thickness were shown to be insignificant when estimating OCR.

An additional assumption not initially identified is that the medium and silicone rubber are assumed to be flat slabs of constant thickness. This assumption is necessary in order to assume 1-D geometry. If any of the phases exhibit curvature, then the oxygen transport problem becomes a 2-D problem with axial symmetry, which may lead to inaccurate estimations of OCR at steady-state and confound efforts to theoretically model transient OBS measurements.

This chapter discusses how the geometric shape of both the silicone rubber and medium were characterized so that theoretical models could be constructed to evaluate the magnitude effect of assuming a flat geometry when the actual geometry is curved. Also discussed are efforts to fabricate

OBS plates with flat, 1-D geometry and subsequent cell-free experiments to test whether the observed behavior of the fabricated well was consistent with expected results for 1-D geometry,

2.2 Methods

2.2.1 Fabricating OBS Plates

Oxygen sensor particles were made by adsorbing 75 mg 4,7-diphenyl-1,10-phenanthioline ruthenium (Alfa Aesar, CAS#: 36309-88-3, Ward Hill, MA) dissolved in 25 ml ethanol onto 11.5 g of silica gel powder (Sigma Aldrich, Catalog no: 23,675-6, St. Louis, MO). The mixture was placed in a glass desiccant chamber connected to a vacuum pump and dried over several days to form a fine powder after which it was stored at -20°C.

For every 6.5 g of silicone elastomer base (Dow Corning, Sylgard, Catalog no: 3097366-0503, Midland, MI) roughly 1.4 g of dried oxygen particles and 0.65 g of the curing agent (Dow Corning, Sylgard, Catalog no: 3097358-0503) were used to make the silicone rubber/sensor mixture. After mixing all three components such that no large clumps of the oxygen sensor particles were present, the mixture was dispensed into either a 96-well tissue culture treated plate with flat bottom wells (Becton Dickinson, Catalog no: 353072, Franklin Lakes, NJ) or a 100 mm square polystyrene Petri dish (Becton Dickinson, Catalog no: 351112). 20 ul of mixture was dispensed into the 96-well plate via a 1 ml syringe (Becton Dickinson, Catalog no: 309602), while 5 ml of mixture was dispensed into the square dish using a 5 ml syringe (Becton Dickinson, Catalog no: 301603). After adding the mixture any remaining visible clumps of undissolved powder were removed using a 200 µl pipette. The mixture was spread to all edges of the well or dish and allowed to cure on a level surface at either room temperature for 2 days or 50 °C in an oven for 4 hours.

The cured slab of oxygen sensor and silicone rubber mixture was removed from the square Petri dish and cut into flat circular discs with a 6mm ID steel hole punch (MIT Machine Shop, Cambridge, MA). Discs were cut from the center of the slab to avoid edges where surface tension forces pulled the silicone rubber up the polystyrene wall. This ensured that discs were of a constant thickness. Multiple discs were aligned, stacked, and pressed on top of each other to form slabs thicker than the original slab thickness. Wells in a 96-well plate were either left empty or prepared with a small 2 ul liquid silicone rubber drop to help seal the disc to the well-bottom. The silicone rubber was composed of 80% silicone elastomer base, 10% curing agent, and 10% Dow Corning® 200 Fluid 20cS (Sigma Aldrich, Catalog no:

378348), which was added to reduce the viscosity of the liquid silicone rubber mixture. Discs were inserted to the bottom of the well and pushed to expel any air bubbles or liquid silicone rubber between the disc and well-bottom. The plates were placed in a 50°C oven for 4 hours to cure the liquid silicone rubber.

2.2.2 Geometric Characterization of Oxygen Sensor Discs

An eyeglass screwdriver was used to detach the cured oxygen sensor and silicone rubber mixture from the bottom of three types of 96-well OBS plates: (1) commercially available Becton Dickinson round bottom well plates (BD Biosciences, Catalog No: 353830), (2) fabricated flat bottom well plates with liquid oxygen sensor added and subsequently cured, and (3) fabricated flat bottom well plates with cured, cut discs inserted into the bottom of the well (either with or without 2 ul silicone rubber to seal the disc to the bottom). These silicone rubber discs were examined to ensure that the detachment process didn't drastically alter its shape. The thickness of the disc was measured initially with a dial caliper (Mitutoyo, Aurora, IL) and subsequently by cutting a thin cross-section of the disc and measuring the height profile with an optical comparator (Sigma HB400, Quadra Check 2000, Starrett, Athol, MA). The cross section was placed on a stage, where its profile was projected onto a screen with crosshairs. The stage was moved to take measurements of the disc's height along the width of the cross section.

More detailed analysis of silicone rubber discs was performed using high resolution photographs of silicone rubber disc cross sections using the camera of a video contact angle system (VCA Optima Surface Analysis System, AST Products, Billerica, MA). The diameter of the disc exceeded the camera's field, so two pictures were taken and then stitched together using freeware image editing software (GIMPshop, 2.2.8). Images were then analyzed using freeware image analysis software (ImageJ 1.40, NIH, Bethesda, MD) to profile the disc dimension using at least 20 point measurements. Individual points were entered into COMSOL (COMSOL Inc, Burlington, MA) to define a solid object, which was then meshed and solved for to determine the total volume of the disc.

2.2.3 Surface Modification of OBS plates

96-well plates were treated to increase the hydrophobicity of the polystyrene so as to decrease its attraction for water to remove the meniscus formed between the air-liquid interface whenever water or cell culture medium were added to the well. The plates were treated in two different manners to modify their surface chemistry. For the primary treatment, plates were placed in a sealed 2L Tupperware® container (Rubbermaid, Sandy Springs, GA) containing open vials of 1H,1H,2H,2H-Perfluorodecylytriethoxy Silane (Alfa Aesar, Catalog no: L16585) for 20 hours in an oven at approximately 80°C. At the elevated temperature the vapor pressure of the silane is sufficient to evenly deposit a thin layer of hydrophobic silane on all surfaces within the sealed container. Alternatively, perfluorodecyl acrylate (Aldrich, Catalog no: 474487) was deposited onto the plate surface in an initiated chemical vapor deposition process as described earlier [35]. Briefly, perfluorodecyl acrylate and tert butyl peroxide vapors were metered at 0.5 sccm and 1.3 sccm, respectively, into a custom-built vacuum chamber at 100 mtorr. Tungsten filaments heated to 300 deg C thermally decomposed the peroxide initiator into radicals, which reacted with the acrylate monomer at a substrate stage maintained at 35 deg C. The film growth was tracked via interferometry and was terminated at a film thickness of 100 nm.

The hydrophobicity of the modified surfaces was quantified by measuring the contact angle (VCA Optima Surface Analysis System, AST Products). Briefly, phosphate buffered saline (PBS, Mediatech, Herndon, VA) was loaded into a precision controlled syringe whose needle rests above a stage. A sample of the modified surface was placed on the stage and the syringe is carefully depressed to form a droplet of water at its tip. The stage was moved toward the needle tip and the droplet of water is removed from the needle tip and rests on the modified surface. A picture of the water droplet was taken and analyzed to determine the contact angle.

Side-angle pictures of the meniscus formed between PBS and air in standard and modified 96-well plates were taken with a Canon Rebel XT with a Nikon close-zoom lens.

2.2.4 Dry, Transient OBS Experiments in Flat-disc Plates

Fabricated OBS plates with wells containing one, two, and four flat discs (n=4 for each thickness) where wells were empty or pre-filled with 2 ul silicone rubber as described previously were placed

within a humidified flush box connected to a nitrogen gas cylinder (Airgas, Radnor, PA). No liquid medium was present in any well. The flush box was housed within a 37°C incubator to mimic cell culture conditions. The nitrogen gas line bubbled through a sealed bottle of DI water in order to humidify the gas before reaching the flush box containing OBS plates. The gas was initially bubbled vigorously into the DI water for 15 minutes to rapidly displace any oxygen present in the flush box. After 15 minutes the flow rate was decreases to a steady stream of small bubbles in the DI water. OBS plates were kept within the flush box over 2 days to ensure that all oxygen was removed from the 96-well plates.

A fluorescent plate reader (POLARstar, BMG LabTechnologies) was pre-warmed to 37°C for 10 – 15 min before the plates were removed from the flush-box and immediately placed within the plate reader. Both excitation (485 nm) and emission (630nm) were directed from underneath the OBS plate to increase proximity of reading to the oxygen sensitive particles embedded within the silicone rubber. Fluorescent measurements were taken every 30 seconds for a total of 200 measurements.

Calculation of pO_2

Intensity measurements were converted to partial pressure of oxygen, pO_2, using the one parameter Stern-Volmer equation

Eq. 2.1
$$\frac{I_0}{I} = 1 + K_{SV}[pO_2]$$

where I_0 is the intensity measurement when no oxygen is present, I is the intensity resulting from the existing pO_2, and K_{SV} is the Stern-Volmer constant, which would be determined for each well by making two intensity measurements: (1) a zero oxygen measurement, I_0 ,and (2) an ambient oxygen measurement, I_{amb}. An oxygen quenching 0.1M sodium sulfite solution (EMD chemicals, Gibbstown, NJ; 0.126 g in 10ml PBS) was prepared and added to each well (200ul) to obtain a zero oxygen intensity reading. Measurements were taken every 5 minutes for a total of 200 measurements. Fluorescent intensity increased as pO_2 decreased in the system until finally reaching a plateau when all oxygen had been quenched from the well. The average intensity of this plateau region for each well was used as the zero oxygen intensity measurement, I_0. The ambient oxygen measurement, I_{amb}, was taken at the end of the dry, transient experiment when the OBS well had equilibrated with ambient conditions. The Stern-Volmer constant, K_{SV}, was determined by rearranging the Stern-Volmer equation

Eq. 2.2
$$K_{SV} = \frac{\frac{I_0}{I} - 1}{[pO_2]}$$

Normalized intensity measurements, I_0/I, were converted to partial pressure, pO_2, by rearranging the Stern-Volmer equation

Eq. 2.3
$$[pO_2] = \frac{\frac{I_0}{I} - 1}{K_{SV}}$$

2.2.5 Theoretical Simulations

Theoretical models for oxygen transport were created to simulate both dry transient experiments and to explore the effect of non 1-D geometry on a transient experiment with tissue present. All models neglected the effect of convection and the species conservation equation for O_2 in the absence of convection is given by

Eq. 2.4
$$\frac{\partial c}{\partial t} = D\nabla^2 c + R$$

where c is the concentration of oxygen, D is the diffusivity of oxygen and is assumed to be isotropic, and R is the homogeneous generation term for oxygen, which was neglected in all models as any tissue was assumed to be infinitely thin and therefore oxygen generation (or disappearance) was dictated by a boundary condition.. For convenience, the concentration terms in Eq. 2.4 are replaced with oxygen partial pressure, p, using

Eq. 2.5
$$c = \alpha pO_2$$

where α is the Bunsen solubility coefficient of oxygen. We assume that within each phase the solubility is constant so that Eq. 2.4 becomes

Eq. 2.6
$$\alpha \frac{\partial pO_2}{\partial t} = (D\alpha)\nabla^2 pO_2$$

where (Dα) is the permeability of oxygen.

This general equation describes oxygen transport in each phase of the systems (medium, silicone rubber, tissue, plate walls). All theoretical models neglected transport within the tissue and

plate walls and only considered the medium and silicone rubber domains. At the interface between these two phases, the following condition must be satisfied

Eq. 2.7
$$p_{O_2,1} = p_{O_2,2}$$

where the subscripts denote different phases of the system. The convenience of using the equations with partial pressure instead of concentration is that partial pressure is constant across any interface, while concentration changes due to solubility differences between the phases. Additionally, unless specified otherwise, the interface between any two phases is also subject to the condition that the normal flux leaving one phase is equal to the normal flux entering the second phase

Eq. 2.8
$$n \cdot (-(D\alpha)\nabla pO_2)_1 = n \cdot (-(D\alpha)\nabla pO_2)_2$$

where n is the unit vector normal to the interface between phases.

Models for were constructed and solved using these general equations in the commercially available software COMSOL Multiphysics 3.4 (COMSOL Inc., Burlington, MA). For 1-D models, its geometric mesh contained more than 100 nodes, while 2-D models contained more than 1000 nodes. Parameter values input into the simulation models are given in Table 1. The relative error estimated by the finite element software in the solution vector for concentration, which takes into account the current and previous solution in the iterative solver was constrained to be less than 10^{-6}. Details about the geometry, boundary and initial conditions for each experimental simulation are given below.

The average partial pressure of oxygen within the silicone rubber, $<pO_2>_{si}$, was determined by integrating pO_2 over the volume of silicone rubber and normalizing by its volume, as given by

Eq. 2.9
$$< pO_2 >_{si} = \frac{\int_V pO_2 dV}{\int_V dV}$$

where rather than writing multiple integrals for each dimension, the integral has been simplified to a volume integral over the whole volume of silicone rubber. The average partial pressure within the silicone rubber was thought to represent the pO_2 that is indirectly measured via the fluorescent intensity measurement of the oxygen-sensitive sensor embedded within the silicone rubber

Dry, Transient Simulations in Flat-disc OBS Plates

1-D models of silicone rubber were designed to simulate dry, transient experiments conducted with the fabricated, flat-disc OBS plates. The thickness of the silicone rubber disc was matched to the experimental thicknesses. The initial condition of the silicone rubber was complete anoxia to mimic the anoxic condition of the OBS plate within the nitrogen-purged flush-box,

Eq. 2.10 $$pO_2(z,0) = 0$$

where z is any distance along the cylindrical axis of the silicone rubber disc. The pO_2 at the top surface of the silicone (z=h) is specified as the ambient partial pressure oxygen,

Eq. 2.11 $$pO_2(h,t) = pO_{2,amb}$$

where h is the specified height of the silicone rubber slab and t is any possible time. The bottom of the silicone rubber disc (z=0) is in contact with the polystyrene well and is therefore modeled as possessing an insulating boundary,

Eq. 2.12 $$\frac{\partial pO_2}{\partial z}(0,t) = 0$$

The solver was specified to solve for pO_2 at every node at time intervals of 5 seconds.

Evaluating Effects of non-ideal Geometry

The magnitude of assuming 1-D, slab geometry when in reality the OBS system possesses curved interfaces was evaluated by creating models of the ideal geometry and comparing the transient response with models created with 2-D, curved interfaces. Two different non-ideal geometries were evaluated: (1) the effect of curved oxygen sensor/silicone rubber at the well bottom and (2) the effect of a meniscus at the air-medium interface. While one of these geometries was evaluated, the other was specified as an ideal, 1-D interface.

These models contained a silicone rubber phase and a stagnant, liquid medium phase, where a flux discontinuity existed at the interface between the two phases. Oxygen transport within

each phase was described by the general species equation, Eq. 2.6. The flux discontinuity at the interface represented an infinitely thin layer of tissue consuming oxygen according to Michaelis-Menton kinetics and was expressed as the boundary condition

Eq. 2.13
$$-n \cdot (N_1 - N_2) = \frac{\left(\frac{OCR}{A_i}\right) pO_2}{K_m + pO_2}$$

where OCR is the total oxygen consumption rate of the tissue in the well, A_i is the area of the interface, K_m is the Michaelis-Menton constant for oxygen consumption in tissue, and N_i is the flux of oxygen at the boundary in phase i and is expressed by

Eq. 2.14
$$N_i = -(D\alpha)_i \nabla pO_2$$

The boundary condition at r=0 was specified as an axis of symmetry,

Eq. 2.15
$$\left.\frac{\partial pO_2}{\partial r}\right|_{r=0} = 0$$

The boundary condition at r=R where both the silicone rubber and liquid medium interface with the oxygen-impermeable polystyrene was expressed as

Eq. 2.16
$$\left.\frac{\partial pO_2}{\partial r}\right|_{r=R} = 0$$

All other boundary conditions were similar to those described for the dry, transient models, except that whereas before each condition was specified at a particular height for the 1-D model it was specified along the entire 2-D interface. These included the insulation condition at the bottom of the silicone rubber where it contacts the polystyrene (see Eq. 2.12) and the constant ambient oxygen condition where the liquid medium contact the air (see Eq. 2.11). The initial condition was specified so that all phases were equilibrated with ambient oxygen

Eq. 2.17

$$pO_2\big|_{t=0} = pO_{2,amb}$$

The curved silicone rubber model was created by specifying measured points from the commercial OBS device. The volume of silicone rubber was determined by integrating within COMSOL and found to be 7.6 ul. This model was compared to an ideal, 1-D model with a flat slab of silicone, whose volume was equal so that any differences between the two models would be attributable to geometry and not total volume of silicone rubber. The height of the flat slab was determined by dividing the volume of silicone rubber by the area of the well bottom as give by

$$h_{s,eq} = \frac{V_s}{\pi R^2}$$

Eq. 2.18

$$= 0.024cm$$

To obtain an order of magnitude estimate for the effect of the meniscus, theoretical models were built that assumed the maximum physically possible curvature where the meniscus was perfectly hemispherical in shape. This limiting case assumed that the liquid medium completely wetted the wall (contact angle, $\theta = 0$) and that the presence of gravity could be neglected in the crown of the meniscus. Although these assumption are typically only valid for very small capillary diameters and are visibly not true in our 96-well plate, the use of this maximum allowable curvature was useful to provide an order of magnitude estimate. Models with the hemispherical meniscus were compared with models of the same volume liquid media, but with a flat gas-medium interface. Both models included 7.6 ul, flat silicone rubber.

All models contained a silicone rubber volume of 7.6 ul and a liquid medium volume of 200 ul. Only the shapes of the phases were varied to investigate the effect of curved geometries. The total OCR in the wells was varied from 0.1 – 1 nmol/min.

Table 2.1. Parameters used in theoretical simulations for oxygen transport in OBS wells

Parameter	Symbol	Value	Units	Reference
Michaelis constant	K_m	0.44	mmHg	Wilson et al. 1988
O2 diffusivity - medium	D_m	2.78 x 10-5	cm2/s	Avgoustiniatos 2001
O2 diffusivity - silicone rubber	D_s	2.17 x 10-5	cm2/s	Colton 1971
O2 solubility - medium	α_m	1.27 x 10-9	mol/cm3 mmHg	Avgoustiniatos 2001
O2 solubility - silicone rubber	α_s	12.1 x 10-9	mol/cm3 mmHg	Colton 1971
Well radius	R	0.3175	cm	Manufacturer Specifications
Ambient oxygen	pO_2	160	mm Hg	
Volume silicone rubber	V_s	0.0076	cm^3	
Volume liquid medium	V_m	0.200	cm^3	

2.3 Results

2.3.1 Geometry of Oxygen Sensor / Silicone Rubber in OBS Plates

The fluorophor-embedded silicone rubber sensors were removed from the bottom of commercial and fabricated OBS devices, cut into thin cross-sections and imaged to profile sensor geometry. Additionally, silicone rubber discs cut from the flat slab in the square Petri dish were also cut into thin cross sections and imaged. The silicone rubber from commercial OBS plates (Figure 2.1A) were thickest in the center of the well where the liquid silicone rubber presumably pooled at the bottom of the round-bottom before curing. The hemispherical shape of the round-bottom well is apparent from the bottom edge of the cross-section. Silicone rubber from fabricated flat-bottom OBS plates (Figure 2.1B), on the other hand, utilized a flat-bottom well in an effort to simplify geometry of the silicone

rubber sensor. However, although the bottom edge of the cross section conformed to the shape of the well and was observably flat, the top surface exhibited curvature. Capillary forces pulled the liquid silicone rubber mixture up at the well's edge so that the disc was thinner at the center of the well than at the edge. Flat silicone rubber discs cut from the square Petri dish slab (Figure 2.1C) were flat across both the bottom and top edges. It was also observed that significant bowing or slanting of the edges were probably indications that the knife deformed the disc edges during the cutting process. This deformation became less significant when cutting thinner discs.

Commercial OBS sensors also exhibited a distinct band where the oxygen sensor fluorophor was present (the black band running along the bottom of the cross section in Figure 2.1A) and a more transparent section of silicone rubber where no oxygen sensor was visibly present. This phenomenon was not observed in OBS plates fabricated within our lab where the fluorophor was homogeneously dispersed throughout the silicone rubber. Possible differences in silicone rubber formulation (specifically viscosity) might explain why the fluorophor settled to the bottom of the silicone rubber in the commercial device, whereas fluorophor particles remained dispersed throughout the curing process in our lab. The effect of this localization of the oxygen sensor particles to the bottom edge of the silicone rubber was evaluated using theoretical models and will be discussed later.

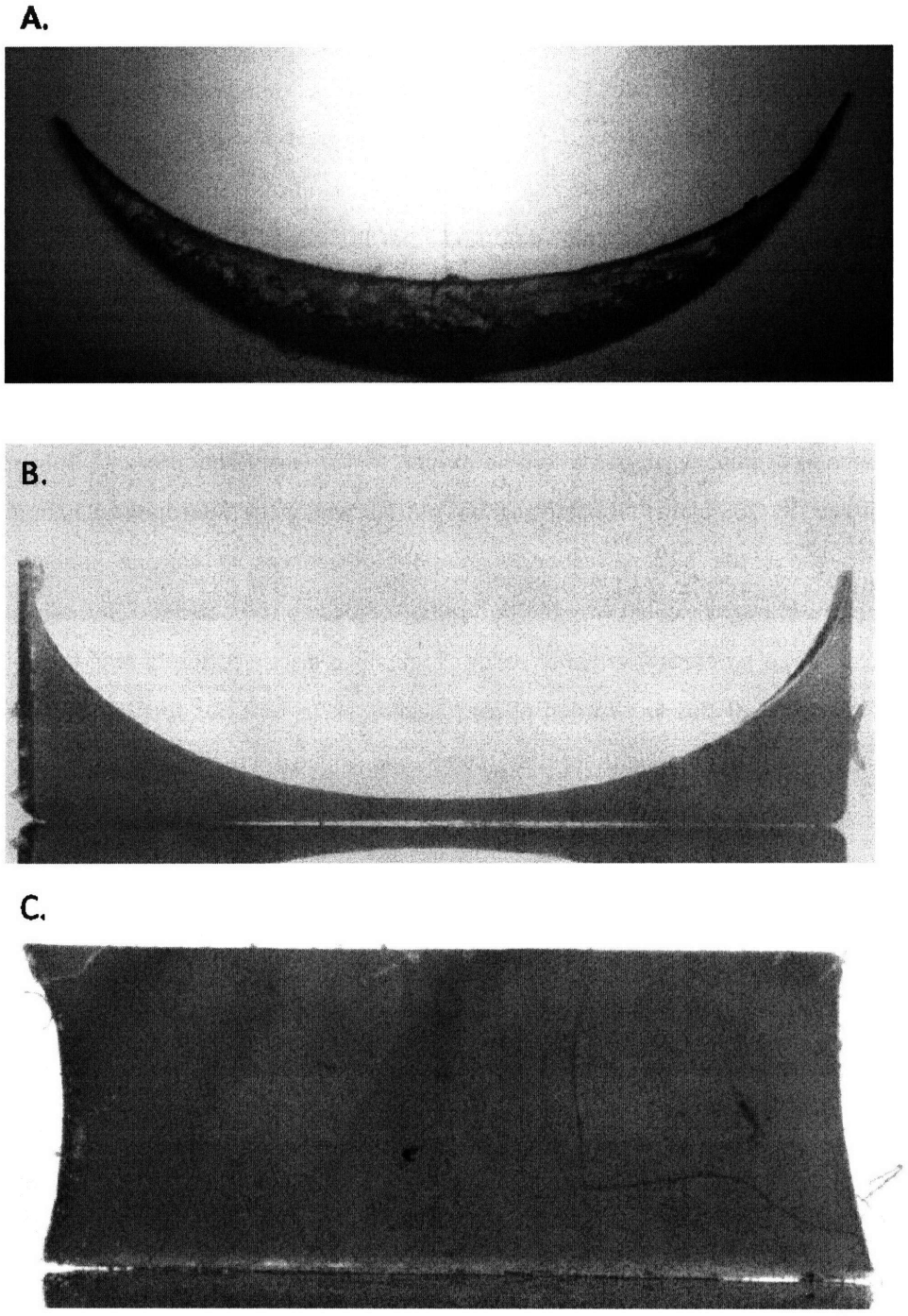

Figure 2.1. Cross-section of oxygen sensor / silicone rubber disc from (A) round-bottom commercial OBS plate, (B) flat bottom fabricated OBS plate, and (C) flat disc cut from square Petri dish slab. Please note that the diameter of all cross sections are approximately equivalent, but that the volume of silicone rubber varies dramatically, particularly for the flat disc(C), which is significantly larger than either of the other silicone rubber discs.

2.3.2 Modification of Polystyrene Surface to Minimize Air-Liquid Meniscus

The interface between the liquid medium and air within the well of an OBS plate (either commercial or fabricated within the Colton lab) formed a highly curved surface as a result of surface tension effects and interactions with the polystyrene side walls (Figure 2.2). The meniscus increased the surface area of the liquid-air interface, which increased oxygen transport from the gas phase into the medium. Additionally, the curvature made the geometry of the system more complex and contradicted previous assumptions about the system geometry where the liquid-air interface was assumed to be flat.

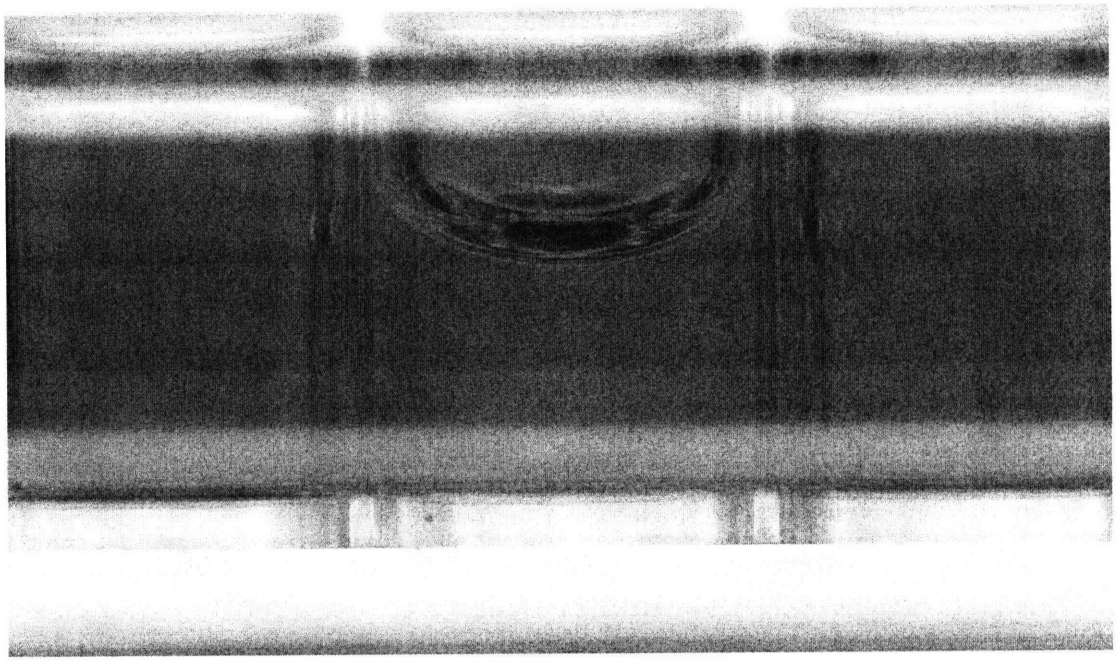

Figure 2.2. Phosphate buffered saline in cell-culture treated polystyrene 96-well plate (the same treatment polystyrene employed in commercial OBS plates). The camera was adjusted to focus on the bottom-most trace of the meniscus, which is the plane at the center of the well.

Modifying the surface of polystyrene by deposition of a thin layer of a hydrophobic compound minimized formation of a meniscus at the air-liquid interface. The hydrophobic nature of the silane layer is demonstrated by observing the contact angle formed between PBS and a silane-coated polystyrene lid (Figure 2.3). Three polystyrene 96-well plates were modified by silane vapor deposition to determine reproducibility of the vapor deposition process as determined by contact angle formed between PBS and the silane-coated polystyrene lid. For each plate, the contact angle was measured five

times to determine reproducibility of contact angle measurement. The average coefficient of variation for contact angle measurements made on the same polystyrene lid was 1.6%. The average (n=3) contact angle between PBS and the silane-modified surface was 93.3° (COV = 3.5%). This contact angle indicates that PBS was neither more attracted to nor repelled to the silane surface than it was to itself and therefore formed a flat interface when dispensed into a 96-well plate. This phenomenon was observed (Figure 2.4), although there were deviations at certain points where the medium seems to 'latch' onto the sidewall. These phenomena were likely a result of the system not being quite at equilibrium. By shaking the plate, these aberrations were disrupted and typically displaced to different locations, but it proved difficult to remove them entirely.

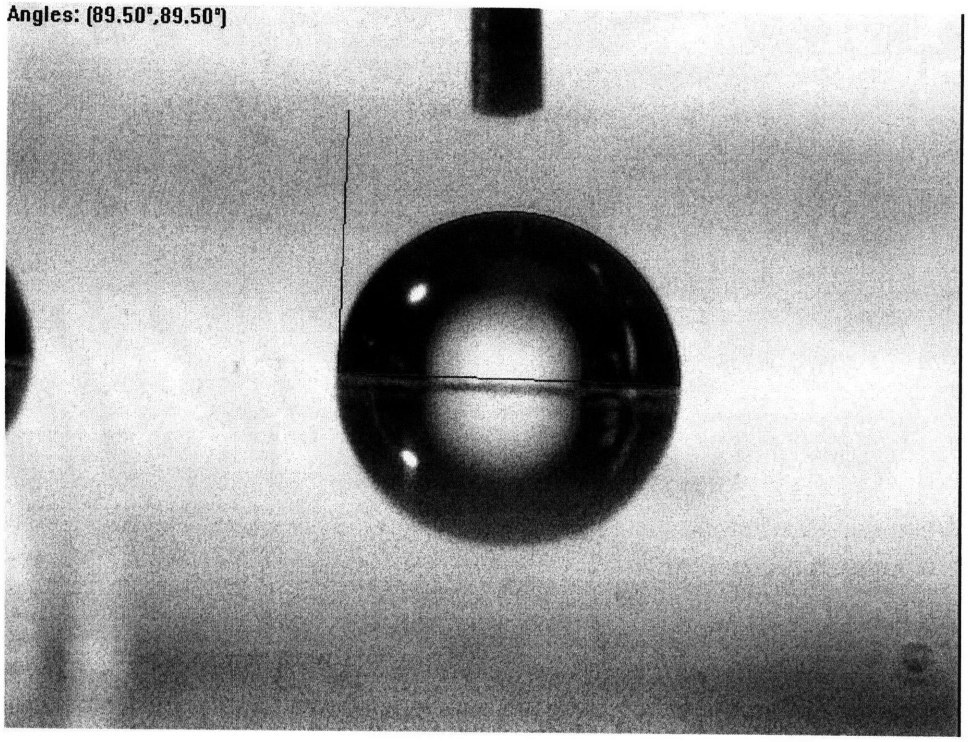

Figure 2.3. Drop of phosphate buffered saline on polystyrene surface with a thin film of silane deposited on the surface. The hemispherical fitting and estimation of contact angle were performed with video contact angle software.

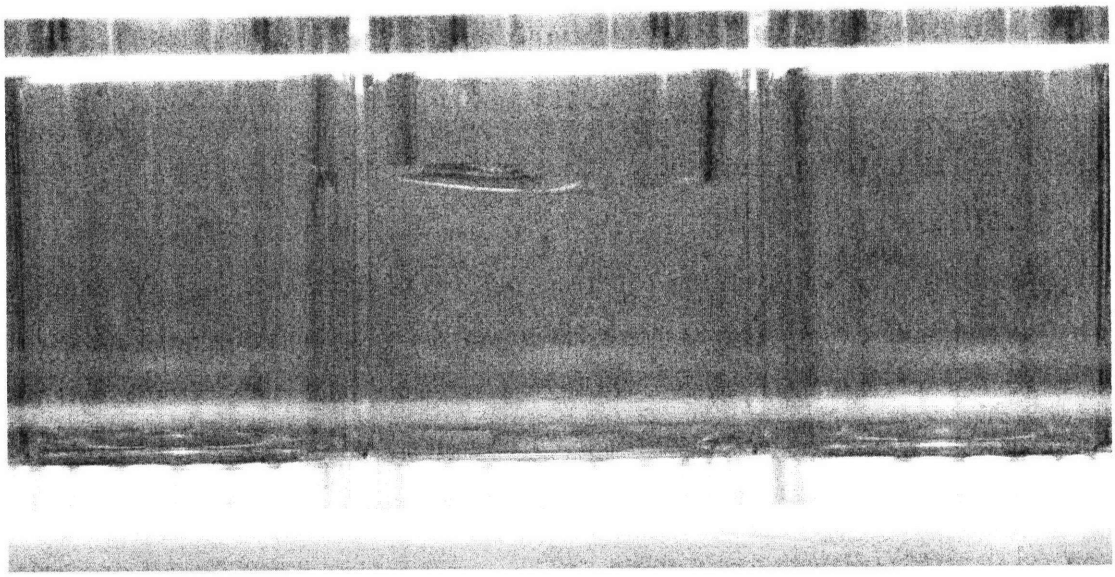

Figure 2.4. PBS in silane-coated polystyrene 96-well plate.

The second process to modify the surface of the polystyrene deposited perfluorodecylacrylate, which imparted a 'Teflon-like' quality to the surface. The high level of hydrophobicity was visualized via contact angle measurement (Figure 2.5A). The contact angle was observed to be always greater than 115°C, which was far enough from the desired 90°C contact angle that further experiments and measurements with the fluorinated polymer were not conducted. A slightly inverse meniscus formed when PBS was loaded into a 96-well plate modified with this Teflon-like polymer (Figure 2.5B).

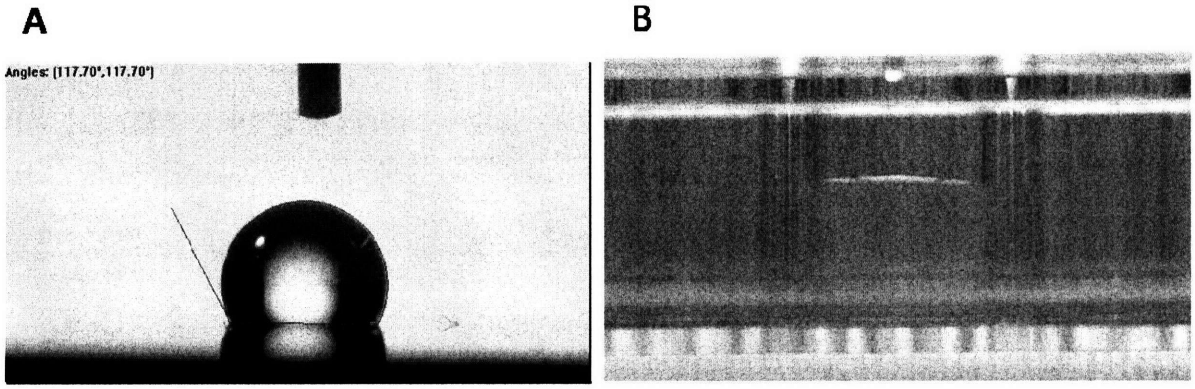

Figure 2.5. Teflon-like coating gives substrate hydrophobic properties. (A) Contact angle of PBS on a silicone water with thin film of fluorinated polymer, θ = 117.7. (B) Inverse meniscus formed when PBS loaded into modified 96-well plate. Both the silicone wafer and 96-well plate were modified simultaneously so that they exhibit the same surface properties.

2.3.3 Dry Transient Experiments with Flat OBS Plates

Experiments without any liquid medium were performed with flat 0.5 mm, 1 mm, and 2 mm oxygen sensor / silicone rubber discs to measure the transient response when taken from anoxia to ambient oxygen conditions. When 0.1M sodium sulfite solution was added to the OBS wells, fluorescent intensity increased until it reached a plateau when all oxygen was quenched from the well (Figure 2.6). The time needed to reach a plateau and the magnitude of the plateau fluorescent intensity both increased with increasing thickness as expected. There was more oxygen stored in the thicker discs so it would take longer to quench all oxygen and there was more fluorophor present in the thicker discs, which would give a greater fluorescent intensity. However, the magnitude of intensity increase is not proportional to the increase in the amount of fluorophor present.

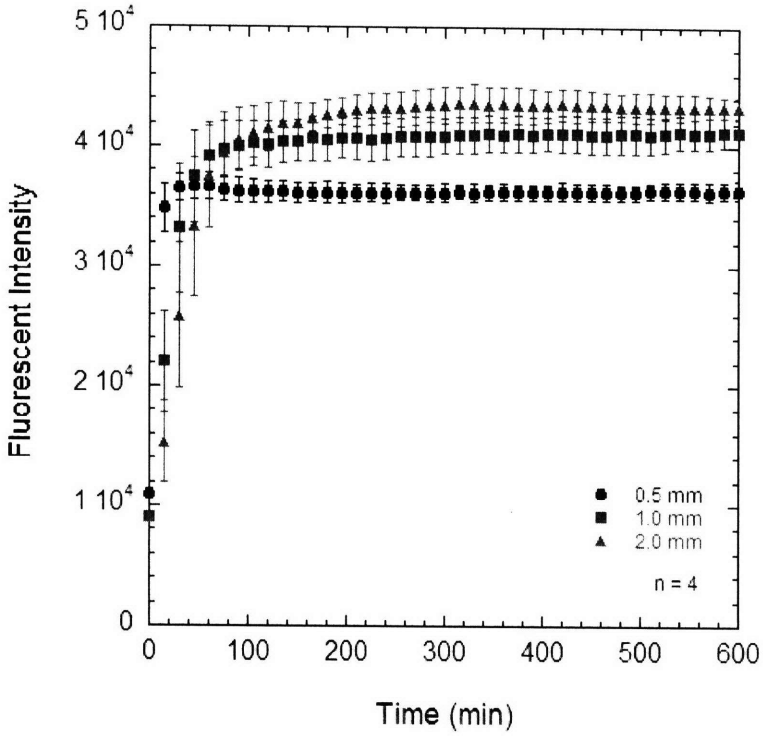

Figure 2.6. Fluorescence transient response when 0.1M sodium sulfite solution added to OBS plate with 2 ul silicone rubber used to seal flat discs of varying thickness. Standard deviation of n=4 wells plotted. Every third data point plotted for clarity.

Average normalized fluorescence values, I_0/I ,for each thickness are shown in Figure 2.7A; corresponding values of pO_2 computed using the Stern-Volmer equation (Eq. 4.2) are shown in Figure 2.7B. As expected, the thicker silicone rubber discs responded slower, although it is interesting to note

that all conditions responded relatively quickly within the first 30 minutes followed by a slow, steady increase in the pO_2. This gradual increase suggests a slow thermal equilibration of the OBS plate.

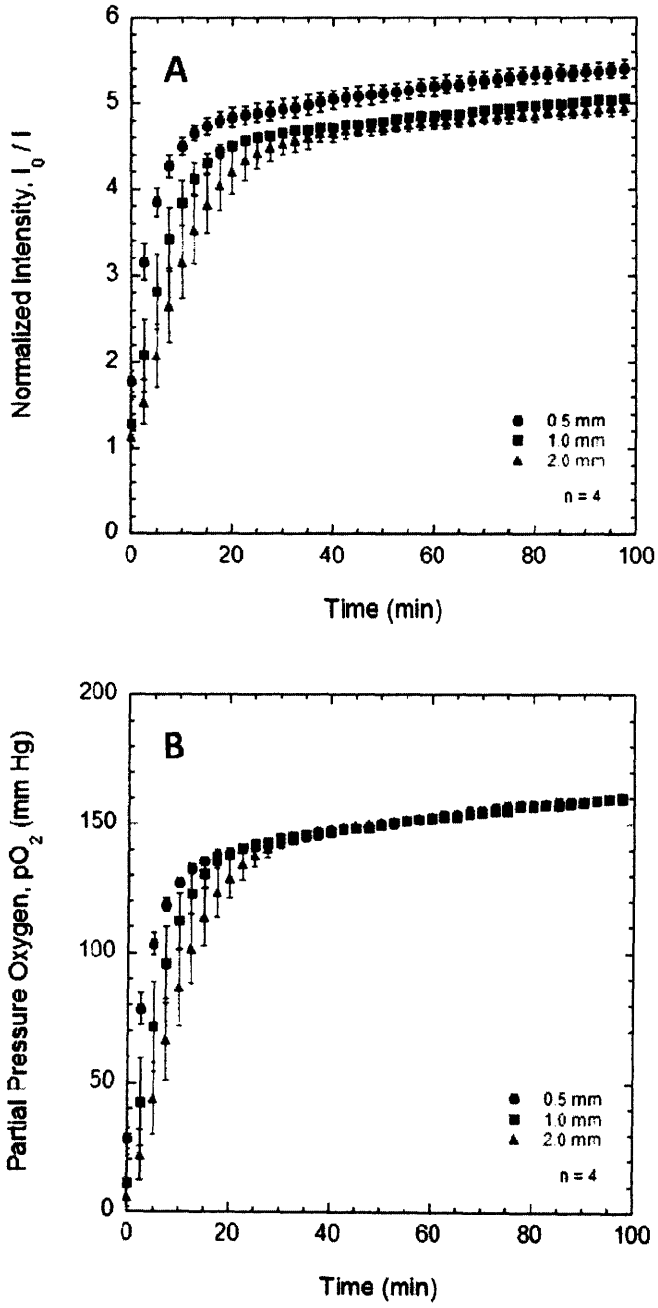

Figure 2.7. Average transient response when OBS plate with 2 ul silicone rubber to seal flat discs of varying thickness when removed from anoxia to ambient oxygen environment for (A) normalized fluorescence, I_0/I, and (B) computed pO_2. Every fifth data point plotted for clarity.

Wells with 2ul liquid silicone rubber placed between the well-bottom and silicone rubber disc did not respond differently for those wells with 0.5mm discs (Figure 2.8A), however, for the thicker discs, the wells with the 2 ul seal responded slower (Figure 2.8B & C). Silicone rubber does have a large oxygen solubility and so will be a large sink for oxygen as it enters the system, which would delay the transient response and help to explain why the wells with 2 ul silicone rubber responded slower. However, were this to be only explanation for the different responses, the thinnest silicone rubber disc would expectedly show the largest discrepancy between the two experimental conditions because the 2ul silicone rubber difference would be proportionally larger to the total volume silicone rubber than for the thicker discs (a 0.5mm thick disc is approximately 16 ul).

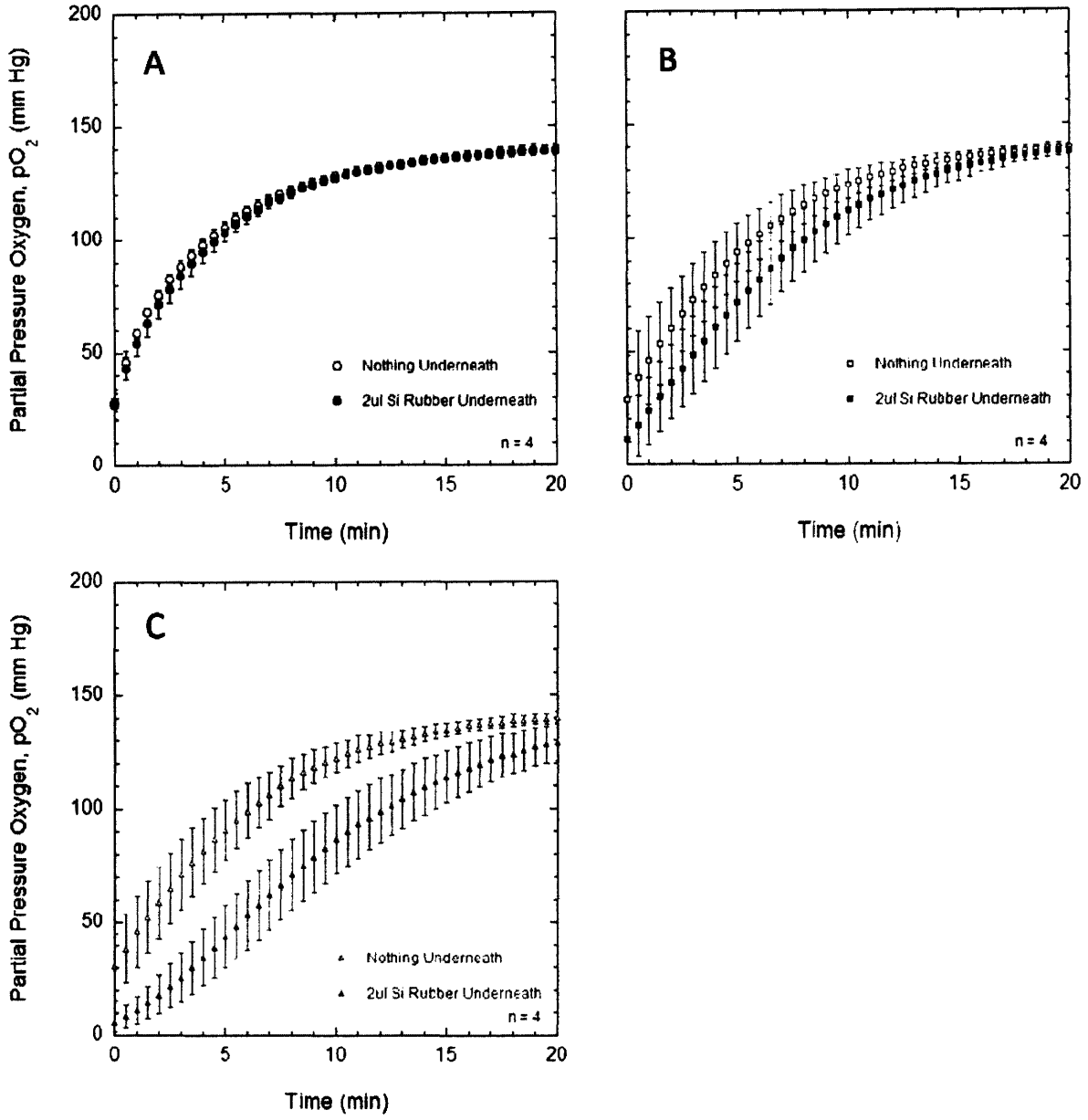

Figure 2.8. Transient response of flat-disc OBS wells to a sudden removal from anoxia to ambient oxygen conditions where silicone rubber discs were either directly seated onto the polystyrene well bottom or placed on top of 2 ul liquid rubber and subsequently cured to seal the disc to the well-bottom. Silicone rubber discs were (A) 0.5mm, (B) 1mm, or (C) 2 mm. All conditions performed with 4 replicates.

There must be an additional explanation for how the 2 ul silicone rubber affected the transient response for it to be consistent with the observation that the effect increased with thicker silicone

rubber discs. The silicone rubber discs were cut to be slightly smaller than the well-bottom diameter to facilitate pressing the discs down to the well-bottom without trapping air. As a result of this, the discs were not flush with the side of the well so that there was a gap where air could enter so that there was a parallel path for oxygen diffusion (Figure 2.9). When the small drop of liquid silicone rubber was placed on the well bottom and the silicone rubber disc pushed down from the top of the well, some of the liquid silicone rubber was displaced and filled the gap. If the liquid silicone rubber perfectly sealed the gap and had similar diffusion and solubility properties as the silicone rubber disc, then the system would be restored to a 1-D oxygen diffusion problem.

Figure 2.9. Diagram of flat silicone rubber not completely flush with edge of well, which allows oxygen to diffuse into the silicone rubber disc through both the top and the side.

The elapsed time for each thickness silicone rubber was nondimensionalized by dividing the time, t, by the time scale, τ, which is defined for each thickness by

Eq. 2.19
$$\tau = \frac{h^2}{D}$$

where h is the thickness of the silicone rubber and D is the diffusivity of oxygen in silicone rubber. The dimensionless time, t*, is given by

Eq. 2.20

$$t^* = \frac{Dt}{h^2}$$

By nondimensionalizing time, the three different thicknesses should essentially become the same oxygen transport problem. The plot of pO_2 as a function of dimensionless time should fall along the same curve for all three thickness silicone rubber discs if the system is truly a 1-D slab. The nondimensional plot of experimental data (where 2ul of silicone rubber was used to seal the discs) show clearly that each thickness disc has its own unique transient curve (Figure 2.10). The thicker discs actually responded faster when plotted against dimensionless time, which is consistent with the hypothesis that oxygen is leaking down the side wall, even when the 2 ul of silicone rubber is used to seal the system and is forced up the side walls of the well. This alternate pathway for oxygen transport became increasingly important as the thickness increased and the assumed pathway for transport (diffusion from the top of the silicone rubber) took more time. A similar dimensionless time plot for wells without 2 ul of silicone rubber would show this effect even more dramatically.

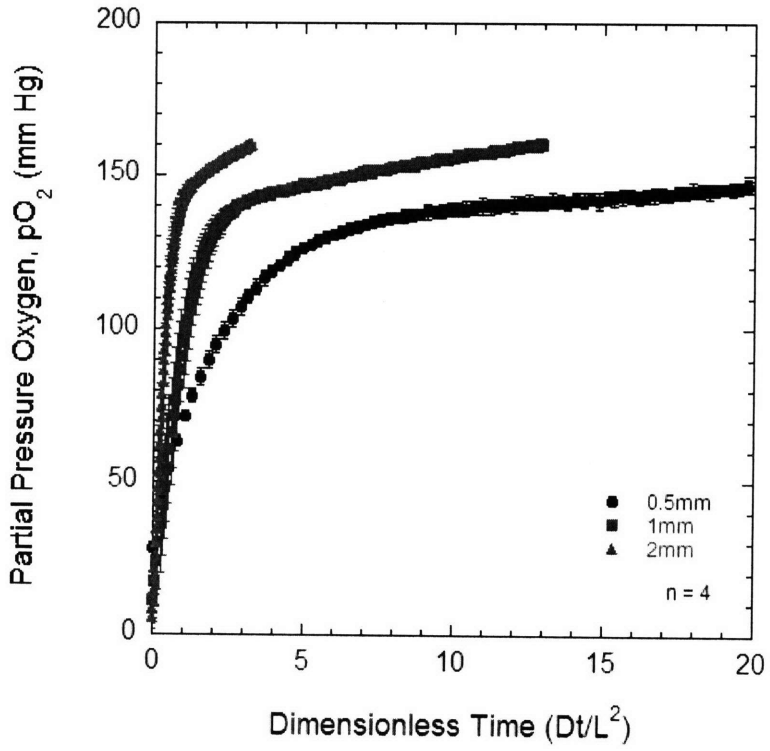

Figure 2.10. Dimensionless time plot of transient plot for OBS plate with different thickness silicone rubber disc. Data shown for wells containing 2 ul silicone rubber to help seal disc to well-bottom.

2.3.4 Theoretical Simulations of Dry, Transient Experiment

Theoretical simulations highlight how experimental results with flat disc geometry deviated from the expected results for a truly 1-D dimensional geometry. These theoretical responses also highlight other experimental complexities that could not be addressed in a theoretical simulation. Theoretical responses responded quickly to the step change in oxygen and reached the ambient oxygen within 40-60 minutes (Figure 2.11A), unlike experimental data that appeared to be slowly trending upward over time as the OBS plate equilibrates with ambient conditions. There is uncertainty in the parameter values used for oxygen diffusion and solubility in silicone rubber which could alter the characteristic time of the response, however, the shape of the theoretical curves is unmistakably different than experimental data.

Dimensionless time plots of theoretical data confirm that different thickness silicone rubber discs are essentially the same oxygen transport problem, which simply need to be scaled correctly to collapse all of their individual transient response curves into one universal transient response (Figure 2.11). Clearly, experimental results deviated from this hallmark of 1-D slab diffusion as the different curves could not be superimposed upon each other. It should be noted that this observation is also independent of the particular value of oxygen diffusion used to nondimensionalize time.

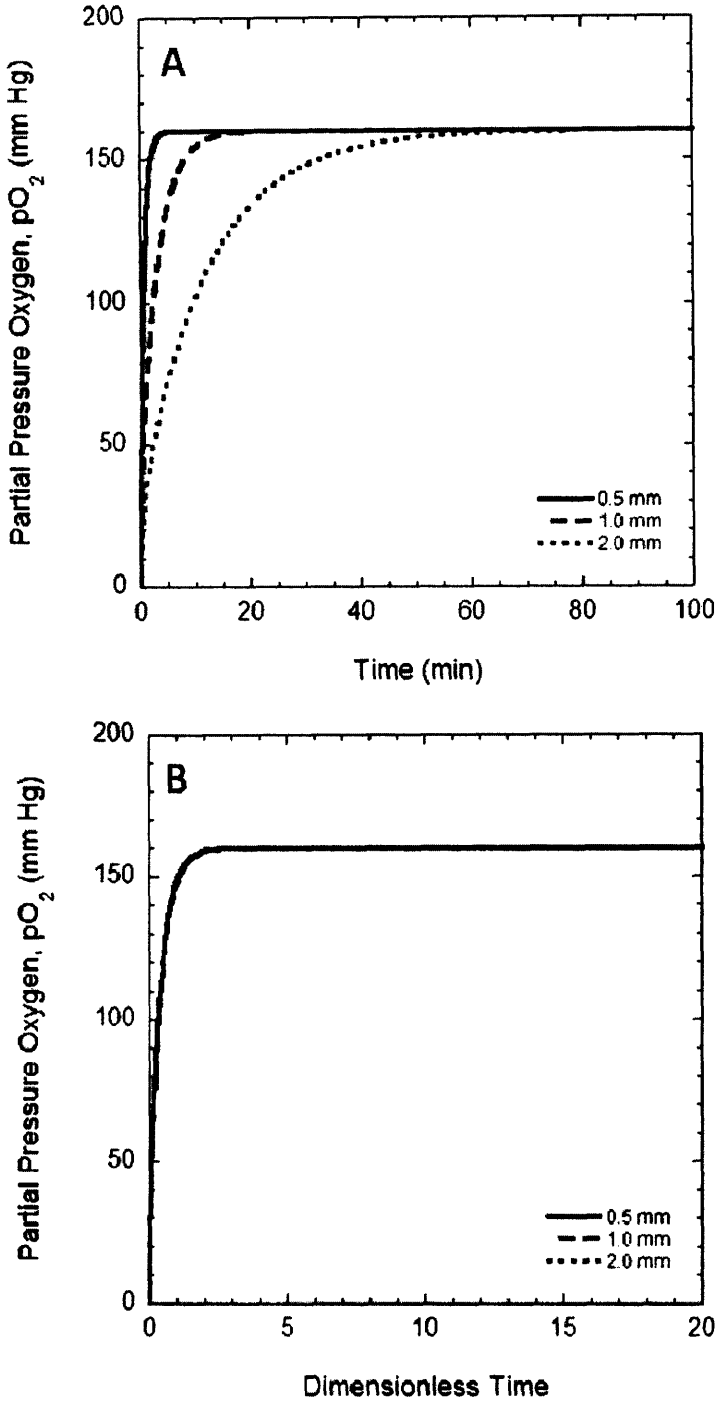

Figure 2.11. Theoretical simulations of dry, transient experiments. (A) Plot of pO_2 as a function of time for three different thicknesses of silicone rubber. (B) Plot of pO_2 as a function of dimensionless time. There are actually three curves plotted, but they have all collapsed onto the same curve.

2.3.5 Theoretical Evaluation of Curved Geometries

Two theoretical models of the commercial OBS plate were created within COMSOL to determine whether a homogeneous distribution of oxygen sensor particles (Figure 2.12A) would yield different results than a localization of same sensor particles to the bottom edge of the silicone rubber (Figure 2.12B) as had been observed previously in commercial OBS wells (see Figure 2.1A). The average pO_2 of the phase containing sensor particles (highlighted regions in Figure 2.12) was plotted over time in response to a sudden consumption of oxygen at the interface between silicone rubber and liquid medium. Simulations where the total OCR within the well ranged from 0.125 – 1 nmol/min were conducted to compare the two models (Figure 2.13). It appears there is no distinct difference between homogeneously dispersing the oxygen sensor particles or allowing them to settle and localize to a specific region of the silicone rubber.

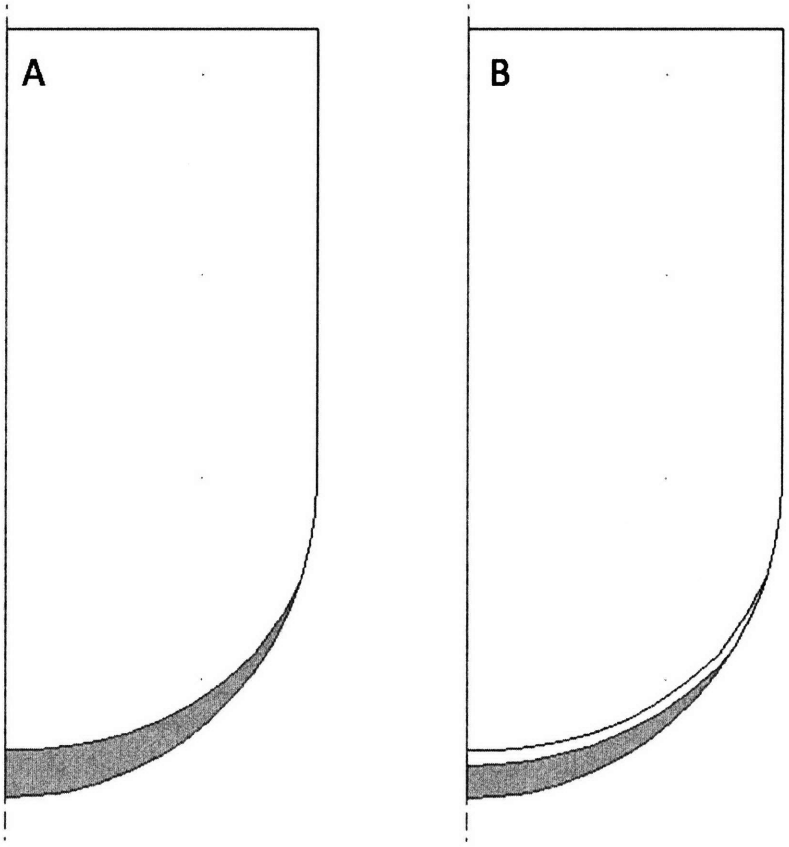

Figure 2.12. Theoretical model of commercial OBS well with (A) homogenous distribution of oxygen sensor particles and (B) localization of oxygen sensor particles to the bottom edge of the silicone rubber.

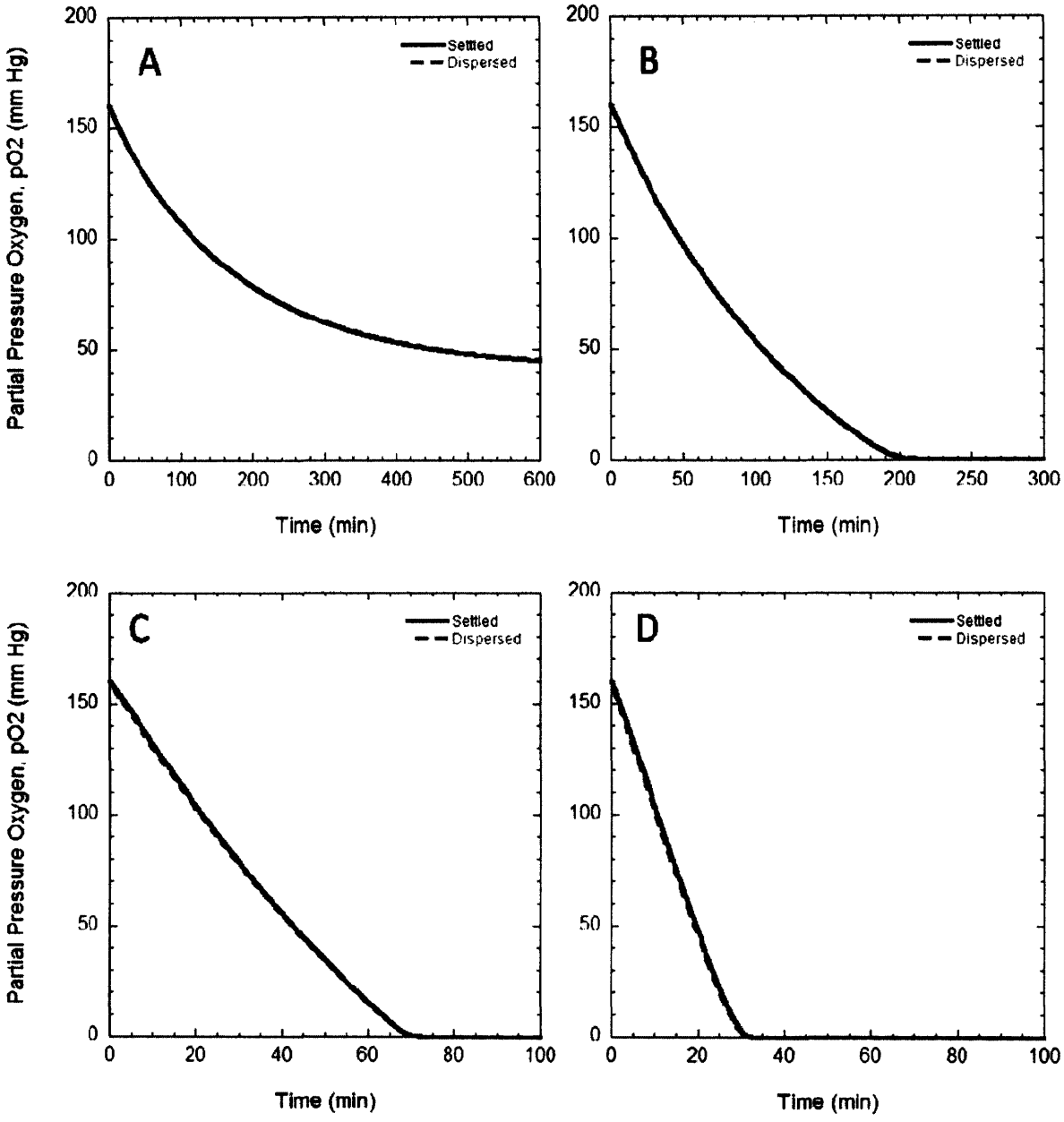

Figure 2.13. Transient theoretical response to sudden oxygen consumption at silicone rubber / liquid medium interface in commercial OBS well with either homogenously dispersed oxygen sensor (dashed red line) or localized oxygen sensor at the bottom of the silicone rubber (solid blue line). The oxygen consumption at the interface was specified as (A) 0.125 nmol/well; (B) 0.25 nmol/well; (C) 0.5 nmol/well; and (D) 1 nmol/well. The two responses fall nearly exactly on top of one another so it is difficult to distinguish that there are actually two curves

The commercial round-bottom model was compared with a 1-D flat slab model with the same volume silicone rubber at multiple different OCR densities. Because the oxygen consumption boundary condition was entered as a flux on a per surface area basis it was necessary to calculate the OCR flux for

the curved round-bottom model so that the total OCR within the well was equal between the curved and slab models. The surface area of the silicone rubber / liquid medium interface in the commercial model was calculated using COMSOL and found to be 0.3897 cm^2. The total OCR/well was then normalized by the surface area in order to determine the OCR flux to input into COMSOL. A comparison of transient responses reveals that the curved geometry responds increasingly slower as the oxygen consumption within the well is increased (Figure 2.14). However, even at 1nmol/min, the difference in the time to reach approximately 0 mm Hg is approximately 15%, so the effect of a curved geometry can be considered minor unless an extremely large amount of tissue is loaded into the OBS.

A theoretical model of an OBS well with a flat air-liquid interface (Figure 2.15A) was compared with a perfectly hemispherical meniscus at the air-liquid medium interface (Figure 2.15B) to evaluate the maximum possible effect the meniscus might have on transient OBS measurements and the error introduced when a 1-D assumption is invoked. Although the observed meniscus is less curved than a hemisphere (see Figure 2.2) this model provided us with an order of magnitude estimate of the meniscus. The presents of the meniscus only slightly alters oxygen diffusion and the transient response of the OBS plate (Figure 2.16). The effect was very minimal at both low and high OCR densities, although it appears that the effect is slightly more pronounced at low OCR density.

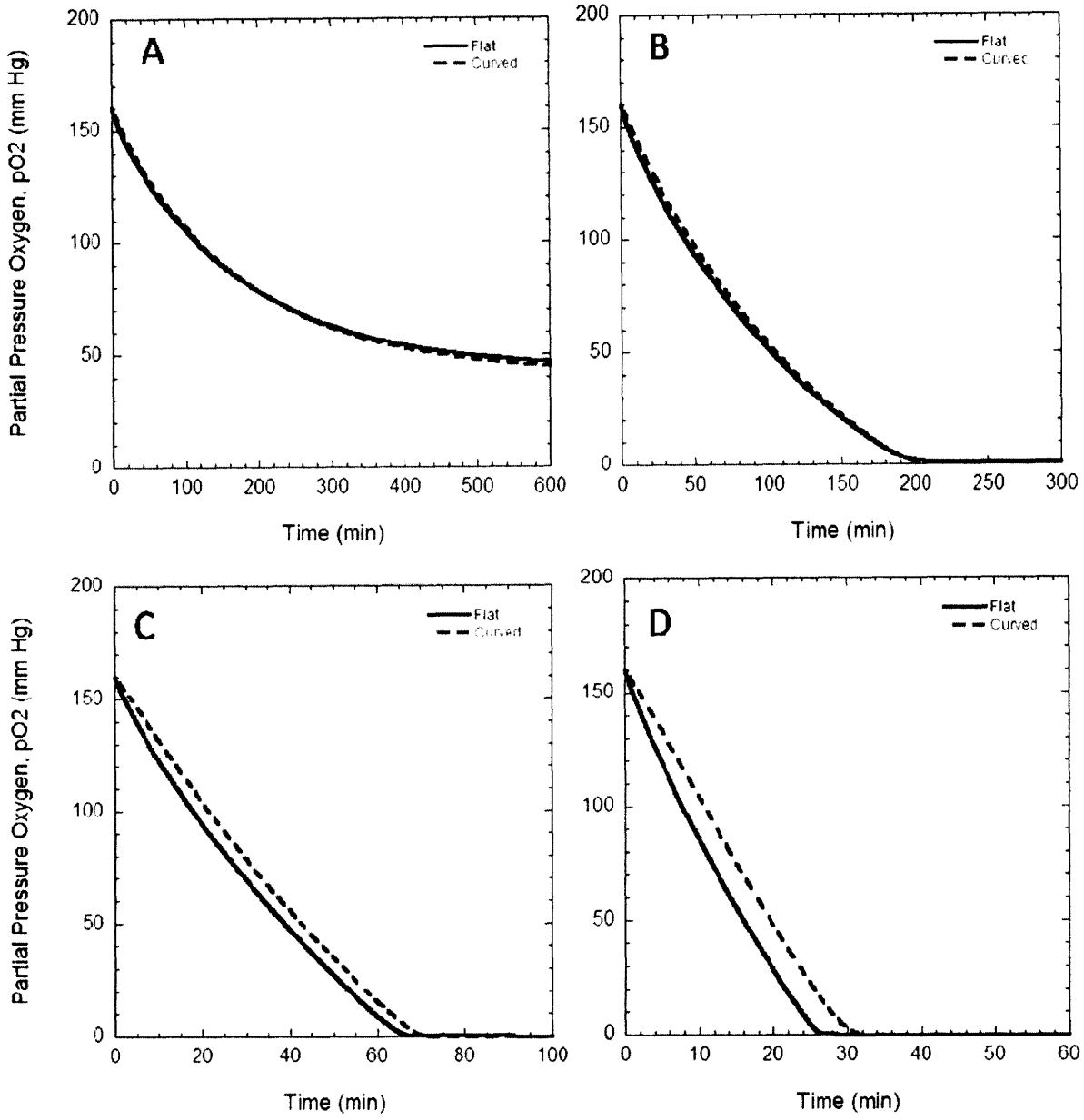

Figure 2.14. Comparison of theoretical transient response when oxygen consuming tissue is introduced to the OBS well at the bottom of liquid medium for a commercial, curved OBS plate (dashed red line) with an ideal, 1-D OBS plate. The total amount of oxygen consumption in the well was constant between the two different models and was specified as (A) 0.125 nmol/well; (B) 0.25 nmol/well; (C) 0.5 nmol/well; and (D) 1 nmol/well.

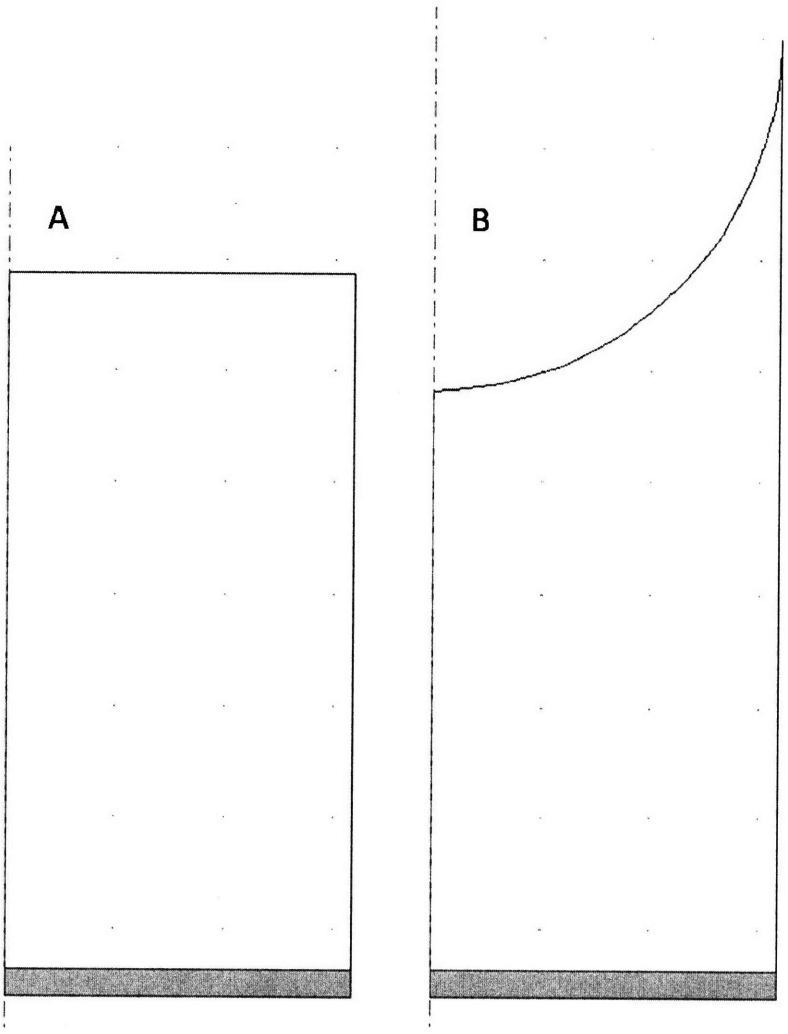

Figure 2.15. Theoretical OBS well model with (A) flat air-medium interface and (B) hemispherical meniscus at air-medium interface. The volume of liquid medium is equal in both models. The volume of silicone rubber is 7.6 ul.

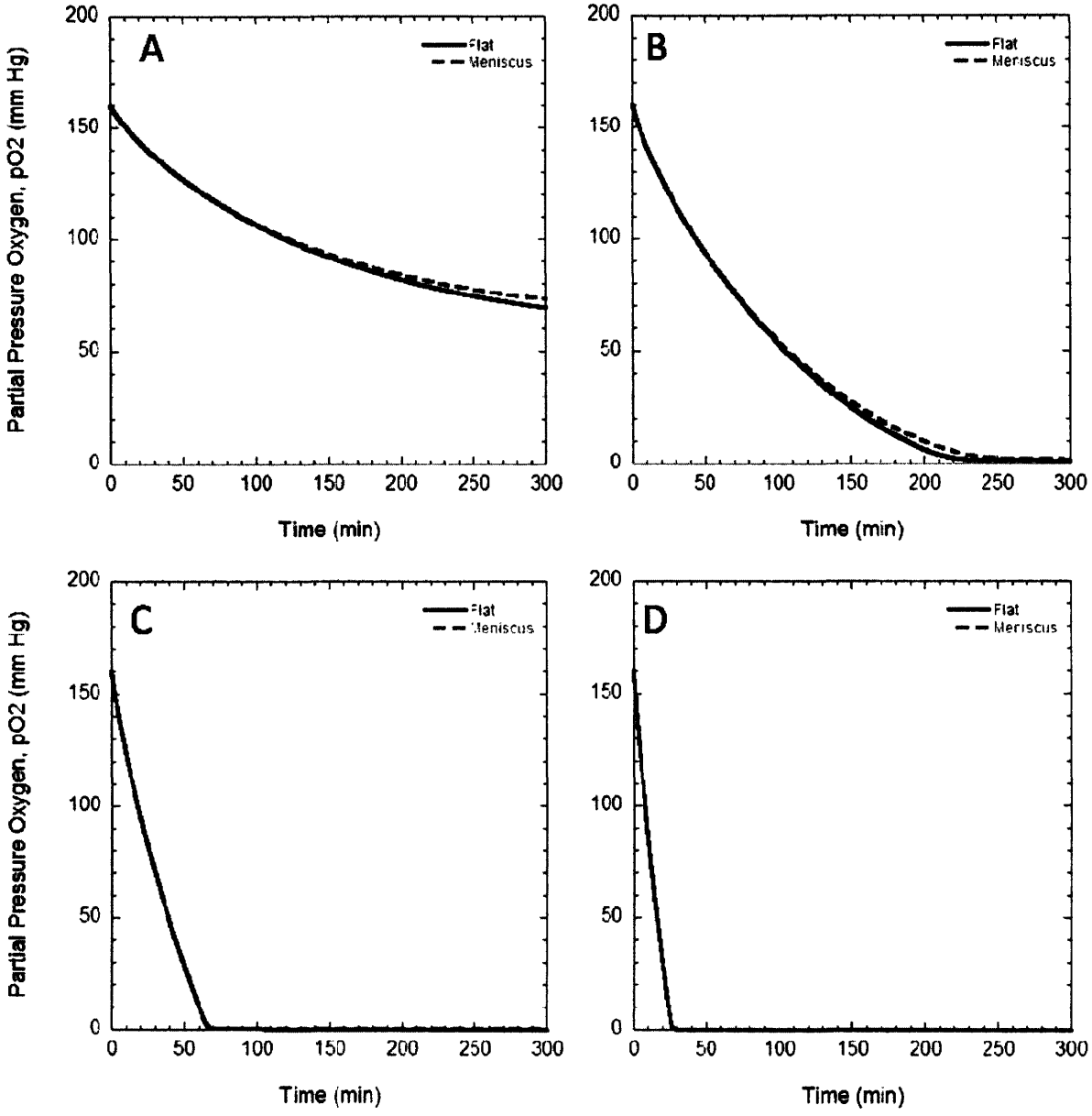

Figure 2.16. Comparison of theoretical transient response when oxygen consuming tissue is introduced to the OBS well at the bottom of liquid medium between an ideal, flat air-medium interface (solid blue line) and a hemispherical meniscus interface (dashed red line). The total amount of oxygen consumption in the well was constant between the two different models and was specified as (A) 0.125 nmol/well; (B) 0.25 nmol/well; (C) 0.5 nmol/well; and (D) 1 nmol/well.

2.4 Discussion

In this study we characterized the curved geometry of commercial OBS plates and tried to fabricate OBS plates that more closely resembled the 1-D, slab geometry that had been initially assumed to describe the OBS well. The advantages of being able to fabricate a truly 1-D system are less clustering of tissue in the center of the well as a result of tumbling down the steep side walls and simplified geometry for theoretical modeling. Previous attempts to model steady-state OBS experiments have not been able to describe all observable phenomenon. A transient experiment is inherently more complex than steady-state and it behooves us to simplify the transient OBS experiment in any way possible to increase the likelihood that theoretical simulations will match with experimental data. Fabricating a 1-D OBS well would simplify the system and perhaps improve attempts at matching data with theory.

Switching to a flat-bottom 96-well plate was insufficient to create a flat, 1-D silicone rubber / oxygen sensor mix as a result of capillary forces wicking the mixture up the side walls of the well. We successfully fabricated a flat silicone rubber disc that could be inserted into a 96-well plate, however, initial cell-free experiments and theoretical simulations indicated that the system was not truly described by 1-D diffusion. The challenge of sealing the cured, cut silicone rubber disc to all sides and bottom of the well without trapping any air bubbles proved beyond our capabilities. Dimensionless plots of experimental data confirmed that alternate pathways for oxygen transport exist.

Surface modification of polystyrene by vapor deposition of silane on an OBS plate changed the geometry of the air-liquid interface and was able to eliminate most of the meniscus typically formed when medium was added to a polystyrene well.

Theoretical simulations compared actual geometries to ideal, 1-D geometries to estimate the magnitude of difference invoked when simplifying geometric assumptions are made. The assumption of a flat, silicone rubber / oxygen sensor disc overestimated the speed with which an OBS plate transiently responded to oxygen consumption being. The magnitude of the overestimation was approximately 15%, however, the difference was less when a smaller OCR density was input into the theoretical model. The assumption that the gas-liquid interface is flat invokes very little error into theoretical models. The commercial OBS system can be modeled as a 1-D slab with minor loss of information from a full-blown, geometrically accurate solution.

This study highlighted one concern for future attempts at modeling transient OBS measurements, namely that experimental data slowly trends upward. The cause of the slow equilibration is unknown and cannot be incorporated into theoretical models, which reduces the likelihood that theoretical models will accurately reflect experimental data. Still, theoretical models can be immensely useful to help design experimental parameters, which will be a focus of the next chapter.

3. Theoretical Evaluation of OBS Parameters

3.1 Introduction

Previous efforts by Rappel [34] to theoretically model OBS steady-state measurements focused on identifying assumptions that both (1) were inaccurate, and (2) introduced large errors such that theoretical models did not match experimental data. Once an incorrect assumption was observed and shown to be significant via sensitivity analysis, then either the experimental protocol was modified so that it more closely matched the initial assumption or the theoretical model was modified to more closely match reality. Either way, the approach focused on narrowing the gap between simulation and experimentation so that accurate OCR estimations could be made using OBS. Rappel was able to close the gap by identifying convection as a significant source of deviation, however, experimental measurements continued to underestimate actual OCR and no theoretical explanation could reconcile the differences. Additionally, certain experimental methods to alter the OBS system to more closely resemble the simplifying assumptions are not easily possible for transient OBS measurements. Gelling liquid agarose to form a quiescent medium is not easily done when tissue is added to the OBS plate and immediately measured in a fluorescent plate reader.

This research takes a slightly different approach to using theoretical modeling to support accurate OBS measurements. This approach is semi-quantitative and does not seek to quantitatively predict actual OBS experiments. Rather, it tries to identify assumptions that can be invoked without significantly compromising qualitative behavior predicted by theoretical models. Thus, the end-goal is a simplified theoretical model that can be used to better understand qualitative features of OBS. An example of this from Chapter 2 is the finding that the shape of both the silicone rubber and liquid meniscus do not significantly affect OBS performance and can therefore be simplified as being flat, 1-D objects.

In this chapter, we will evaluate the assumption of an infinitely thin layer of tissue to determine its effect on transient OBS experiments. Rappel [34] had previously evaluated this assumption for steady-state measurements, but not for transient measurements. As part of evaluating this assumption,

it is also necessary to explore the geometry of a finite tissue layer and exactly how close tissue can pack together while remaining a monolayer.

A simplified model consisting only of 1-D slabs of silicone rubber and quiescent, liquid medium is then used to explore the range of OBS parameters to find parameter values that make transient measurements more amenable to consistent, practical data analysis by improving the qualitative shape of pO_2 data so that it becomes easier to fit data to a line.

3.2 Methods

3.2.1 Calculating OCR Density of Tissue Monolayer

In order to evaluate the effect of tissue layer with finite thickness, it was necessary to determine the maximum amount of tissue that could be packed into a monolayer. The closest packing possible for an array of sphere is a face-centered cubic (FCC) array, where the diagonal of the unit cell is equal to twice the sphere diameter (Figure 3.1). This analysis was performed for both islets and cells to determine the maximal surface density before tissue begins to stack on one another.

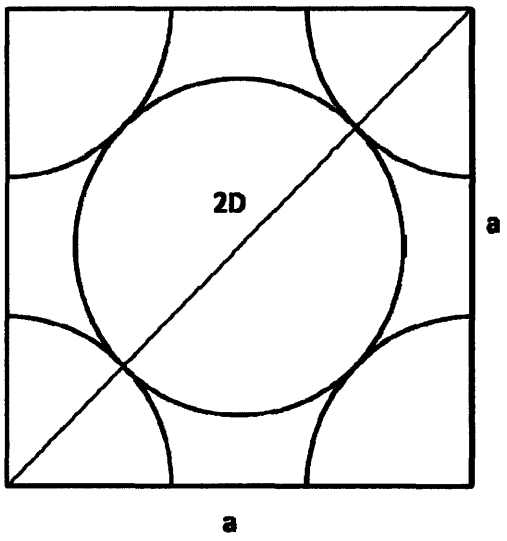

Figure 3.1. Unit cell of a face-centered cubic (FCC) array. A close packing of the tissue on a flat OBS well will look somewhat similar to this array when viewed from above.

The surface density (tissue/cm^2) was determined by relating the diameter of a unit of tissue, D, to the dimension of the unit cell, a, using Pythagorean's theorem

Eq. 3.1
$$a = \sqrt{2}D$$

where D is the diameter of either an islet equivalent (IEQ), 150 um, or a single cell, 12 um. The surface density was then determined by dividing the total number of spheres within the unit cell, 2, by the area of the unit cell.

Eq. 3.2
$$\frac{tissue}{cm^2} = \frac{2}{(\sqrt{2}D)^2} = \frac{1}{D^2}$$

For a single cell monolayer, the cell surface density was multiplied by an average measure of OCR/cell to yield an OCR density.

Eq. 3.3
$$\frac{OCR}{cm^2} = \frac{cells}{cm^2} \cdot \frac{OCR}{cell}$$

For an islet monolayer, the islet surface density was multiplied by the number of cells in an islet equivalent and an average measure of OCR/cell to yield OCR density.

Eq. 3.4
$$\frac{OCR}{cm^2} = \frac{IEQ}{cm^2} \cdot \frac{cells}{IEQ} \cdot \frac{OCR}{cell}$$

Lastly, the OCR density was multiplied by area of the well-bottom of a 96-plate to yield the total OCR within an OBS well.

Eq. 3.5
$$OCR = \frac{OCR}{cm^2} \cdot \pi R_{well}^2$$

Parameter values are given in

Table 3.1.

3.2.2 Theoretical Simulations

Theoretical models for oxygen transport were created to simulate transient experiments with tissue present. Simulations were used in a semi-quantitative fashion to evaluate certain theoretical assumptions and to explore the effect of changing some of the parameters in a transient experiment. Specifically, the assumption that the finite dimension of the tissue layer can be ignored was evaluated and the following parameters were systematically varied: (1) silicone rubber thickness, (2) medium thickness, and (3) total OCR. All models used a simplified, 1-D slab geometry and neglected the effect of convection. The species conservation equation for O_2 in the absence of convection is given by

Eq. 3.6
$$\frac{\partial c}{\partial t} = D\nabla^2 c + R$$

where c is the concentration of oxygen, D is the diffusivity of oxygen and is assumed to be isotropic, and R is the homogeneous generation term for oxygen. For convenience, the concentration terms in Eq. 3.6 are replaced with oxygen partial pressure, p, using

Eq. 3.7
$$c = \alpha pO_2$$

where α is the Bunsen solubility coefficient of oxygen. We assume that within each phase the solubility is constant so that Eq. 3.6 becomes

Eq. 3.8
$$\alpha \frac{\partial pO_2}{\partial t} = (D\alpha)\nabla^2 pO_2 + R$$

where (Dα) is the permeability of oxygen.

This general equation describes oxygen transport in each phase of the systems (medium, silicone rubber, tissue). At the interface between any two phases, the following condition must be satisfied

Eq. 3.9
$$p_{O_2,1} = p_{O_2,2}$$

where the subscripts denote different phases of the system. The convenience of using the equations with partial pressure instead of concentration is that partial pressure is constant across any interface, while concentration changes due to solubility differences between the phases. Additionally, unless specified otherwise, the interface between any two phases is also subject to the condition that the normal flux leaving one phase is equal to the normal flux entering the second phase

Eq. 3.10 $$n \cdot (-(D\alpha)\nabla pO_2)_1 = n \cdot (-(D\alpha)\nabla pO_2)_2$$

where n is the unit vector normal to the interface between phases.

The boundary condition at the air-liquid medium interface was specified as constant ambient oxygen.

Eq. 3.11 $$pO_2\big|_{\text{air-medium}} = pO_{2,amb}$$

An insulating boundary condition was specified at the bottom of the silicone rubber, x=0, where it interfaces with the polystyrene well-bottom.

Eq. 3.12 $$\frac{\partial pO_2}{\partial z}(0,t) = 0$$

The initial condition was specified so that all phases were equilibrated with ambient oxygen.

Eq. 3.13 $$pO_2\big|_{t=0} = pO_{2,amb}$$

Models for were constructed and solved using these general equations in the commercially available software COMSOL Multiphysics 3.4 (COMSOL Inc., Burlington, MA). All models were meshed to contain more than 100 nodes. Parameter values input into the simulation models are given in Table 1. The relative error estimated by the finite element software in the solution vector for concentration, which takes into account the current and previous solution in the iterative solver was constrained to be less than 10^{-6}.

The average partial pressure of oxygen within the silicone rubber, $\langle pO_2 \rangle_{si}$, was determined by integrating pO_2 over the length of the silicone rubber slab and normalizing by its length, as given by

Eq. 3.14
$$< pO_2 >_{si} = \frac{\int pO_2 dz}{\int dz}$$

The average partial pressure within the silicone rubber was thought to represent the pO_2 that is indirectly measured via the fluorescent intensity measurement of the oxygen-sensitive sensor embedded within the silicone rubber of the OBS plate. In figures throughout this chapter, if pO_2 is not specifically labeled to identify it at a particular location, then it is meant as the average partial pressure within the silicone rubber.

Evaluation of Infinitely Thin Tissue Assumption

Two theoretical models were created to evaluate whether the assumption that the tissue in the OBS well is infinitely thin results in a significant error. The first model assumed the tissue was infinitely thin and contained a silicone rubber phase and a stagnant, liquid medium phase, where a flux discontinuity existed at the interface between the two phases. Oxygen transport within each phase was described by the general species equation, Eq. 3.8, where there is no homogenous oxygen generation term. The flux discontinuity at the interface represented an infinitely thin layer of tissue consuming oxygen according to Michaelis-Menton kinetics and was expressed as the boundary condition

Eq. 3.15
$$-n \cdot (N_1 - N_2) = \frac{\left(\frac{OCR}{cm^2}\right) pO_2}{K_m + pO_2}$$

where OCR/cm^2 is the oxygen consumption surface density in the well, K_m is the Michaelis-Menton constant for oxygen consumption in tissue, and N_i is the flux of oxygen at the boundary in phase i and is expressed by

Eq. 3.16
$$N_i = -(D\alpha)_i \nabla pO_2$$

The second model included a tissue phase to model the islet tissue. The assumption of an infinitely thin layer of cells was not evaluated simply because the characteristic dimension of a single cell, ~ 10 um, is two orders of magnitude less than the characteristic dimension of the next smallest

phase—silicone rubber, ~ 1 mm. It seemed appropriate to evaluate the assumption with islet tissue as islets possess a more significant geometry and are therefore more likely to invalidate the assumption. Within the islet tissue the homogenous oxygen generation term, R, in Eq. 3.8 is described by Michaelis-Menton kinetics

Eq. 3.17
$$R = -\frac{V_{\max} pO_2}{K_m + pO_2}$$

where V_{max} is the maximum possible reaction rate on a volumetric basis (mol / volume time) and is given by

Eq. 3.18
$$V_{\max,IEQ} = \frac{\left(cells/_{IEQ}\right)\left(OCR/_{cell}\right)}{\frac{4}{3}\pi\left(\frac{D_{IEQ}}{2}\right)^3}$$

The thickness of the islet slab was proportional to the number of islets present and was determined by dividing the total islet volume by the area of the well-bottom.

Eq. 3.19
$$h_t = \frac{V_t}{\pi R_{well}^2}$$

Initially, the islet volume specified in the model was determined by multiplying the maximum surface density (Eq. 3.2) by the area of the well bottom and by the volume of an individual IEQ.

Eq. 3.20
$$\begin{aligned} V_{t,\max} &= \frac{1}{D_{IEQ}^2} \cdot \pi R_{well}^2 \cdot \frac{4}{3}\pi\left(\frac{D_{IEQ}}{2}\right)^3 \\ &= \frac{\pi^2 R_{well}^2 D_{IEQ}}{6} \end{aligned}$$

This maximum islet volume provided an upper-bound for the amount of tissue that could be added to an OBS well and still form a monolayer. Substituting Eq. 3.20 into Eq. 3.19, we obtain the maximum tissue height for the theoretical model.

Eq. 3.21

$$h_{t,\max} = \frac{\pi D_{IEQ}}{6}$$

Exploring Parameter Values

The effects of changing total OCR, medium height, and silicone rubber thickness were investigated using a simple 1-D model where the tissue is assumed to be infinitely thin.

The derivative of pO_2 vs. time data was estimated using EXCEL's (Microsoft, Redmond, WA) linear regression function to obtain data for the slope (mm Hg / min) as a function of time.

Table 3.1. Parameters used in theoretical simulations for oxygen transport in OBS wells

Parameter	Symbol	Value	Units	Reference
IEQ diameter	D_{IEQ}	150	um	
Cell diameter	D_{cell}	12	um	Based on average cell diameter
Cells / IEQ		1560		[1]
OCR / cell		2	fmol/min/cell	Based on average historical OCR measurements
Well radius	R_{well}	0.3175	cm	Manufacturer Specifications
Michaelis constant	K_m	0.44	mmHg	[36]
O2 diffusivity - medium	D_m	2.78 x 10-5	cm2/s	[37]
O2 diffusivity - silicone rubber	D_s	2.17 x 10-5	cm2/s	[38]
O2 solubility - medium	α_m	1.27 x 10-9	mol/cm3 mmHg	[37]
O2 solubility - silicone rubber	α_s	12.1 x 10-9	mol/cm3 mmHg	[38]
Ambient oxygen	pO_2	160	mm Hg	

3.3 Results

3.3.1 Surface and OCR Density in Tissue Monolayer

A close-packed monolayer of islets contains 4.4 x 10^3 IEQ/cm^2, which in a 96 well plate is a total of 1.4 x 10^3 IEQ. The typical amount of islet tissue loaded into each well is well below this limit of high-density packing and the assumption of a monolayer of islets was reasonable. For cells, the surface

density of a close-packed monolayer is 6.9×10^5 cells/cm^2, which in a 96 well plate is a total of 2.2×10^5 cells. It was not unusual to exceed this number of cells experimentally, which implies that stacking (i.e. multiple layers of cells) was probably commonplace for cellular experiments. Because the limit of close-packing of tissue is purely a space consideration, it is more appropriate to use surface density calculations when determining whether tissue forms a monolayer or is stacking. However, often it is more convenient to express an OCR density (or total OCR within each well). Assuming that the cellular OCR does not deviate significantly from the parameter value used to make these calculations (2 fmol/min cell) then OCR density or total OCR can be used a good proxy measure of whether tissue forms a monolayer or multiple layers. It is interesting to note that the close-packed OCR density for islet tissue is 10 times larger than for single cells. This result is expected as an islet is a large, multicellular aggregate whose characteristic length is approximately 10 times larger than single cells. The volume of the islet monolayer is thus approximately 10 times larger than the single cell monolayer and will clearly have more cells and therefore higher OCR density. Even when single cells stack to form multiple layers, the height of the multiple layers will still be less than the height of an islet monolayer. Table 3.2 contains a summary of all surface and OCR calculations for close-packed monolayers of both islets and cells.

Table 3.2. Surface and OCR density for close-packed monolayer of islet equivalents and cells

	Surface Density	Total Tissue	OCR Density	Total OCR
Islets	4.4×10^3 IEQ/cm^2	1.4×10^3 IEQ	14 nmol/min cm^2	4.4 nmol/min
Cells	6.9×10^5 cells/cm^2	2.2×10^5 cells	1.4 nmol/min cm^2	0.44 nmol/min

3.3.2 Evaluating Assumption of Infinitely Thin Tissue

The effect of assuming an infinitely thin tissue layer was evaluated by comparing one model with an infinitely thin tissue layer with a model where the tissue was given a finite height proportional to the OCR specified in the model. The specified OCR was converted to islet volume by dividing by the OCR/volume of an IEQ. The OCR/volume of an IEQ is given by

$$\frac{OCR}{vol} = \frac{OCR}{cell} \cdot \frac{cell}{IEQ} \cdot \frac{IEQ}{\frac{4}{3}\pi\left(\frac{D_{IEQ}}{2}\right)^3}$$

Eq. 3.22

$$= \frac{2\text{fmol}}{\text{min cell}} \cdot \frac{1\text{nmol}}{10^6\text{fmol}} \cdot \frac{1560\text{cell}}{1\text{IEQ}} \cdot \frac{1\text{IEQ}}{\frac{4}{3}\pi\left(\frac{150\times10^{-4}\text{cm}}{2}\right)^3}$$

$$= 1.8\times10^3 \frac{\text{nmol}}{\text{cm}^3}$$

where the OCR/cell value is a rough average of historical data taken in the Colton lab. The islet volume was then converted to the slab height by dividing by the cross-sectional area of the well. In this manner, total OCR/well values of 0.5, 1, 2, and 4.4 nmol/min were converted to slab thicknesses of 9, 18, 36, and 79 um.

The transient responses of the two models were nearly indistinguishable from one another except at the largest specified OCR value (Figure 3.2). The largest specified OCR value, 4.4 nmol/min, represented the largest attainable OCR for a monolayer of islets as previously calculated. Even at this large OCR, the finite model's transient response lagged behind by 10% at most. For typical OCR values that would be used experimentally, there was no error associated with assuming an infinitely thin layer of tissue.

The method of converting the total tissue volume to an equivalent slab thickness is understandably a somewhat crude approximation of the finite geometry of an islet layer. Even at low islet surface density where islets are far apart, the relevant characteristic height in the local area of an islet is the diameter of the height. The approach of converting to an equivalent slab thickness essentially smoothes that height across the entire well. More sophisticated models could take into account the 3-D geometry of an islet and spacing, however, the equivalent slab thickness is an appropriate approximation for semi-quantitative modeling where we are more interested in appreciating the order of magnitude of the tissue geometry's effect.

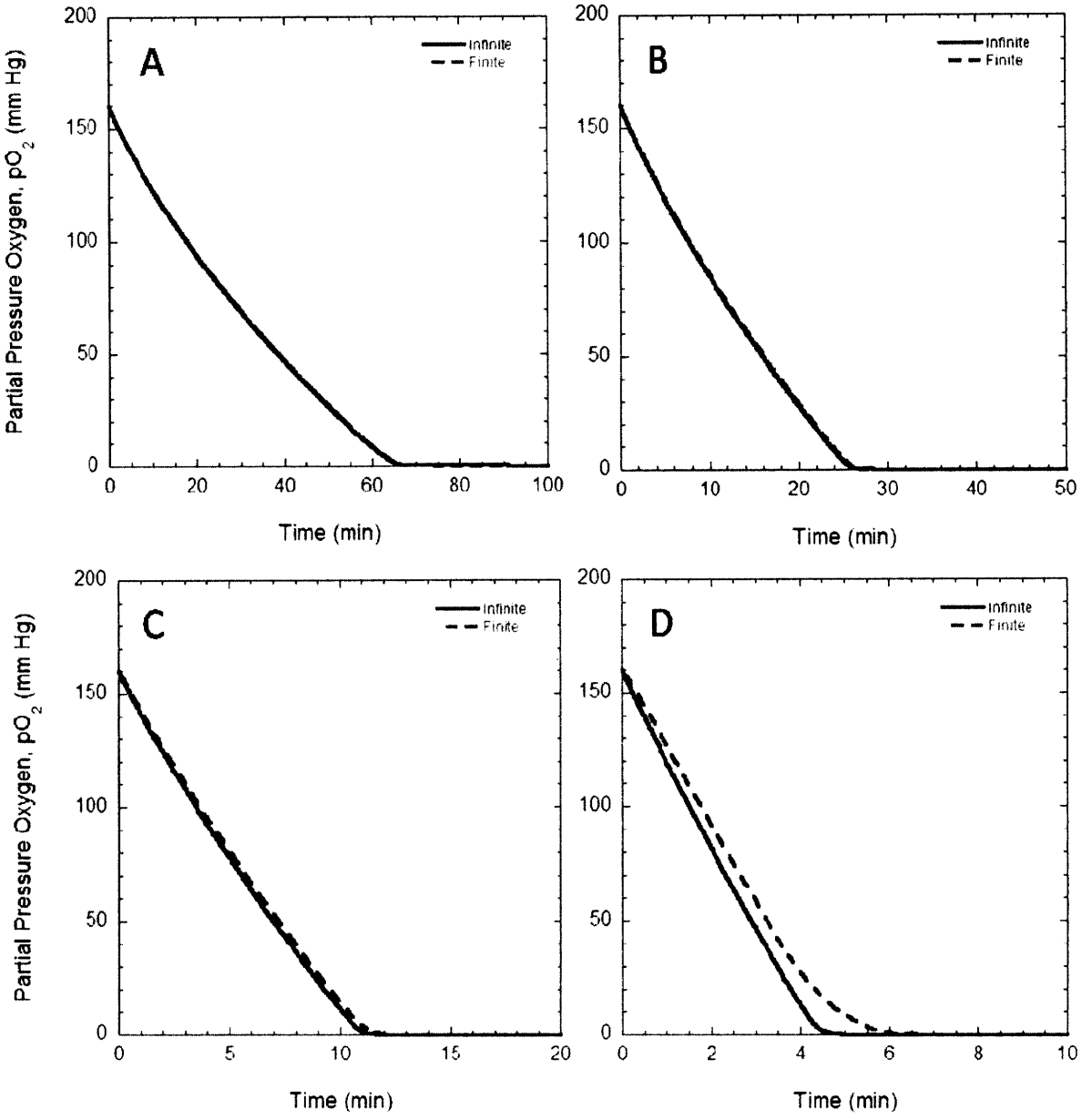

Figure 3.2. Comparison of theoretical transient response where islet tissue is either modeled as infinitely thin (solid blue line) or as a finite slab (dashed red line). The total OCR present in the well is constant between the two models and was specified as (A) 0.5 nmol/min, (B) 1 nmol/min, (C) 2 nmol/min, and (D) 4.4 nmol/min, which is the maximum allowable OCR that allows the islet tissue to remain in a close-packed monolayer. For both models the silicone rubber was 0.24 mm thick and the liquid medium was an equivalent height of 200ul medium.

3.3.3 Effect of Varying Silicone Rubber Thickness

Transient models where silicone rubber thickness was varied showed that thicker silicone rubber slabs dramatically increased the characteristic time of the transient response (Figure 3.3A and B).

The data plotted are from two different total OCR values. Figure 3.3A corresponded to an OCR that was less than the diffusion limitation of the OBS well and it is observed that the transient curves are approaching steady-state at a non-zero pO_2. Figure 3.3B corresponded to an OCR that was greater than the diffusion limitation of the OBS well and it is observed that two of transient curves have already reached a steady-state pO_2 very close to zero and the third is approaching a similar steady-state pO_2. Rappel demonstrated previously that steady-state pO_2 is insensitive to silicone rubber thickness and so we can project that all curves in both figures will approach the same steady-state pO_2. However, the thickness of silicone rubber changed the time length over which the pO_2 dropped from its initial value to its steady-state value.

The rate of change of pO_2 was approximated by performing linear regression about each data point using the three data paints both immediately ahead of and behind that particular point. The rate of change of pO_2 was initially greater in magnitude for thinner silicone rubber slabs and approaches zero (its steady-state value) sooner than for thicker slabs (Figure 3.3C and D). Figure 3.3C is the rate of change Figure 3.3A and represents a situation where the OCR is less than the oxygen diffusion limit of the well. Figure 3.3D is the rate of change of Figure 3.3B and represents a situation where the OCR is greater than the oxygen diffusion limit of the well. The two slope figures are visibly different in that the slopes steadily decreased when the OCR is less than the oxygen diffusion limit, whereas when the OCR is greater than the diffusion limit, the slopes reached a point where they quickly dropped to zero. The time at which they dropped to zero corresponded to pO_2 approaching zero. The two slope figures are also visibly similar in some aspects. The thinnest silicone rubber slab initially has the steepest slope, but it soon crosses over the other curves and approaches zero sooner than for the thicker slabs.

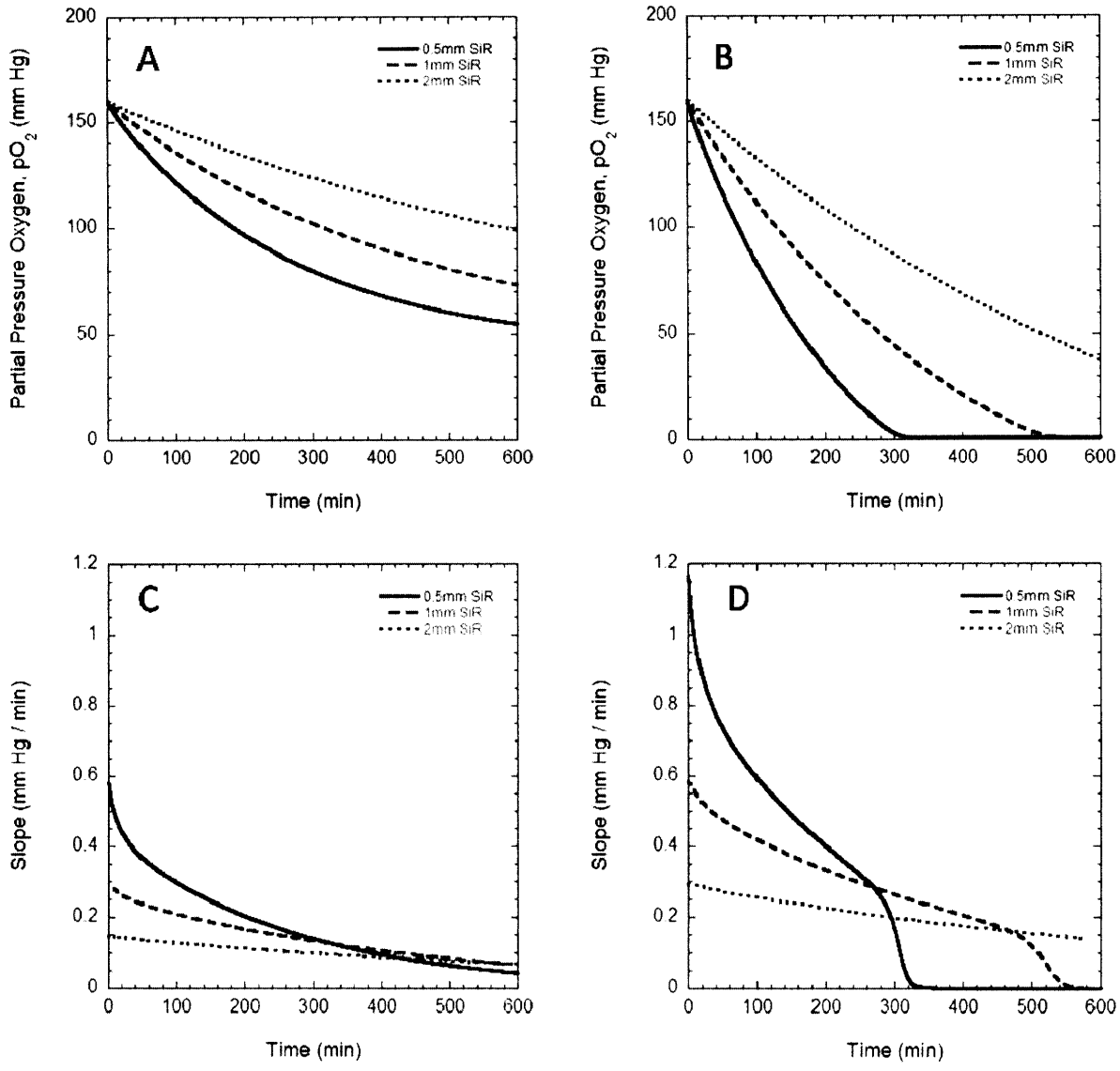

Figure 3.3. Transient response of OBS well with different thickness silicone rubber. (A) and (C) are the partial pressure and slope, respectively, as a function of time when total OCR is less than the oxygen diffusion limit of the well and eventually reaches a non-zero steady-state pO_2 (0.125 nmol/min). (B) and (D) are the partial pressure and slope, respectively, as a function of time when total OCR is greater than the oxygen diffusion limit of the well and goes to zero pO_2 (0.25 nmol/min). The liquid medium depth was the equivalent of 200 ul in a flat bottom 96-well plate (0.6315 cm) for both conditions.

Thicker silicone rubber has a larger reservoir of oxygen for the tissue to consume so the pO_2 within the silicone rubber decreases at a slower rate. A representative plot of pO_2 profiles along the height of the OBS well at various time illustrates the concept of the silicone rubber as an oxygen reservoir (Figure 3.4). The silicone rubber was defined as negatively displaced from 0, while the liquid

medium was defined as positively displaced from 0. The interface between the two phases, x = 0, is consuming oxygen at a constant, specified rate and oxygen diffuses from both phases to meet this consumption requirement. Within 2 minutes, the pO_2 at the base of the silicone rubber (the region farthest from the interface) has already decreased and 'knows' that there is an interface consuming oxygen. However, it is not until approximately 30 minutes that the pO_2 at the top of the medium is affected and 'knows' that the interface is consuming oxygen. This same concept can be illustrated by calculating the characteristic diffusion time for the two phases. The characteristic diffusion time is equal to the square of the height divided by the diffusivity of oxygen in that phase

Eq. 3.23
$$\tau = \frac{h^2}{D}$$

For the model geometry used in Figure 3.4, the characteristic diffusion time of the silicone rubber phase, τ_{si}, is 3 min, while the characteristic diffusion time of the medium phase, τ_{med}, is 240 min. Because τ_{med} is two orders of magnitude larger than τ_{si}, the diffusion gradient within the silicone rubber is established so quickly relative to diffusion in the medium that it can be considered pseudo steady-state. If we look closely at the pO_2 profile within the silicone rubber over time, we see that the magnitude of the gradient does not change significantly over time and that the pO_2 profile simply shifts downward over time. Thus the silicone rubber acts as a reservoir of oxygen where the pO_2 is fairly uniform throughout.

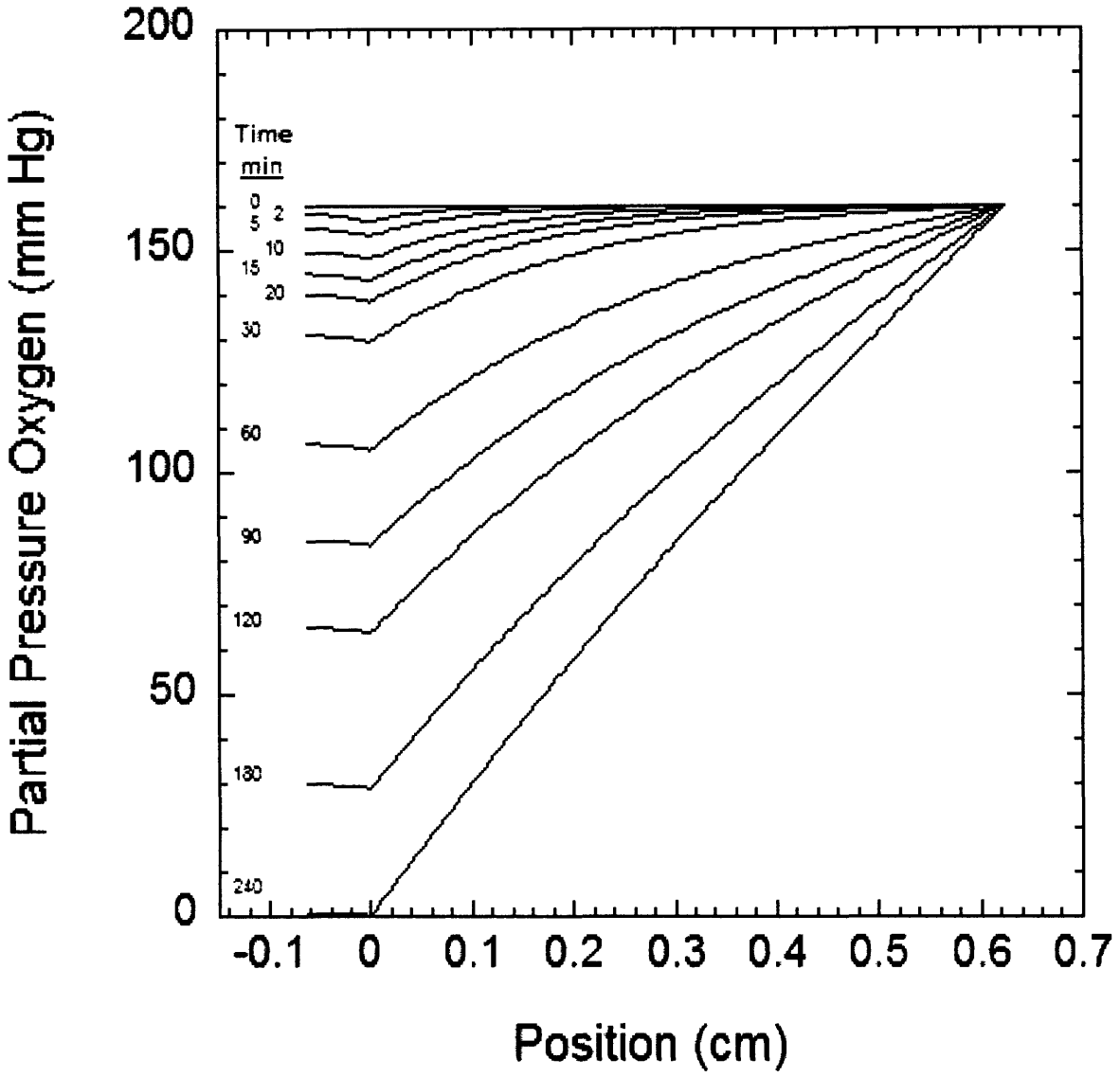

Figure 3.4. pO_2 profiles along the height of the OBS well at selected times where 0 cm is the interface between silicone rubber and liquid medium. The silicone rubber is defined as negative, while the liquid medium is positive in its displacement from 0. The silicone rubber thickness was 0.6 mm, the medium height was an equivalent volume of 200 ul, and the specified total OCR was approximately 0.3 nmol/min.

3.3.4 Effect of Varying Medium Volume (Height)

All theoretical models were 1-D, so the appropriate dimension for any phase was length (or height). However, it was more intuitive to express liquid medium as a volume rather than a height. Therefore, volumetric measures will be used to describe various medium heights, where the volume is equal to the height multiplied by the cross-sectional area.

Theoretical models of various medium volumes demonstrated that its effect was varied and a function of the specified OCR. At steady state, all oxygen being consumed by tissue at the bottom of the well is being transported entirely via diffusion through the liquid medium. The flux of oxygen transporting through the liquid medium at steady state is expressed as

Eq. 3.24
$$N_{O_2,\text{med}} = \frac{D_{O_2,\text{med}}(pO_{2,\text{amb}} - pO_{2,\text{interface}})}{h_{\text{med}}}$$

where $N_{O2,med}$ is the flux of oxygen through the medium at steady-state. This expression for $N_{O2,med}$ is only valid at steady-state when a linear concentration gradient is established across the medium. If sufficient tissue if loaded into the well, the pO_2 at the interface will be zero at steady-state and the flux of oxygen through the medium has reached its maximum value and can be expressed as

Eq. 3.25
$$N_{O_2,\text{med,max}} = \frac{D_{O_2,\text{med}}(pO_{2,\text{amb}})}{h_{\text{med}}}$$

Adding additional tissue will not change the pO_2 at the interface because the flux of oxygen through the medium has reached its maximum and cannot supply the increased oxygen demands of the added tissue. The system is described as 'diffusion-limited' when tissue demand for oxygen reaches the point that it cannot be satisfied at steady-state via diffusion through the medium. Inspection of Eq. 3.25 reveals that the diffusion limited flux if inversely proportional to the height of the medium. Thus the volume of the medium in the OBS determines the oxygen diffusion limit and can dramatically impact both the transient and steady-state behavior.

When tissue OCR was specified as 0.125 nmol/min (Figure 3.5A), the oxygen demand was less than the diffusion limit for medium volumes of 100ul and 200ul (and perhaps 300ul—it is difficult to extrapolate beyond the limit of the graph). The pO_2 gradually decreased to a non-zero steady-state value. The steady-state pO_2 values were different for each medium volume and can be solved by rearranging Eq. 3.24

Eq. 3.26
$$pO_{2,\text{interface}} = pO_{2,\text{amb}} - \frac{N_{O_2,\text{med}} D_{O_2}}{h_{\text{med}}}$$

where $N_{O2,med}$ is equal to the flux of oxygen being consumed by the tissue at the interface and is constant across different medium volumes. The initial rate of change of measured pO_2 was constant for

all three medium volumes. The steady-state pO_2 was approached sooner for smaller medium volumes because the characteristic medium diffusion time (Eq. 3.23) is shorter.

When tissue OCR was doubled to 0.25 nmol/min (Figure 3.5B), the well was diffusion limited for both 200 ul and 300 ul. Only the well with 100 ul was not diffusion limited where the pO_2 reached a non-zero steady-state. Again, the initial rate of change of measured pO_2 was constant across all three volumes. However, with this amount of OCR, the wells with larger medium volumes reached steady-state sooner only because they 'bottomed-out' at $pO_2 = 0$.

When tissue OCR was increased to either 0.5 nmol/min or 1.0 nmol/min (Figure 3.5C and D) all wells were diffusion limited. For 0.5 nmol/min, the well with only 100 ml medium took slightly longer to reach steady-state, however, when the OCR is increased to 1.0 nmol/min, the transient behavior of the system was indistinguishably similar, regardless of medium volume. When the total OCR was this great, the silicone rubber pO_2 reached 0 while diffusion in the medium phase was still semi-infinite for all three medium volumes. Therefore, the transient response was insensitive to medium volume because the diffusion wave had yet to hit the top surface of the medium.

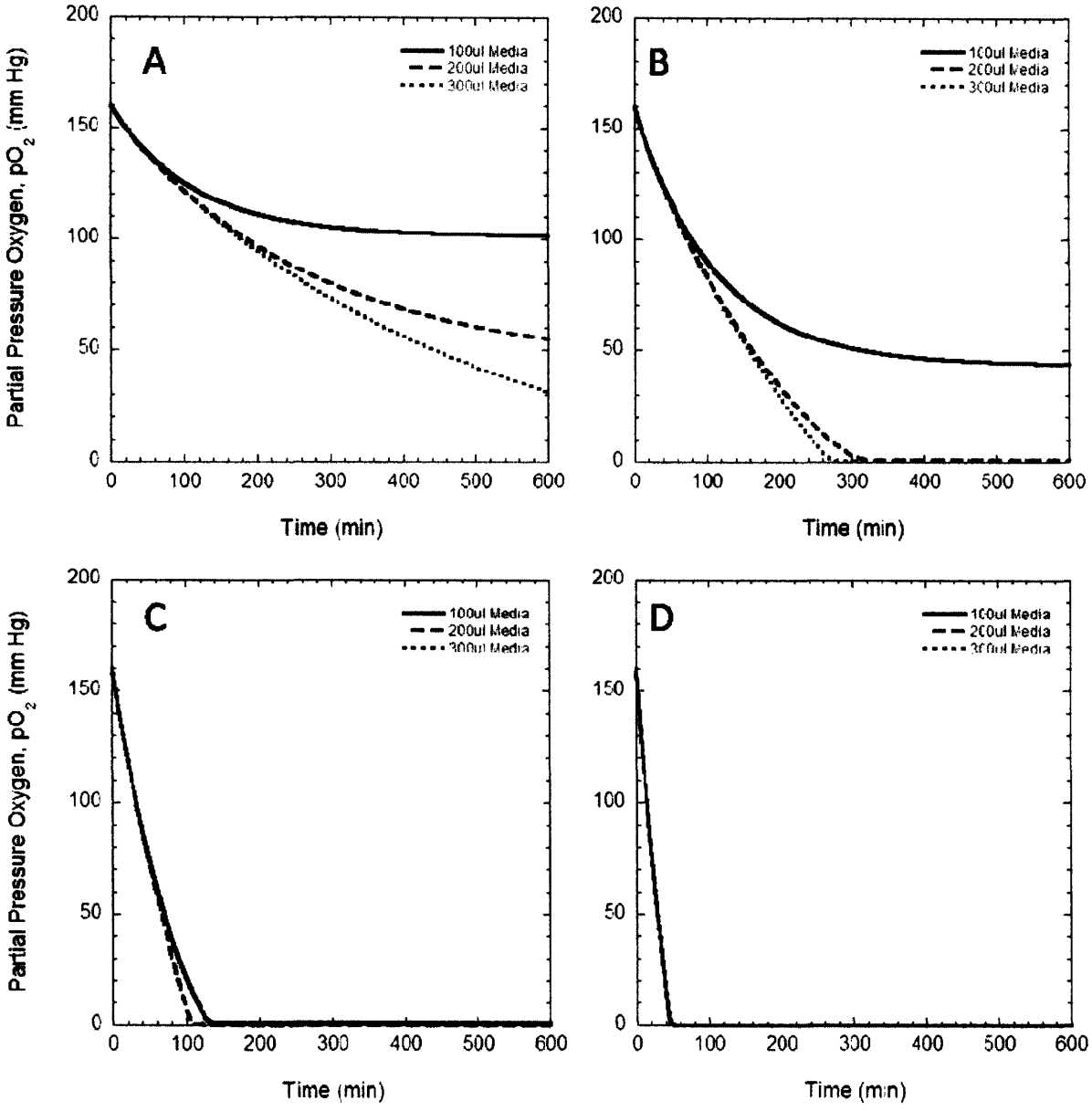

Figure 3.5. Transient response of OBS well where liquid volume (height) is varied. The total OCR of the tissue in the well was (A) 0.125 nmol/min, (B) 0.25 nmol/min, (C) 0.5 nmol/min, and (D) 1.0 nmol/min. The silicone rubber height was 0.63 cm for all simulations.

3.3.5 Effect of varying OCR

Theoretical simulations where total OCR at the infinitely thin interface was varied demonstrated that increasing OCR above a certain threshold caused the pO_2 to decrease to 0 where it remained at

steady-state and further increasing OCR caused the pO_2 to reach 0 faster (Figure 3.6A). The initial rate of pO_2 change was proportional to total OCR. The slope of pO_2 as a function of time decreased sharply with greater total OCR. Therefore the largest total OCR underwent the greatest change in slope and did so in the shortest amount of time.

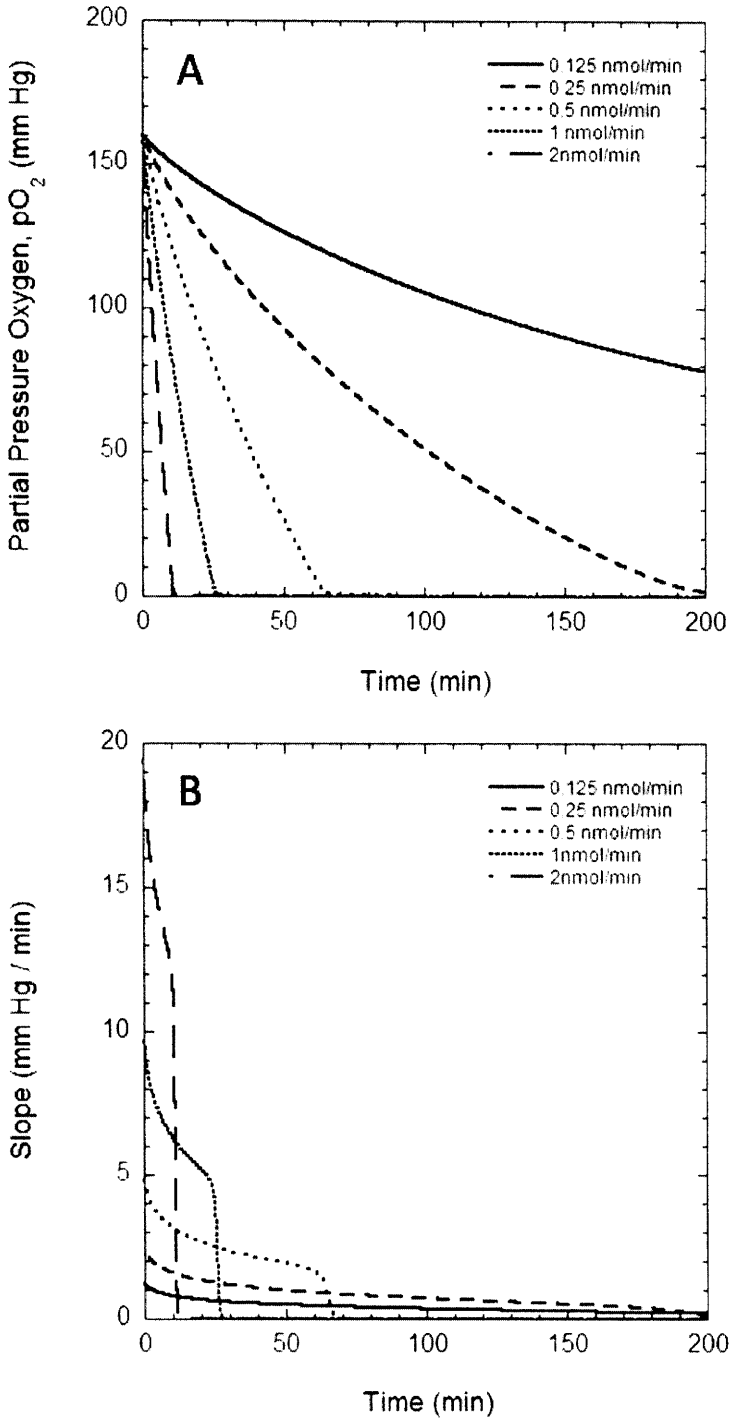

Figure 3.6. Transient response of OBS well where total OCR of the infinitely thin tissue layer is varied. (A) Plot of pO_2 as a function of time. (B) Plot of slope as a function of time where the slope is the rate of pO_2 change as estimated by linear regression. For all simulations the silicone rubber thickness was 0.24 mm and the liquid medium was an equivalent volume of 200 ul.

3.4 Discussion

Geometric analysis of tissue packing provided a rough guide to the amount of tissue that can be loaded into an OBS well while still preserving a monolayer of tissue. Knowing and heeding this limit is helpful to prevent stacking of islets which is likely to cause hypoxia in certain areas of the tissue and ensuing necrotic death. This limiting monolayer surface density is lower for cells as a result of their smaller dimension, although stacking of single cells is less worrisome than islets.

Knowing the maximum allowable surface density for a monolayer enabled us to simulate a close-packed layer of islets with a slab of tissue of finite height to evaluate whether the tissue dimensions significantly change the transient response of OBS or whether the tissue can be accurately approximated as infinitely thin. Theoretical results for the maximally close-packed monolayer indicated that the infinitely thin assumption introduced a small error (~ 10%), however, when less tissue is added to the OBS well, this error decreases and becomes negligible. This finding enabled us to perform additional simulations where the geometry was simplified by assuming infinitely thin tissue.

Theoretical simulations were used to semi-quantitatively evaluate the effect of various experimental parameters, including silicone rubber height, medium height, and total OCR / well. Previous work with steady-state OBS measurements (Rappel) and dry cell-free transient experiments (Chapter 2) suggests that theoretical simulations of OBS experiments will not accurately predict experimental results. Thus, our approach to theoretical modeling has not been purely quantitative in order to match data, but has rather been semi-quantitative where we strive to understand qualitatively how changing parameter values will affect the observed, experimental behavior.

It is important to remember how the data in a transient OBS experiment will be analyzed as we evaluate different parameter's effects in an effort to fine tune experimental parameters to improve the accuracy and practicality of transient OBS measurements. The analysis of transient experiments fits a straight line to a portion of the pO_2 vs. time plot that most appears to be linear and the slope of this line is related to the OCR of tissue in the well. However, theoretical simulations indicated that there is no truly linear portion of the pO_2 vs. time plot and that fitting a straight line is an approximation with no theoretical basis. That is not to say that fitting data with a straight line is useless, but it is important to recognize that selecting this region of greatest linearity is arbitrary. It would be helpful to select parameter values so that it is easier to fit data to a straight line.

A thicker silicone rubber phase will result in a transient response where the slope is relatively constant compared to a thin silicone rubber slab where the initial slope is large and it decreases faster than the thicker slab. The thicker slab is much more forgiving to being fit with a line because the slope will not change dramatically, whereas the thinner slab could yield vastly different linear slopes if different regions of the data are fit. Additionally, a thicker slab would accommodate a wider range of data to be fit well, which would decrease the standard error associated with estimating the slope of a regressed line. However, there are two drawbacks to using a thicker silicone rubber segment: (1) longer experimental time to reach a significant pO_2 drop; and (2) the lower magnitude slope means that data are more susceptible to noise and the signal (i.e. change in pO_2) may not be strong enough to overcome noise. The potential positive and negative effects of thicker silicone rubber segments highlights that choosing an optimal parameter for OBS experiments will balance between competing interests and must be adapted to the purpose and setting of the intended experiment. Lastly, the thickness of silicone rubber may be somewhat limited as commercially produced OBS plates are all the same thickness. As discussed in Chapter 2, attempts to fabricate plates of varying thickness have not improved upon the irregular geometry of the commercial OBS plate. Additionally, fabricating OBS plates can be a time-consuming practice and are most likely not manufactured with the same level of reproducibility as commercial plates.

Increasing the volume in an OBS experiment will typically result in a steeper pO_2 descent, which would be easier to approximate as a line. There is more curvature in the pO_2 vs. time curve when less medium is used. The initial rate of change of pO_2 is independent of medium volume, so obtaining adequate signal strength might not be amenable to varying liquid volume. Generally speaking, when conditions are diffusion limiting, the experiment takes less time and gives a steeper descent rather than a gradual decrease. For these reasons, it is recommended to use at least 200 ul medium so as to improve chances that experiments will be diffusion limited.

More tissue in an OBS experiment will result in a stronger signal (less noise) and will take less time to complete the experiment, however, the range of slopes is greater and it occurs over a shorter period of time. Still, the advantage of a stronger signal and shorter experiment most likely overcome any difficulties associated with fitting data to a line.

4. Empirical Correlation of Transient OBS Data with Accurate OCR Measurements

4.1 Introduction

Transient OBS measurements have previously been used as a measure of relative viability where a sample's transient response was normalized to the transient response of a control. Primary rat hepatocytes were exposed to rotenone or dinuseb and compared to untreated hepatocytes [30]. Human islets were cultured in different glucose conditions and the ratio of the high-glucose slope to the low-glucose slope was defined as the 'OCR Index' [31]. Although these relative measures of viability are reliable and potentially useful measurements, an absolute measurement of OCR would enable more direct comparison of tissue viability across different experiments and potentially between different laboratories. Furthermore, absolute OCR is potentially a meaningful metric itself for certain tissue applications. Papas has demonstrated that the absolute OCR of human islet tissue correlated with diabetes reversal when transplanted in nude mice [2].

Previously, the rate of pO_2 change for one well in a transient OBS experiment has been correlated with the OCR determined with the steady-state pO_2 of that same well, provided that the steady-state pO_2 is non-zero [30, 31]. The relationship between the transient slope and steady-state pO_2 is linear, however, there are limitations associated with this empirically-observed relationship: (1) the time necessary to reach steady-state is long and actual tissue viability might have changed over the course of the measurement; (2) the correlation is limited to measurements where the tissue is not oxygen-starved at steady-state and cannot be used for measurements where more tissue is added to quicken the transient response; and (3) steady-state pO_2 does not give an accurate OCR measurements as shown by Rappel [34].

Theoretical models can be used to explore various assumptions and parameters of OBS experiments, however, they are unable to accurately predict either steady state behavior or dry, transient OBS experiments without tissue present (see Chapter 2). An empirical correlation of transient

OBS measurements with a direct measurement of tissue OCR that is known to be reliable is needed to enable accurate, absolute measurements of OCR using the OBS.

This chapter will analyze transient OBS data in a systematic approach to evaluate the linearity of data and minimize errors associated with fitting data to a least-squares fit line. A similar analysis will be performed on direct OCR measurements taken with a sealed stirred chamber. Lastly, data from these different measures of tissue viability will be related to one another to determine whether a reliable relationship exists between the two so that a calibration curve can be generated to convert from transient OBS data to stirred chamber OCR data. Experiments will be conducted on both islets and cells to determine whether this calibration relationship is independent of tissue geometry.

4.2 Methods

4.2.1 Culture of Cell Lines and Islets

Rat insulinoma INS-1 cells (118), with passage numbers 20-30, were cultured in tissue culture flasks in RPMI medium with 11.1 mM D-glucose (Mediatech, Herndon, VA, USA) supplemented with 10% (v/v) fetal bovine serum (FBS, Mediatech), 100 U/ml penicillin (P3539, Sigma-Aldrich, St. Louis, MO, USA), 100 ug/ml streptomycin (Sigma), 10 mM HEPES (Mediatech), 2 mM L-glutamine (Mediatech), 1 mM sodium pyruvate (Mediatech), and 50 pM P-mercaptoethanol (Sigma).

Rat islets were isolated from male Sprague-Dawley rats by using collagenase digestion/ficoll purification (37, 174). Standard collagenase/protease digestion methods were used for human (4, 33) and porcine (40) isolations. Preparations of rat, and human islets, human non-islet tissue, and porcine islets were provided fresh (4-6 hr after isolation was complete) by the Islet Core at either the Joslin Diabetes Center (Boston, MA) or Massachusetts General Hospital (Boston, MA). Human islets were also received after overnight shipment (sometimes after up to 1 day culture) from other centers contained in 300 ml Permalife bags. When first observed, some preparations were in suspension, some in a pellet. Upon receipt, a portion of the preparation was analyzed and the remainder placed into untreated polystyrene culture flasks at 37oC in a humidified environment (5% CO 2), oxygen partial pressure (pO2) of 142 mmHg, for 34-60 hr during which no medium change occurred.

Islets were cultured in supplemented RPMI (11.1 mM D-glucose, 100 U/ml penicillin, 100 [ug/ml streptomycin, 2 mM L-glutamine, 1 mM sodium pyruvate (all from Mediatech Inc., Herdon, VA), and 50 pM [3-mercaptoethanol (Sigma Aldrich, St. Louis, MO) with 10% fetal bovine serum (FBS, Mediatech Inc.), at low densities (< $8x10^4$ cells/cm^2 or about 50 islet equivalents (IE)/cm^2, where IE is the volume of a sphere with a diameter of 150 um) in 1.3 mm of medium in tissue culture flasks. After culture the free, non-adherent tissue (which is the only tissue used in current practice) was collected. In selected experiments, human tissue attached to the culture vessel (adherent) was incubated for 5 min at 37°C in 0.05% trypsin EDTA (Mediatech Inc.), dislodged with fresh medium, collected and mixed with non-adherent tissue, and stored on ice until used.

4.2.2 Cell Suspension Preparation

INS-I cell suspensions were prepared as previously described [1]. Briefly, the medium was removed from the tissue culture flasks, and 0.05 ml/cm^2 of 0.05% (w/v) trypsin in 0.53 mM EDTA solution (Mediatech) were added and incubated at 37°C for 3 min. Culture medium (0.13 ml/cm^2) was added in order to deactivate the trypsin and cells were detached by gently tapping the flask, collected in a tube, centrifuged at 300 x g for 3 min (AllegraTM 21R Centrifuge, Beckman Coulter), and resuspended in fresh medium. The resulting cell suspensions were stored on ice until used.

4.2.3 Cell and Islet Enumeration by Nuclei Counting

Nuclei were prepared and counted as previously described [1]. Briefly, nuclei were prepared from cells and islets by adding equal 100-ul volumes of sample and of a lysis solution containing 0.1 M citric acid (Sigma) and 1% (v/v) Triton X-100 (Sigma) to a 1.5 ml microtube. The mixture was incubated at room temperature for 5 min with vortex mixing every 1.5-2 min. The islet mixture was then placed in a 1-ml syringe and rapidly forced through a 26G3/8 needle (Becton Dickinson, Franklin Lakes, NJ) 10 consecutive times. Isolated nuclei were diluted with D-PBS to a concentration no higher than 5x10 5 nuclei/ml, stained with 7-aminoactinomycin D (7-AAD, Molecular Probes, Eugene, OR), and then analyzed using a flow cytometer (Guava Personal Cell Analysis (PCA) system, Guava Technologies, Hayward, CA). A conversion factor of 1560 cells / IEQ (Pisania) was used to calculate IEQ from nuclei counting data. Unless otherwise noted, five replicates were taken for nuclei counting.

4.2.3 Oxygen Consumption Rate (OCR) in Stirred Chamber

OCR was measured as previously described [1]. Briefly, islet or cell suspensions in DMEM containing 4.5 g/l glucose and 0.6 g/l L-glutamine supplemented with 100 U/ml penicillin, 100 ug/ml streptomycin, 10 mM HEPES, and no added serum were pipette (350 ul) and sealed in a 200-ul stirred titanium chamber (Micro Oxygen Uptake System, FO/SYSZ- P250, Instech Laboratories, Plymouth Meeting, PA) maintained at 37°C. The time dependent pO_2 within the chamber was recorded with a fluorescence-based oxygen sensor (Ocean Optics, Dunedin, FL). Additional calibration measurements were taken of medium equilibrated with ambient oxygen and 0.1 M sodium sulfite (EMD chemicals, Gibbstown, NJ; 0.126 g in 10 ml double-distilled, sterile water) in order to convert fluorescence to pO_2. Data at high pO_2 were fit to a straight line and the volumetric OCR was evaluated as

Eq. 4.1
$$\frac{OCR(\text{nmol/min})}{vol(\text{ml})} = \alpha \frac{\Delta pO_2}{\Delta t}$$

where α = 1.27 nmol/mmHg-ml is the Bunsen solubility coefficient for oxygen in medium (176).Volumetric OCR measurements were subsequently multiplied by the volume of medium in the OBS well to yield the total OCR within each well. Alternatively, volumetric OCR measurements were normalized by the cell concentration (determined via nuclei counting) to yield the OCR/cell.

4.2.4 Transient OBS Experiments

A fluorescent plate reader (POLARstar, BMG LabTechnologies) was pre-warmed to 37°C for 10 – 15 min after which an empty commercial OBS plate (BD Biosciences, Catalog No: 353830) was loaded into the plate reader for a minimum of 30 minutes to achieve thermal equilibration with the plate reader environment. The plate was read every 5 min to monitor equilibration. When sufficiently equilibrated, a final measurement was taken to serve as an ambient control, I_{amb}, for each well. This ambient control is later used to convert fluorescent intensity to pO_2 as described below. Both excitation (485 nm) and emission (630nm) were directed from underneath the OBS plate to increase proximity of reading to the oxygen sensitive particles embedded within the silicone rubber.

Three samples from the cell or islet suspension were taken for nuclei counting to determine islet or cell concentration of the suspension. A sufficient volume of the suspension was pipetted into one 15 ml centrifuge tube so that there were approximately 8000 IEQ (or 12 x 10^6 cells). The sample was centrifuged at 300 x g for 3 min, culture medium resuspended and replaced with 4-5 ml pre-warmed

DMEM containing no serum as described for OCR measurements in stirred chamber. The sample was serially diluted typically four times into 15 ml centrifuge tubes while leaving at least 2.5 ml of the initial sample for stirred chamber OCR measurement and nuclei counting (1.5 ml) and for the OBS plate (0.8 ml). Unless otherwise noted, serial dilutions were typically 1 – 1.5 ml as they were only used for the OBS plate.

Eight wells of the pre-warmed OBS plate were filled with 200 ul of prewarmed DMEM medium containing no serum to serve as ambient controls. Another eight wells were filled with 200 ul of 100 mM sodium sulfite to serve as anoxic control. The ambient control helps to normalize fluorescence signals that may be changing or drifting not as a direct result of tissue oxygen consumption, but a slower equilibration or signal drift process. The anoxic controls are essential to convert from fluorescent intensity to pO_2 as described below. Four 200 ul replicates of each dilution sample were added to the OBS plate.

Tissue and control samples were added to the pre-warmed plate within 10 min of removing the OBS plate from the plate reader to minimize cooling. The OBS plate was placed in the temperature-controlled plate reader and read at 1.5 min intervals for 200 cycles. The plate reader was configured to only read wells containing tissue or control samples to minimize unnecessary plate movement in order to reduce convection. After loading samples onto the plate and inserting the plate into the plate reader, the initial sample (undiluted) was taken for stirred chamber OCR measurements and nuclei counting. Triplicate OCR measurements were performed serially in one chamber and five 100 ul were taken for nuclei counting.

Calculation of pO_2

Fluorescent intensity measurements from the plate reader were converted to partial pressure of oxygen, pO_2, using the one parameter Stern-Volmer equation

Eq. 4.2
$$\frac{I_0}{I} = 1 + K_{SV}[pO_2]$$

where I_0 is the intensity measurement when no oxygen is present, I is the intensity resulting from the existing pO_2, and K_{SV} is the Stern-Volmer constant, similar to the method described in Chapter 2. In chapter 2 both ambient, I_{amb}, and zero, I_0, measurements were made for each well, whereas now only I_{amb} measurements were made for each well. I_0 measurements were only taken for the eight wells

containing the anoxic control. I_{amb} is used to normalize all intensity measurements for each well to correct for any variations in fluorescence intensity due to real or instrument-perceived variations in the concentration of fluorophore between wells. This adjusted intensity, I', is thus expressed as

Eq. 4.3 $$I' = \frac{I}{I_{amb}}$$

At each time point the mean I' value for the eight medium-containing wells was calculated to serve as a baseline for fluorescent intensity. This baseline intensity was calculated as

Eq. 4.4 $$\overline{I}'_{\text{med}} = \sum_{i=1}^{8} I'_{\text{med,i}}$$

where I'_{med} is the adjusted intensity of the medium-only wells. All I' are subsequently normalized by $\overline{I}'_{med}$, resulting in a normalized fluorescence, N, expressed as

Eq. 4.5 $$N = \frac{I'}{\overline{I}'_{\text{med}}}$$

where N represents the fluorescent signal relative to negative-control wells and should remove drift due to temperature changes or equilibration, excitation light intensity. The mean N value for the medium-containing wells is by definition equal to 1 at every time point. The maximum increase in relative fluorescent intensity occurred in the anoxic control wells after sufficient time had elapsed for all oxygen to be quenched (typically 1 hr) at which time the relative fluorescent intensity reaches a plateau. $\overline{N}_0$ is defined as the average maximum relative fluorescent signal and is calculated by averaging across the time that the signal plateaus and across all eight anoxic control wells. The left hand side of the Stern-Volmer equation (Eq. 4.2) can now be modified as follows

Eq. 4.6

Divide top and bottom by I_{amb}

$$\frac{I_0 / I_{amb}}{I / I_{amb}} = \frac{I_0'}{I'}$$

Divide top and bottom by $\overline{I}'_{med}$

$$\frac{I_0' / \overline{I}'_{med}}{I' / \overline{I}'_{med}} = \frac{N_0}{N}$$

where N_0 would the relative signal at anoxic conditions for that particular well. This modification of the Stern-Volmer equation has not invoked any assumptions and is true for each well. Because N_0 is not directly measured for every well it is assumed that there is sufficiently little well-to-well variability that N_0 is relatively constant across wells. Therefore the average anoxic signal, $\overline{N}_0$, can be substituted for N_0, which yields the modified Stern-Volmer equation:

Eq. 4.7

$$\frac{\overline{N}_0}{N} = 1 + K_{SV}[pO_2]$$

The same Stern-Volmer constant, K_{SV}, is calculated at ambient pO_2, where N is by definition equal to 1, by rearranging the Eq. 4.7 to yield

Eq. 4.8

$$K_{SV} = \frac{\frac{\overline{N}_0}{1} - 1}{pO_{2,amb}}$$

where $pO_{2,amb}$ is the ambient pO_2, which we assume constant at 160 mm Hg. The pO_2 in each well at every time point is then calculated by the expression

Eq. 4.9

$$pO_2 = \frac{\frac{\overline{N}_0}{N} - 1}{K_{SV}}$$

4.2.5. Slope Analysis of Transient OBS Data

Two methods were employed to estimate the slope from transient OBS data. The first method has been described previously [31]. Briefly, the slope of the least-squares fit to pO_2 data between 20

and 60 min was determined using linear regression (EXCEL, Microsoft, Redmond, WA) and reported with a standard error associated with the estimate of the slope. The time window was adjusted as necessary for conditions where the pO_2 decreased to 0 before 60 min had transpired. In such instances, only the visibly linear portion of the pO_2 data was being fit with a line.

The second method took a more systematic approach estimating the slope of data by adjusting the size of the time range to be fit with a least-squares fit. The smallest time window looked at only 3 data points to fit the line at any given time: the time point of interest, the time point preceding it, and the time point following it. As measurements were made every 1.5 min, the time window this analysis was 3 min. This particular method of analysis will hereafter be referred to as the '3 min window'. Similar analysis was performed with windows of 6, 15, 30, 45, 60, 90, 120, and 180 minutes. The standard error associated with each individual fit's slope was also determine using EXCEL.

The slope was estimated individually for each well at every time point where there was data to fill the entire time window. For example, the first estimate of the slope for a 3 min window analysis is centered around the time point 1.5 min. Similarly, the first estimate of the slope for a 15 min window analysis is centered around 7.5 min. As the time window of analysis is increased, the slope is only estimated for time points towards the center of the data, whereas there are no estimates for time points at the beginning or endpoint of the experimental data.

At every time point for every well and for each analysis time window the standard error of the slope estimate was divided by the absolute magnitude of the slope to yield a % error. For a given well and analysis time window, all time points were compared to determine the minimum % error. This was then repeated for the different analysis time windows. Eventually the value of the minimum % error was plotted against the width of the time window for all replicates of one condition. The shape of this minimum % error vs. time window curve was concave and the time window corresponding with the minimum of this curve was identified. That time window was then used for each well to identify the maximum slope across all time points. The maximum slope for all four replicates was averaged. Thus the final slope reported is the maximum slope for that particular time window which minimizes the error of the least-squares fit. Hereafter, it will simply be referred to as the maximum slope for each condition.

4.2.6 Statistical Analysis

Linear regression was performed in EXCEL (Microsoft, Redmond, WA) to determine estimates and standard errors for both the slope and intercept of a best-fit line. For any linear correlation, The estimated value of y when $x=x^*$, is given by

Eq. 4.10 $$\hat{y} = \hat{\beta}_0 + \hat{\beta}_1 x^*$$

where $\hat{\beta}_0$ is the intercept estimate and $\hat{\beta}_1$ is the slope estimate.

When OBS slope data was empirically correlated with stirred chamber OCR measurements, linear regression was performed as mentioned previously. Additionally, prediction intervals were generated using a well-established method to predict the possible limits of the calibration relationship [39]. Briefly, a prediction interval for a defined 100(1-α)% confidence level was calculated at every value of x=x* by the expression

Eq. 4.11 $$Y = \hat{y} \pm t_{\alpha/2,n-2} \cdot s_{\hat{y}}$$

where $t_{\alpha/2,n-2}$ is the t-statistic for α/2 with n-2 degrees of freedom (n is the total number of measurements) and $s_{\hat{Y}}$ is the standard deviation associated with estimate of Y. The standard deviation associated with the estimate of Y, $s_{\hat{y}}$, is given by

Eq. 4.12 $$\hat{s}_Y = \sqrt{s^2\left(1+\frac{1}{n}\right)+s_{\beta 1}^2\left(x^*-\overline{x}\right)^2}$$

where s is the standard error of all measurements, $s_{\beta 1}$ is the standard error of the slope estimate, and $\overline{x}$ is the average x-value of all measurements.

Two different prediction intervals were determined for each linear correlation. A prediction interval with 95% (α = 0.05) confidence was generated as well as a 68.3% confidence interval (α = 0.317). A confidence level of 68.3% was chosen because it represents the percentage of data falling within one standard deviation on either side of the mean in a normal distribution.

4.3 Results

4.3.1 Transient OBS Data and Analysis

Relative fluorescent intensity increased sharply to reach a maximum plateau for conditions where the tissue OCR was high enough for the well to be diffusion-limited, whereas loading lower amounts of tissue could result in a fluorescent intensity that gradually rises and after a significant amount of time reaches steady-state value (Figure 4.1A). The pO_2 data converted from fluorescent intensity inversely mirror this transient behavior where the pO_2 dropped sharply to 0 when lots if tissue was loaded into the well and gradually decreased to a non-zero steady-state pO_2 (Figure 4.1B). For non-zero steady-state conditions, oftentimes pO_2 would not remain constant at its steady-state value, but instead reach a minimum and begin to increase. This phenomenon was a result of tissue dying over time so that the total OCR within the well actually decreased over time. This problem was more of a concern when low amounts of tissue were added because the time to reach non-zero steady-state often was over 3-4 hr. However, when lots of tissue was present, the pO_2 would drop steeply to 0 often within 1 hr. This phenomenon highlights the importance of adding sufficient tissue for transient OBS measurements.

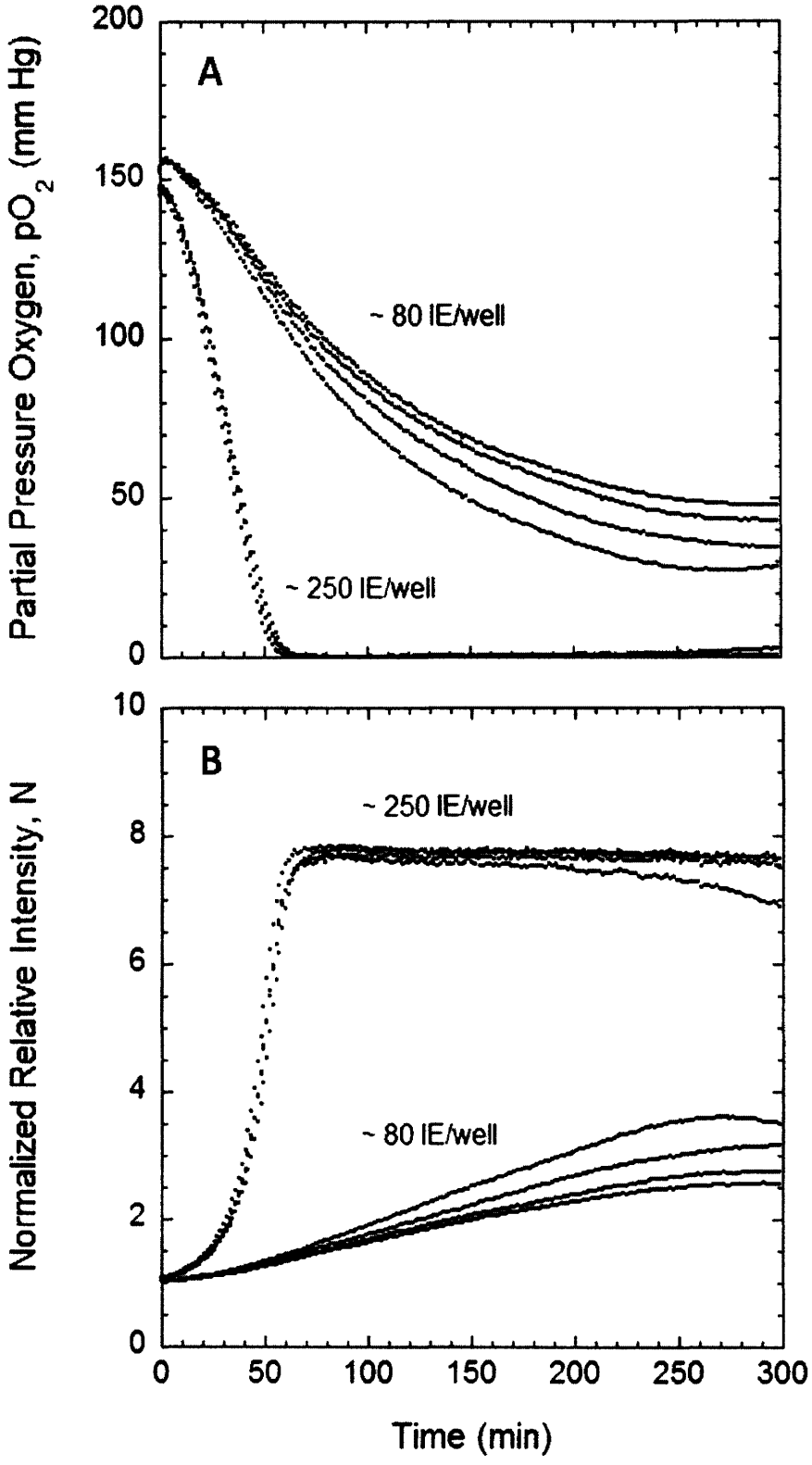
A
B
Partial Pressure Oxygen, pO_2 (mm Hg)
Normalized Relative Intensity, N
Time (min)
~ 80 IE/well
~ 250 IE/well
~ 250 IE/well
~ 80 IE/well
200
150
100
50
0
10
8
6
4
2
0
0
50
100
150
200
250
300

Figure 4.1. Representative plots for transient OBS measurements at two loading concentrations of (A) relative fluorescence and (B) converted pO_2. Each condition had 4 replicates. Data from fresh rat islets (7/16/08).

Closer examination of the early transient data (Figure 4.2) reveals discrepancies between experimental data and theoretical predictions (see Chapter 3 for methodology and figures of theoretical predictions). Theory predicted that the greatest rate of pO_2 change occurred right at t = 0, however, experimental pO_2 had the steepest rate of change usually 20 – 60 min after tissue was added to the OBS plate and fluorescent intensity began to be measured. This could be a result of the time necessary for tissue to settle to the bottom of the OBS well. Theoretical models assumed all tissue was localized to the bottom of the well at t = 0, but when tissue is first added to the well tissue is dispersed throughout the liquid medium and will settle to the bottom over time. The pO_2 in wells with small amounts of tissue would often initially rise before beginning to decrease. These qualitative discrepancies between theoretical simulation and experimental data underscore the difficulty of accurately predicting experimental results from theory and the need for an empirical correlation between transient OBS measurements and the stirred tank OCR measurement.

Estimating the slope of pO_2 data with fixed width time windows revealed that the slope is not constant, but that its magnitude peaked usually between 20 and 60 min and then decreased until reaching 0 and the well was at steady-state (Figure 4.3 A). The maximum slope was greater and the peak was sharper for conditions with more tissue. The fractional error associated with estimating the slope reached a minimum at the same point that the slope peaked, which is not surprising given that the fractional error is by definition normalized by the slope (Figure 4.3B). The magnitude of the minimum error was smaller for conditions with more tissue. Also, the sharpness of the minima was great when more tissue was loaded into the OBS well.

The value of the fractional error minimum for each time window analysis was plotted versus the width of the time window (Figure 4.4). The shape of this curve was concave and there a minimum associated with a particular time window. The concavity of the curve was deeper for samples where more tissue was present. For each sample condition, the time window where this minimum occurred is referred to as the optimal time window. The optimal time window was larger for samples where less tissue was present and this trend was generally observable over a large number of experiments (Figure 4.5).

For each sample condition the optimal time window was determined and the maximum slope associated with that time window was averaged across all four replicates. The averaged slope is referred to simply as the maximum slope and was the final output of transient OBS analysis.

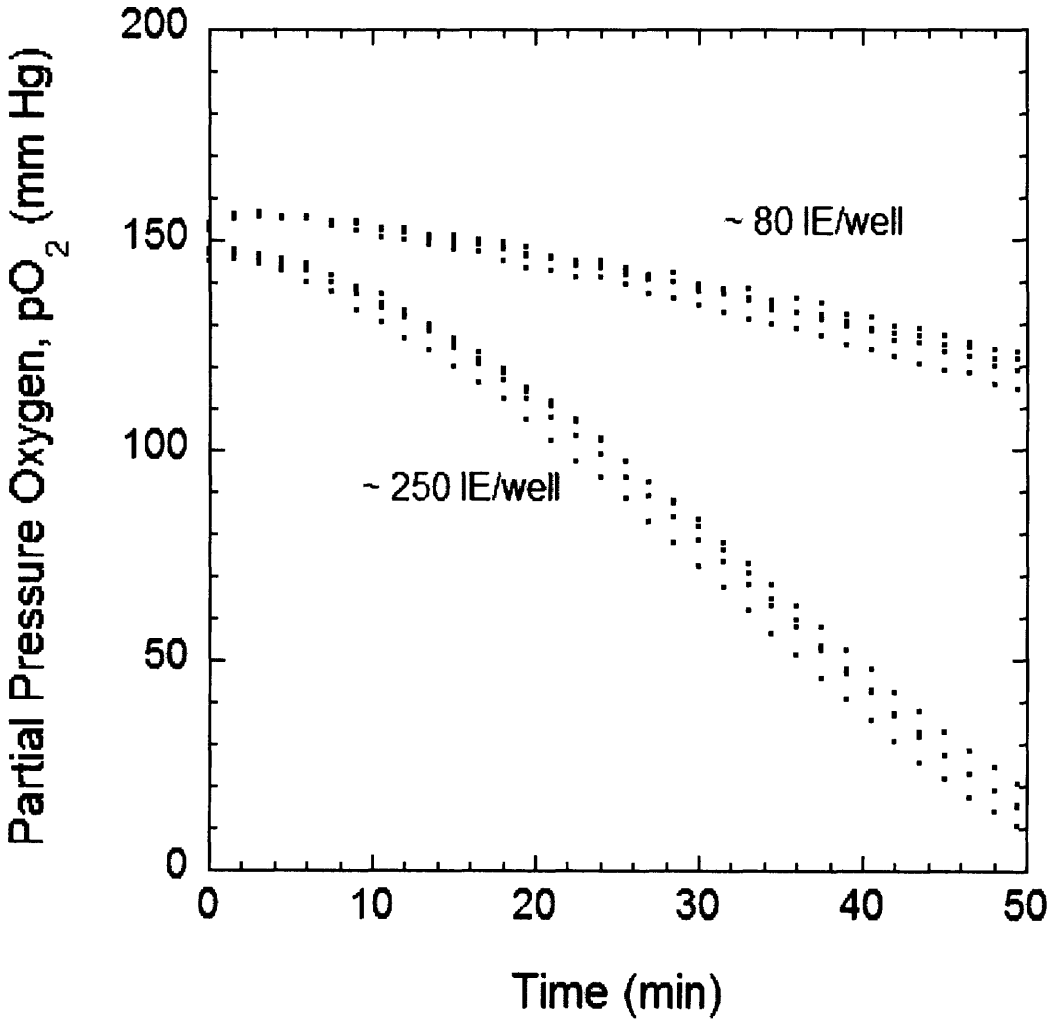

Figure 4.2. Early time transient pO_2 profile for rat islets (7/16/08) at two loading concentrations (n = 4).

Alternatively, the transient slope was estimated using the method where all data from 20 – 60 min were fit with a line. For conditions where the pO_2 reached 0 before 60 min this window was accordingly adjusted. Comparing the slope obtained with this method to the maximum slope reveals that the 20 – 60 min method is hardly distinguishable from the more involved maximum slope analysis

(Figure 4.6). When plotted against each other the slope is 0.979 ± 0.005, where the slope would be 1 if the two methods were exactly similar.

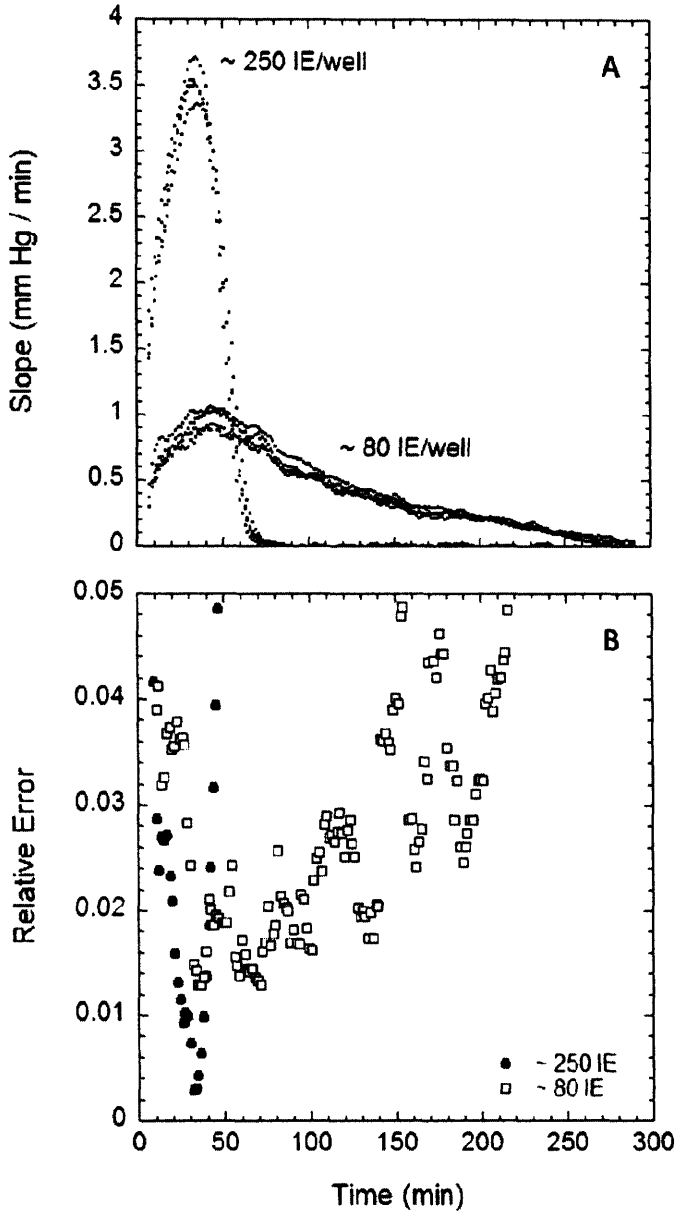

Figure 4.3. Representative analysis of two sample loadings (n = 4) using a 15 min window. (A) Slope of least-squares fit through 15 min data surrounding each time point. (B) Relative error associated with estimating the slope. Data from fresh rat islets, 7/16/08.

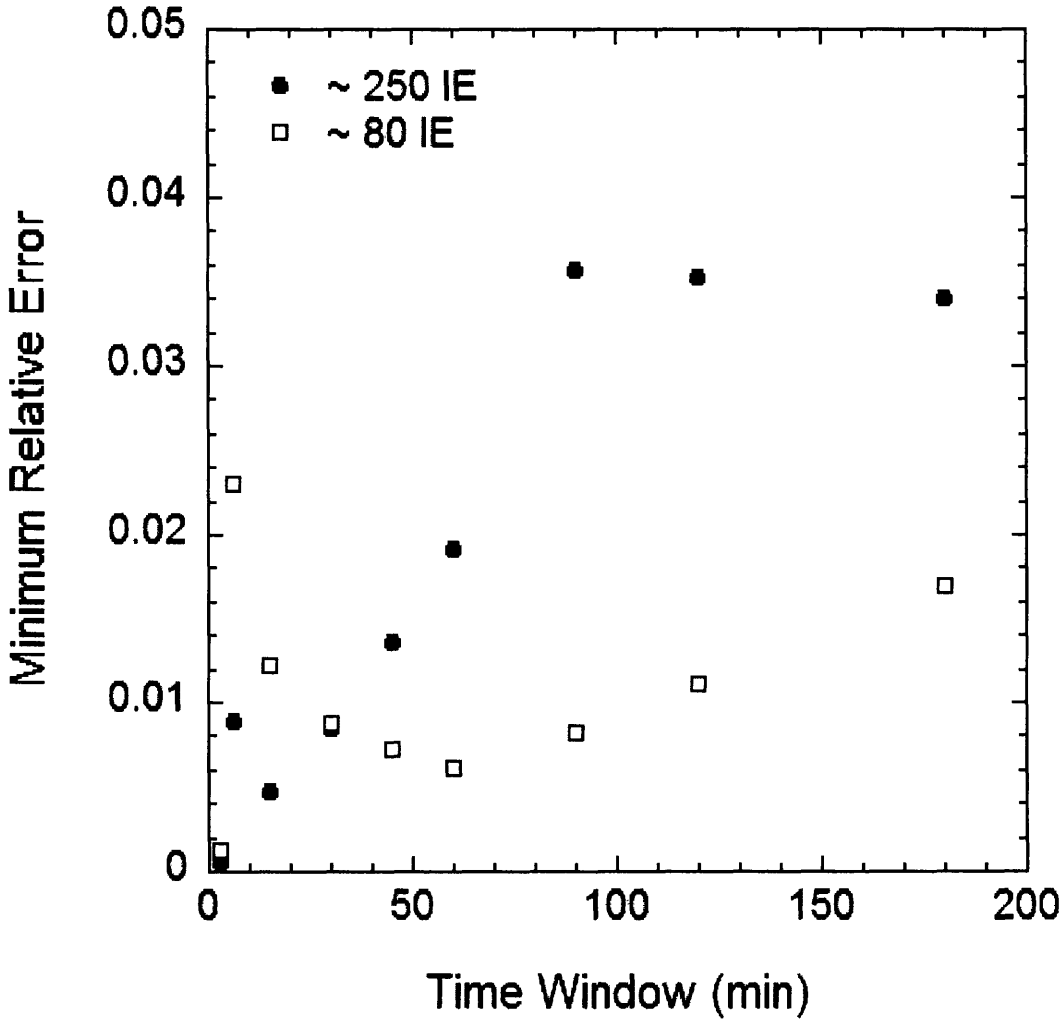

Figure 4.4. Minimum fractional error when estimating transient slope as a function of the analysis time window slope for two loading concentrations (n = 1). For the 250 IE data, there was a minimum at 15 min; for the 80 IE data, there was a minimum at 60 min. Data are from rat islets, 7/16/08.

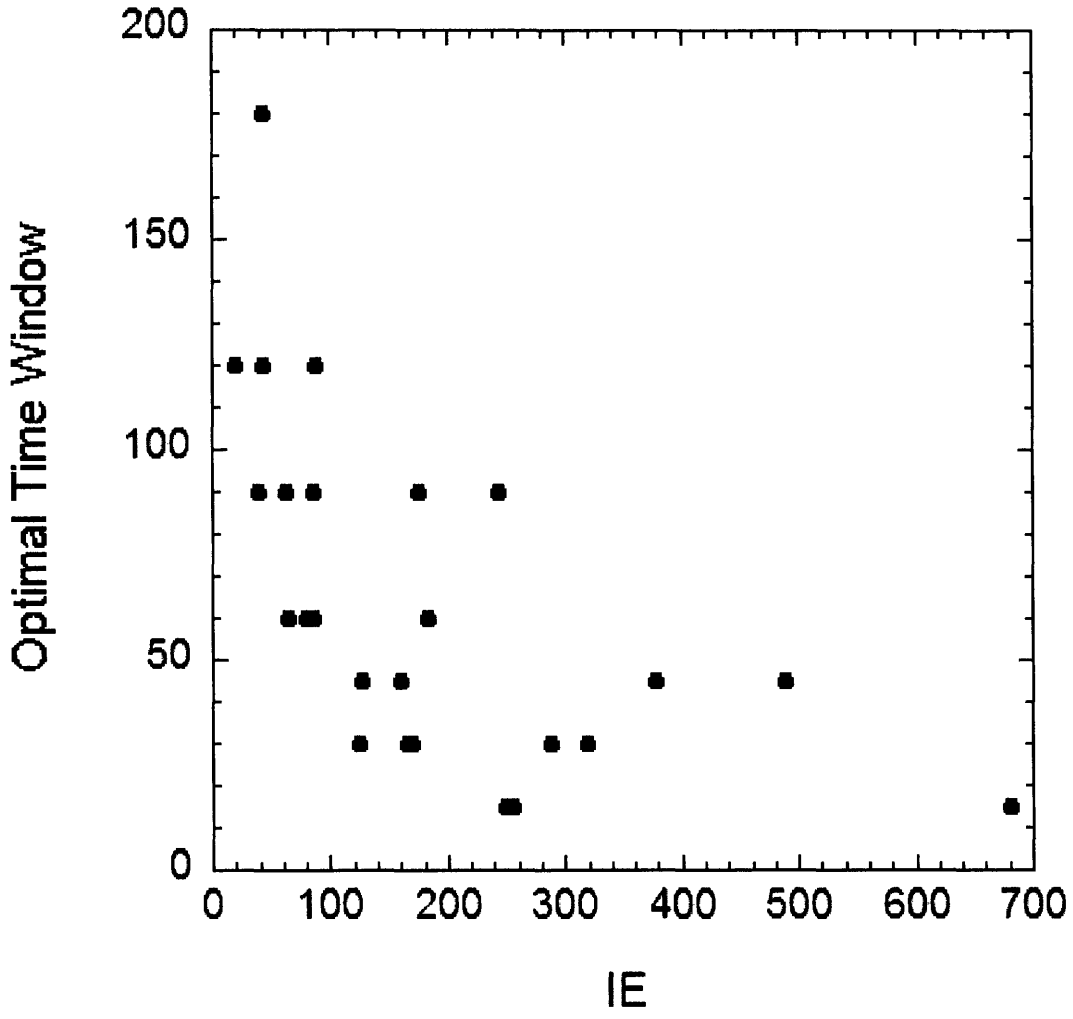

Figure 4.5. Optimal time window as a function of IE. As more tissue is loaded, the optimal time window for analysis decreases.

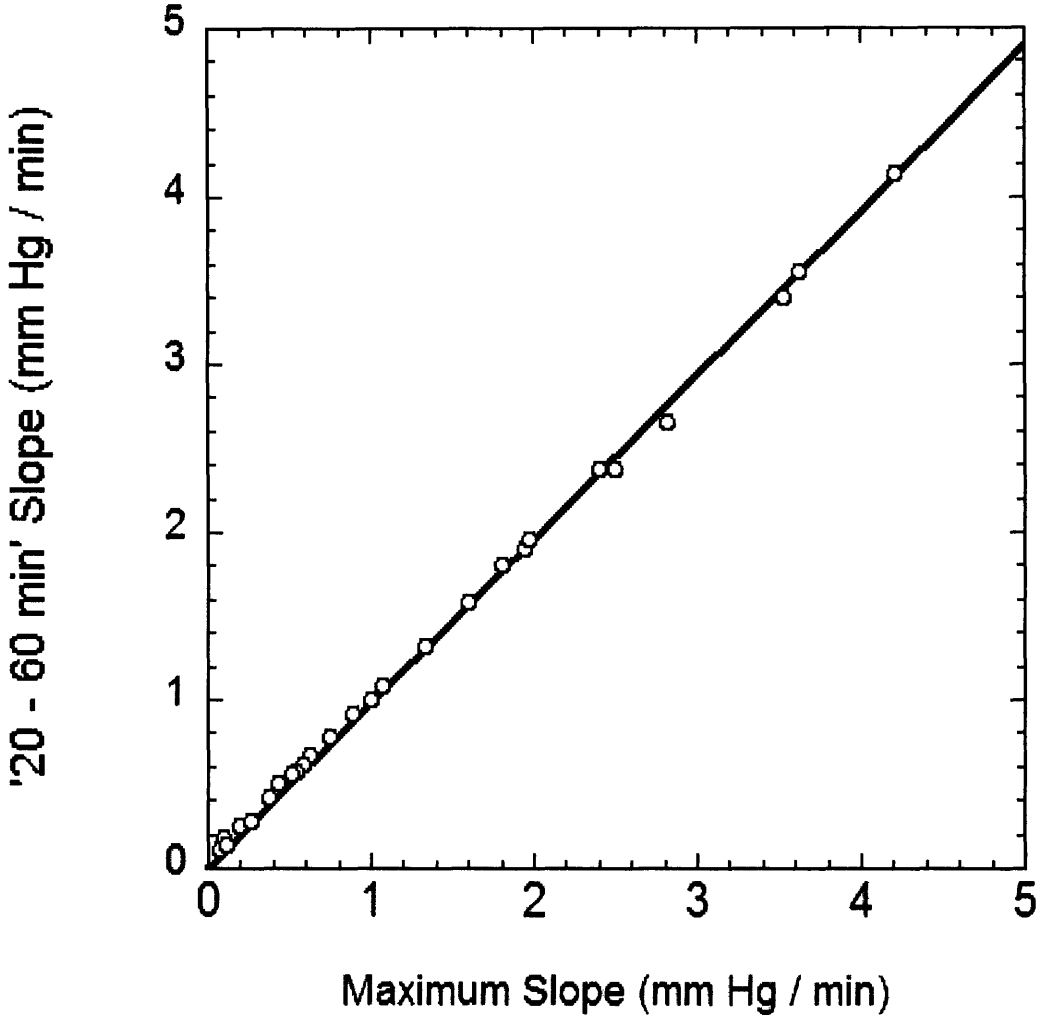

Figure 4.6. Correlation between two methods to determine transient slope from OBS data. The equation of the line is $Slope_{20\text{-}60} = (0.979 \pm 0.004)Slope_{Max}$, where two exactly equivalents methods would yield a coefficient of 1. Data from both islets and INS-1 cells.

4.3.3. Analysis of Stirred Chamber OCR Measurements

A similar analysis of stirred chamber OCR measurements was performed to contrast the stirred chamber measurement with transient OBS measurements. Triplicate measurements of tissue were performed in series, where each measurement required approximately 20 min (Figure 4.7). The stirred chamber required significant time before t = 0 to equilibrate with ambient oxygen conditions and an additional 20 min after the last OCR measurement to quench the chamber with 0.1M sodium sulfite

(data not shown). The total time required to perform stirred chamber measurements from start to finish was approximately 3 hr.

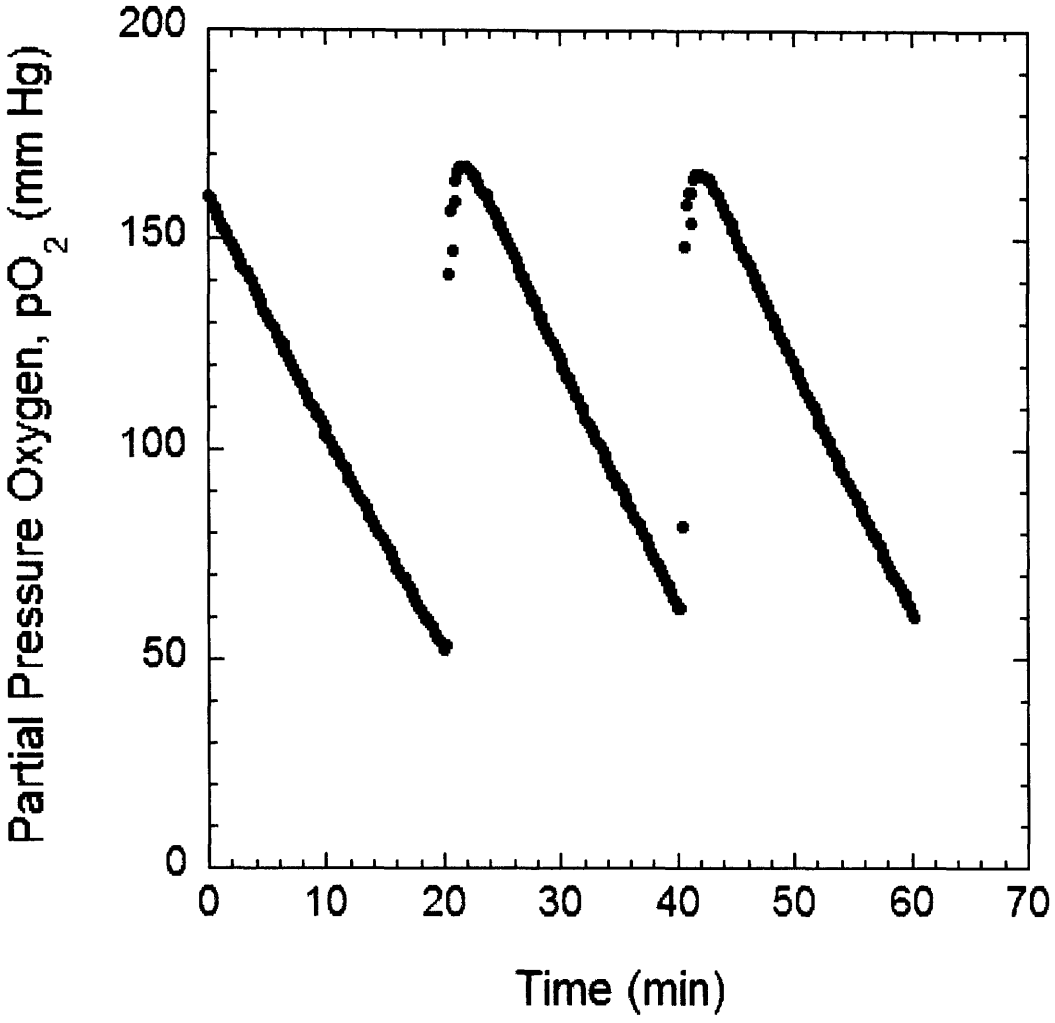

Figure 4.7. Serial OCR measurements in stirred chamber. The samples contained ~ 250 IE. Data taken from fresh rat islets 7/18/08.

The slope of each measurement was estimated with a least-squares fit spanning data from 160 mm Hg to 50 – 60 mm Hg (Figure 4.8). The fractional error associated with such slope estimates typically ranged from $1x10^{-3} - 5x10^{-3}$. The slope was estimated using different time windows so that the data being fit didn't span completely from 160 mm Hg to 50 – 60 mm Hg (Figure 4.9A). Over time the slope decreased 9.4%, 6.7%, and 3.8% for 5 min, 10 min, and 15 min windows, however, this magnitude decrease has less to do with improved fitting and more to do with simply less time points being analyzed

for the larger time windows. The goodness of fit can be assessed by determine the relative error, which is the standard error divided by the slope magnitude (Figure 4.9B). As expected, the error decreases as more data are included to estimate the slope of a least-squares fit line.

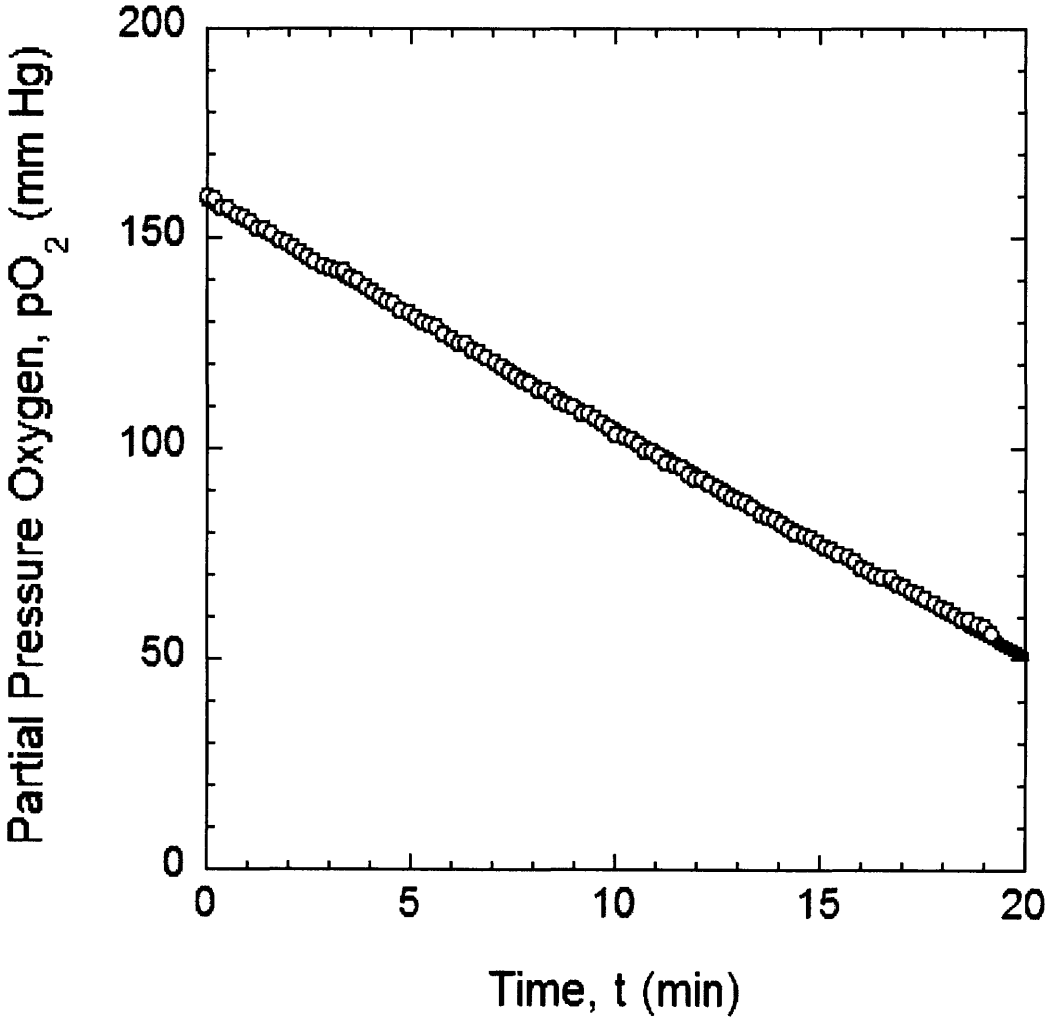

Figure 4.8. Stirred chamber pO_2 data from 1st of 3 serial dilutions. The least-squares fit spanned the entire plotted data range from 160 mm Hg to 50 mm Hg and yields the relationship $pO_2 = (-5.387 \pm 0.014)t + (1864 \pm 4)$. Data from fresh rat islets (7/18/08).

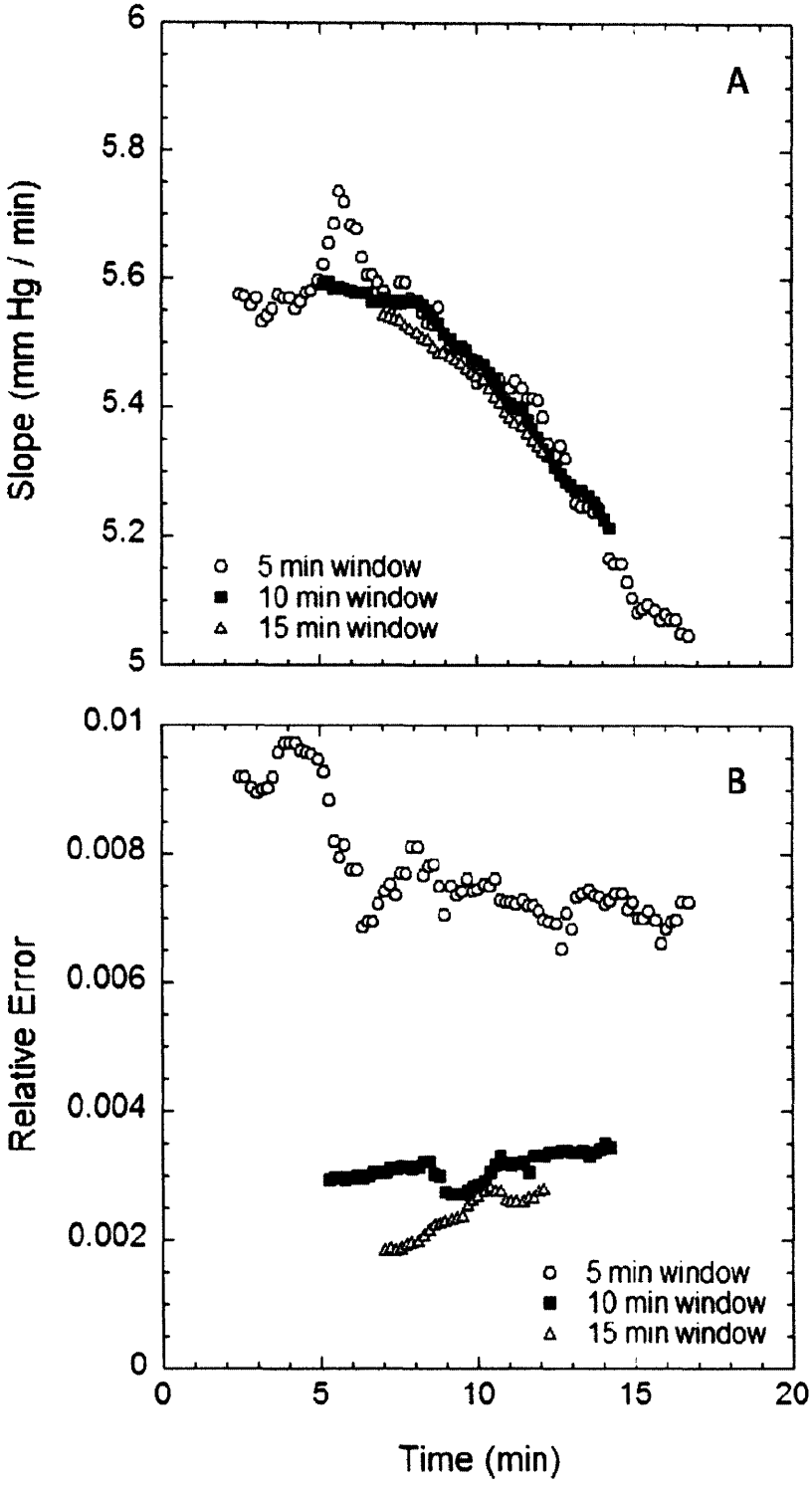

Figure 4.9. Data analysis of stirred chamber OCR measurement. (A) Rate of pO_2 change over time for given time windows. (B) Relative error associated with estimating the slope. Data taken from fresh rat islets (7/18/08).

4.3.4 Calibrating OBS Transient Slope with Stirred Chamber OCR Measurement

Stirred chamber OCR measurements were conducted in parallel with transient OBS measurements for both INS-1 cells (Table 4.1) and islets (

Table 4.2). OCR measurements were initially expressed as consumption rate per volume (nmol / min ml) and then multiplied by the volume of medium in each OBS well (0.2 ml) to yield the total OCR (nmol / min) within each well. Nuclei measurements were similarly determined on a volume basis and then multiplied by medium volume to yield the total number of cells (or IE when divided by 1560 cells / IE).

It should be noted that OCR and nuclei measurements were only performed on the most concentrated sample and then calculations were extended to more dilute samples by the use of dilution factors, except for human islet experiments on 6/28/2008. Data from islet experiments on 6/28/2008 indicate that dilutions were trustworthy and extrapolating from one measurement to multiple via dilution factors did not introduce significant error (Figure 4.10).

Table 4.1. INS-1 Cell Data

Date	Cells ($\times 10^5$)	OCR nmol / min (n = 3)		Maximum Slope mm Hg / min (n = 4)	
7/12/2008	5.2	1.09	± 0.13	2.98	± 0.09
	2.6	0.55	± 0.07	1.30	± 0.01
	1.3	0.27	± 0.03	0.54	± 0.01
	0.7	0.14	± 0.02	0.21	± 0.01
	0.3	0.07	± 0.01	0.07	± 0.01
7/15/2008	10.2	2.28	± 0.05	7.57	± 0.09
	6.8	1.52	± 0.03	4.67	± 0.10
	5.1	1.14	± 0.02	3.34	± 0.04
	3.4	0.76	± 0.02	1.96	± 0.09
	2.6	0.57	± 0.01	1.30	± 0.18
7/17/2008	8.6	2.14	± 0.08	6.97	± 0.18
	5.8	1.43	± 0.06	4.18	± 0.05
	4.3	1.07	± 0.04	3.04	± 0.08
	2.9	0.71	± 0.03	1.69	± 0.01
	2.2	0.54	± 0.02	1.15	± 0.02
	1.4	0.36	± 0.01	0.63	± 0.02
	1.1	0.27	± 0.01	0.44	± 0.01

Table 4.2. Islet Data

Date	Source	Species	IE	OCR nmol / min (n=3)			Maximum Slope mm Hg / min (n=4)		
6/27/2008	MGH	Human	488	0.39	±	0.11	1.59	±	0.16
			244	0.20	±	0.05	0.62	±	0.13
			175	0.13	±	0.04	0.44	±	0.01
			87	0.06	±	0.02	0.20	±	0.01
			44	0.03	±	0.01	0.07	±	0.01
6/28/2008	MGH	Human	680	0.93	±	0.20	3.63	±	0.36
			377	0.51	±	0.12	1.81	±	0.21
			182	0.29	±	0.04	0.76	±	0.15
			85	0.11	±	0.01	0.37	±	0.04
			42	0.05	±	0.00	0.10	±	0.02
7/4/2008	Miami	Human	319	0.79	±	0.10	2.50	±	0.36
			159	0.40	±	0.05	1.00	±	0.09
			80	0.20	±	0.02	0.58	±	0.12
			40	0.10	±	0.01	0.26	±	0.16
			20	0.05	±	0.01	0.11	±	0.07
7/7/2008	Miami	Human	287	0.81	±	0.19	2.82	±	0.27
7/16/2008	Joslin	Rat	255	1.11	±	0.18	3.52	±	0.15
			170	0.74	±	0.12	1.95	±	0.08
			127	0.56	±	0.09	1.33	±	0.07
			85	0.37	±	0.06	0.90	±	0.08
			64	0.28	±	0.04	0.55	±	0.02
7/18/2008	Joslin	Rat	249	1.50	±	0.08	4.21	±	0.42
			125	0.75	±	0.04	1.97	±	0.77
			166	1.00	±	0.05	2.40	±	0.42
			83	0.50	±	0.03	1.08	±	0.10
			62	0.38	±	0.02	0.52	±	0.19

For INS-1 cells, the coefficient of variation was 5.7% for stirred chamber OCR measurements and 3.1% for transient OBS slope measurements. For islets, the coefficients of variation were 16.2% and 17.2% respectively. The increased variability of islet measurements is consistent with past results indicating the difficulty of sampling islets (Papas REF).

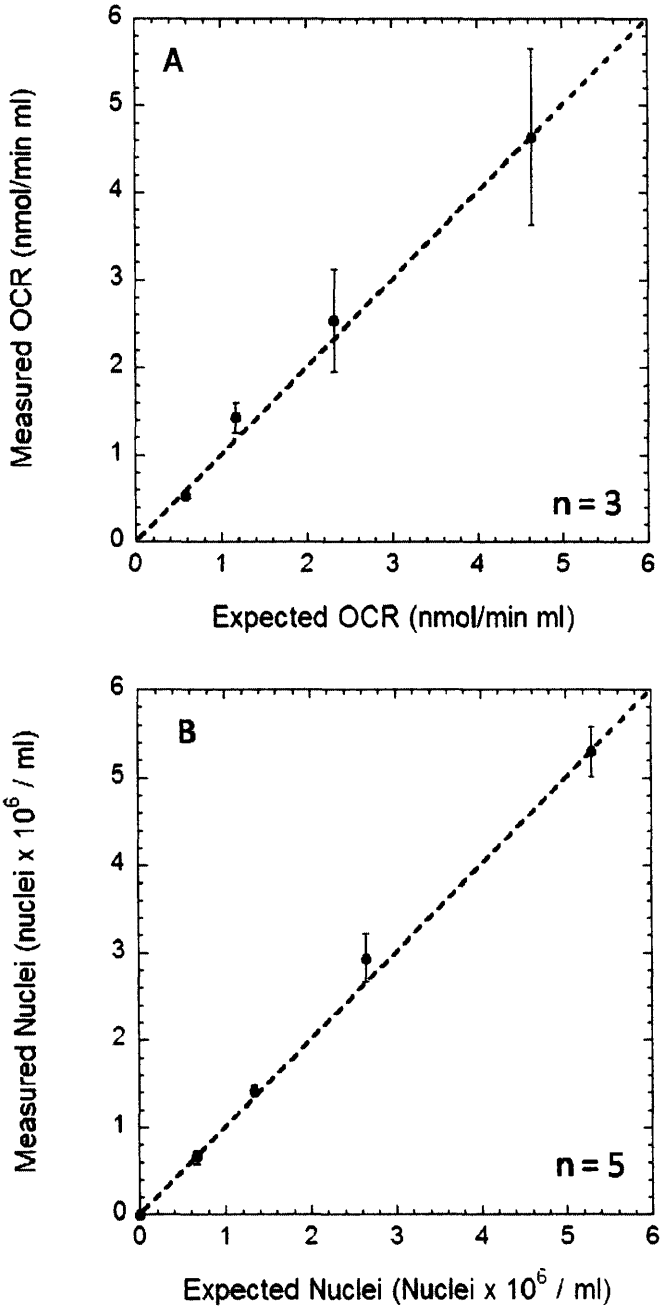

Figure 4.10. Dilutions plots to determine trustworthiness of dilution factors for (A) OCR measurements and (B) Nuclei measurements. Measurements for every dilution were performed and compared with expected results based on dilution factors (dashed, y = x line). Expected results were based on the largest actual measurement and then dividing by appropriate dilution factors. Data from fresh human islets 6/28/2008.

Plotting the stirred chamber OCR as a function of OBS maximum slope reveals a nearly linear relationship between the two measurements for both INS-1 cells (Figure 4.11A) and islets (Figure 4.11B).

As this relationship is an empirical observation, the least-squares fit line was not constrained to intercept the origin. Cell data were significantly tighter as can be seen by the low relative errors (standard error normalized by estimate) for both slope and intercept estimates, 2.1% and 12%, respectively. The relative errors associated with slope and intercept estimates for islet data were 5.5% and 61%, respectively.

Prediction intervals for the linear correlation were generated for both INS-1 (Figure 4.12A) and islets (Figure 4.12B). A 95% confidence level was used to determine the outermost interval, while a 68.3% confidence level determined the innermost interval. A confidence level of 68.3% was chosen because it represents the percentage of data falling within one standard deviation on either side of the mean of a normal distribution. The prediction intervals are not perfectly linear, but are tightest at the center of the data and begin to bow outward at the outer limits of data. This reflects the greater uncertainty with predicting data at the edges when data across the whole range was used to regress the least-squares fit. As expected, the prediction intervals are tighter for cells than they are for islets.

At every possible maximum slope value of the standard deviation prediction interval, the absolute difference between the OCR values of the standard deviation prediction and the least-squares fit was normalized by the OCR magnitude of the least-squares fit and termed the coefficient of variation. It is important to note that this is not a true coefficient of variation, which is based on experimental data (standard deviation normalized by the experimental mean), but is a analogous in the sense that the standard deviation prediction interval is similar to the standard deviation and the least-squares fit is similar to the mean. This coefficient of variation decreases sharply as the amount of viable tissue present increases (Figure 4.13) and is large for islet tissue.

The greater variability in islet measurements was most likely due to sampling variability. While islets do exhibit greater size and shape variability than cells, it is unlikely that geometric differences between islets caused substantial variability (see Chapter 2 for a discussion of how geometry does not significantly affect OBS results). Papas [18] demonstrated in stirred chamber measurements with islets, that the coefficient of variation sharply decreased when amount of viable islet tissue increased (Figure 4.14). The similarity between current data and Papas' data suggests that islet sampling is the primary source of variability and that a minimum threshold of viable tissue must be taken for any islet viability assessment to overcome the significant variability associated with low viable tissue.

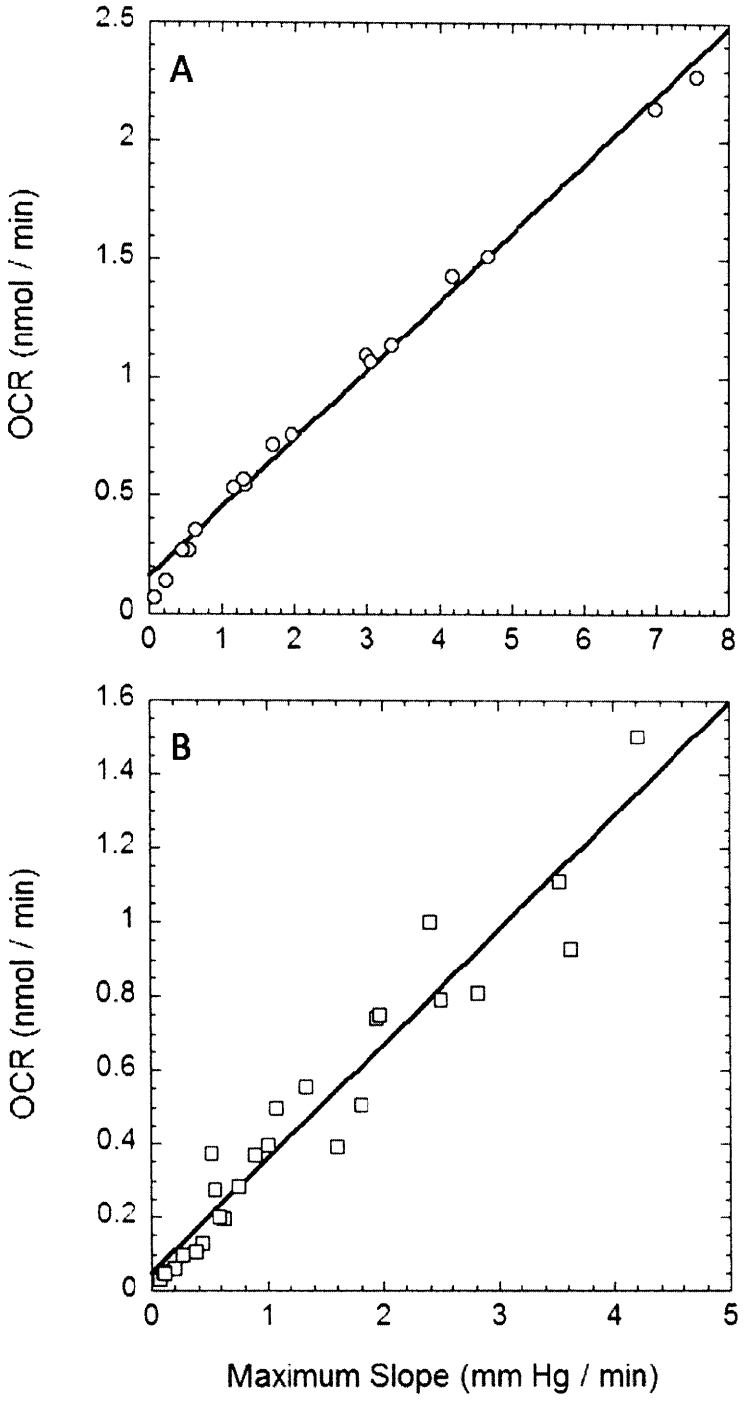

Figure 4.11. Correlation between OCR measured with stirred chamber and maximum slope measured with OBS for (A) INS-1 cells and (B) Islets. The least-squares fit for each data set gives the expression OCR = (0.290±0.006)Slope + (0.160±0.020) and OCR = (0.309±0.017)Slope + (0.051±0.031) for cells and islets respectively, where OCR is nmol/min and the maximum slope if mm Hg/min.

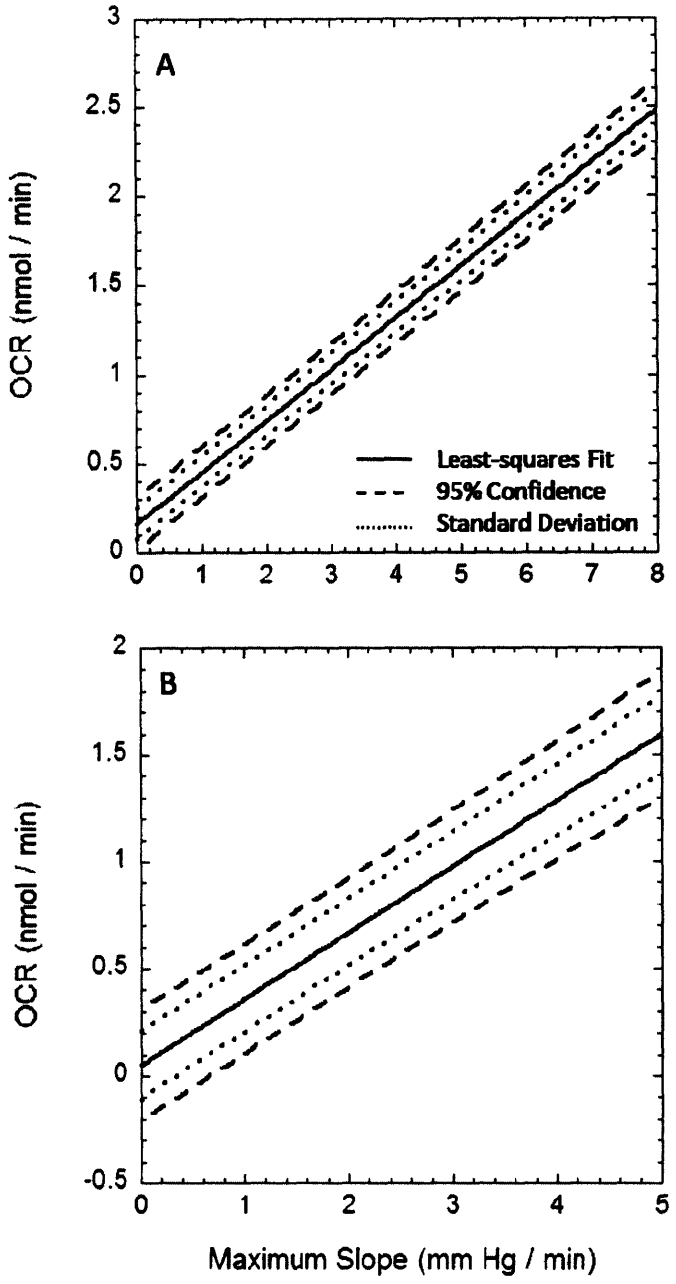

Figure 4.12. Prediction curves for (A) INS-1 cells and (B) islets. The least-squares fit is bounded first by the standard deviation (68% confidence) interval and subsequently by the 95% confidence interval. Prediction curves show the bounds (with an associated confidence level) for the next single measurement.

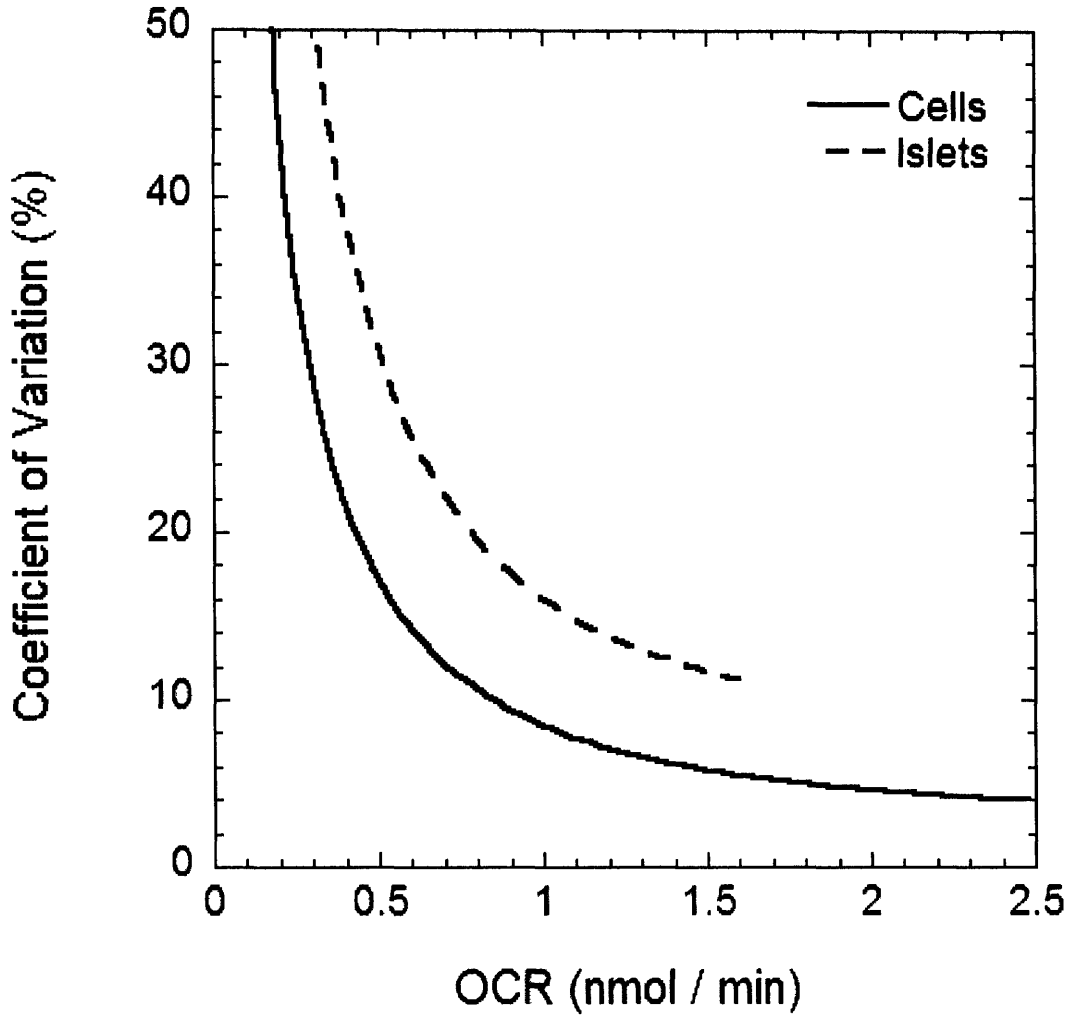

Figure 4.13. Coefficient of variation for islet and cell data where the standard deviation of the prediction interval was divided by the OCR value of the least-squares fit.

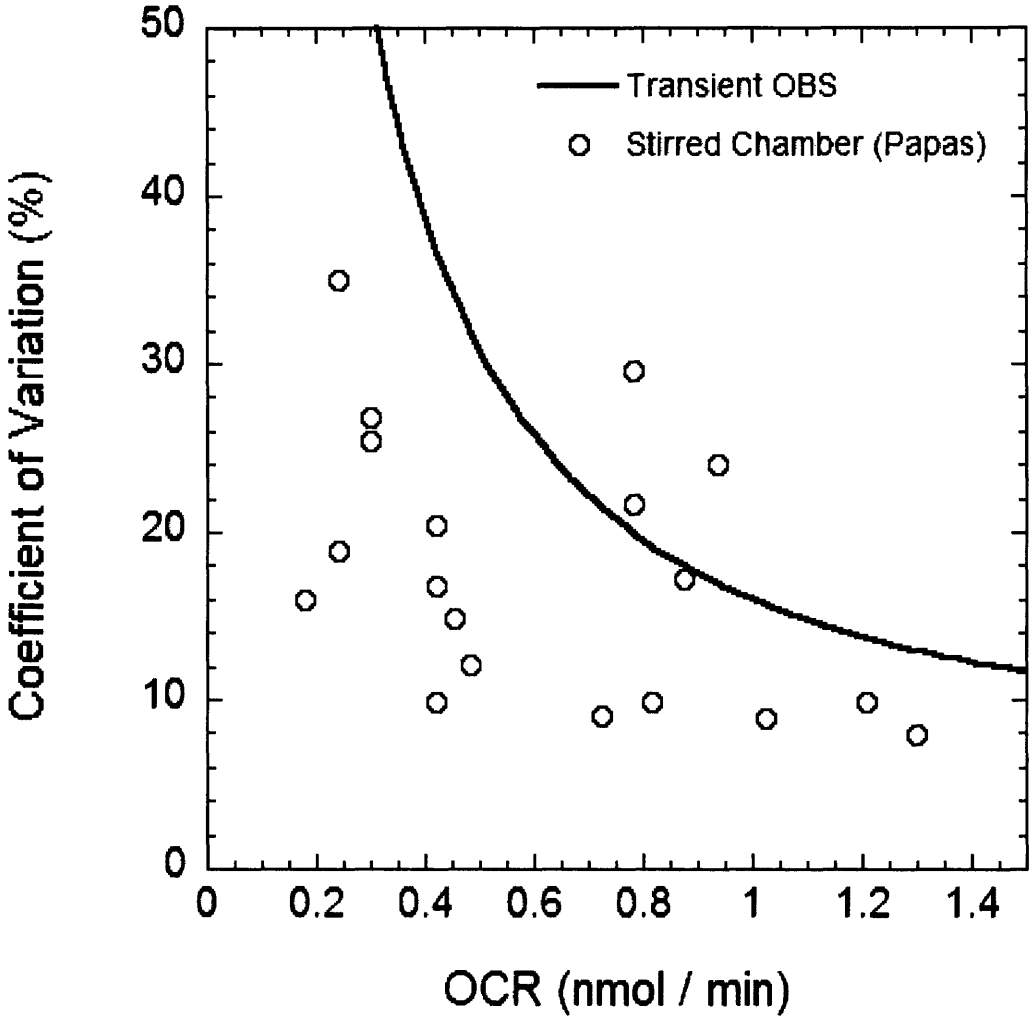

Figure 4.14. Coefficient of variation for two different islet tissue measurements. The COV for 'Transient OBS' was determined by dividing the standard deviation of the prediction interval by the value of the least-squares fit at that particular OCR value. As these values are determined from statistically regressed smooth lines, they yield a smooth curve. COV data from Papas, 2006 are from OCR measurements where the standard deviation (n=3) of the calculated linear slope was divided by the average calculated linear slope.

Plotting the least-squares fits at low OCR demonstrates that the difference between the empirical relationships for cells and islets increases as the amount of active tissue decreases (Figure 4.15). It is promising that cell and islet measurements are explained by the same empirical relationship, which is what we would expect if the tissue geometry can be ignored (see chapter 3 for a theoretical investigation of the effects of tissue thickness), provided that sufficient viable tissue is sampled.

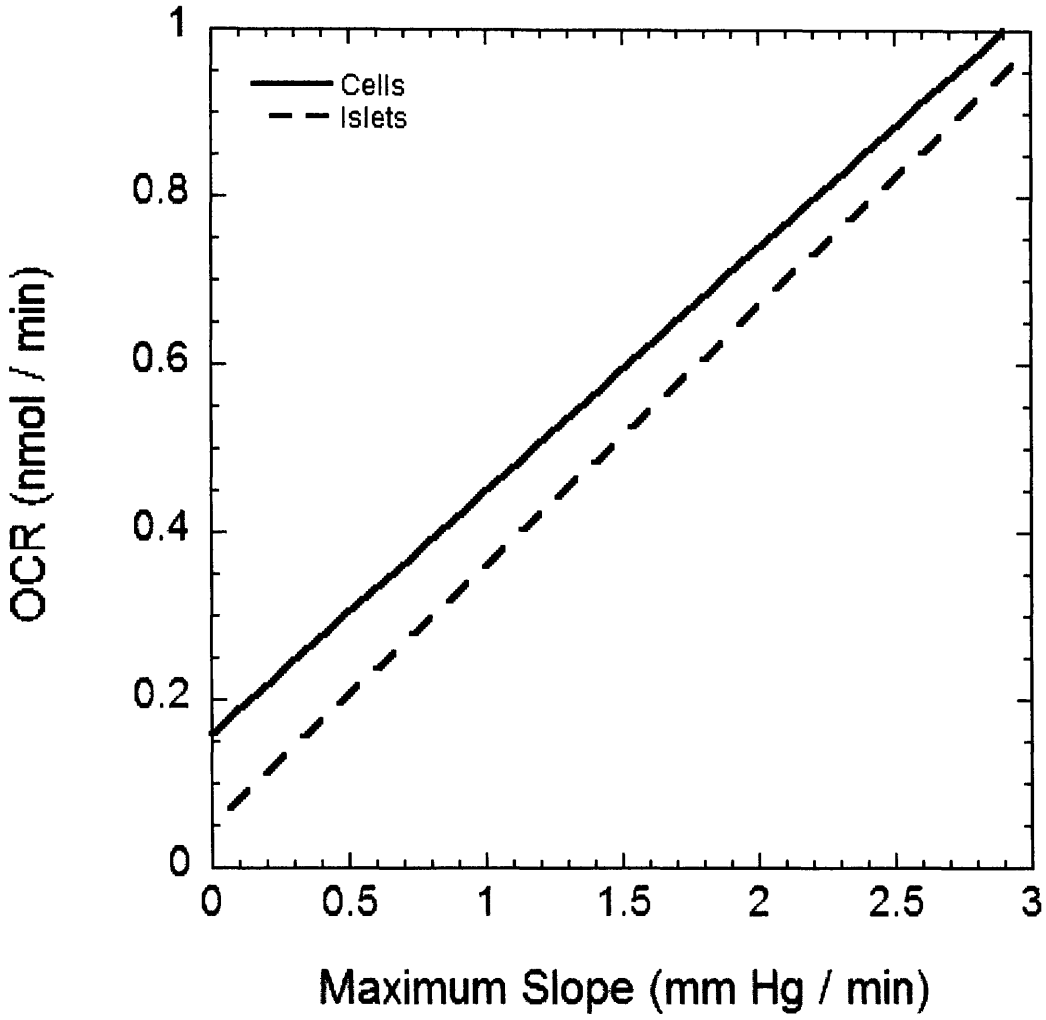

Figure 4.15. Least-squares fit for cells and islets. The region about the origin has been enlarged to demonstrate that at low OCR values, there is greater discrepancy between cell and islet correlations between maximum slope and OCR measurements.

A calibration plot was developed by fitting both cell and islet data (two cell data points beyond the highest limits of islet data were removed) and determining prediction intervals (Figure 4.16). Although clearly the islet tissue exhibited greater variability, both cells and islets demonstrated a similar empirical relationship between stirred chamber OCR measurement and maximum slope OBS measurement. The relative errors for the slope and intercept estimates are 3.5% and 32%, respectively.

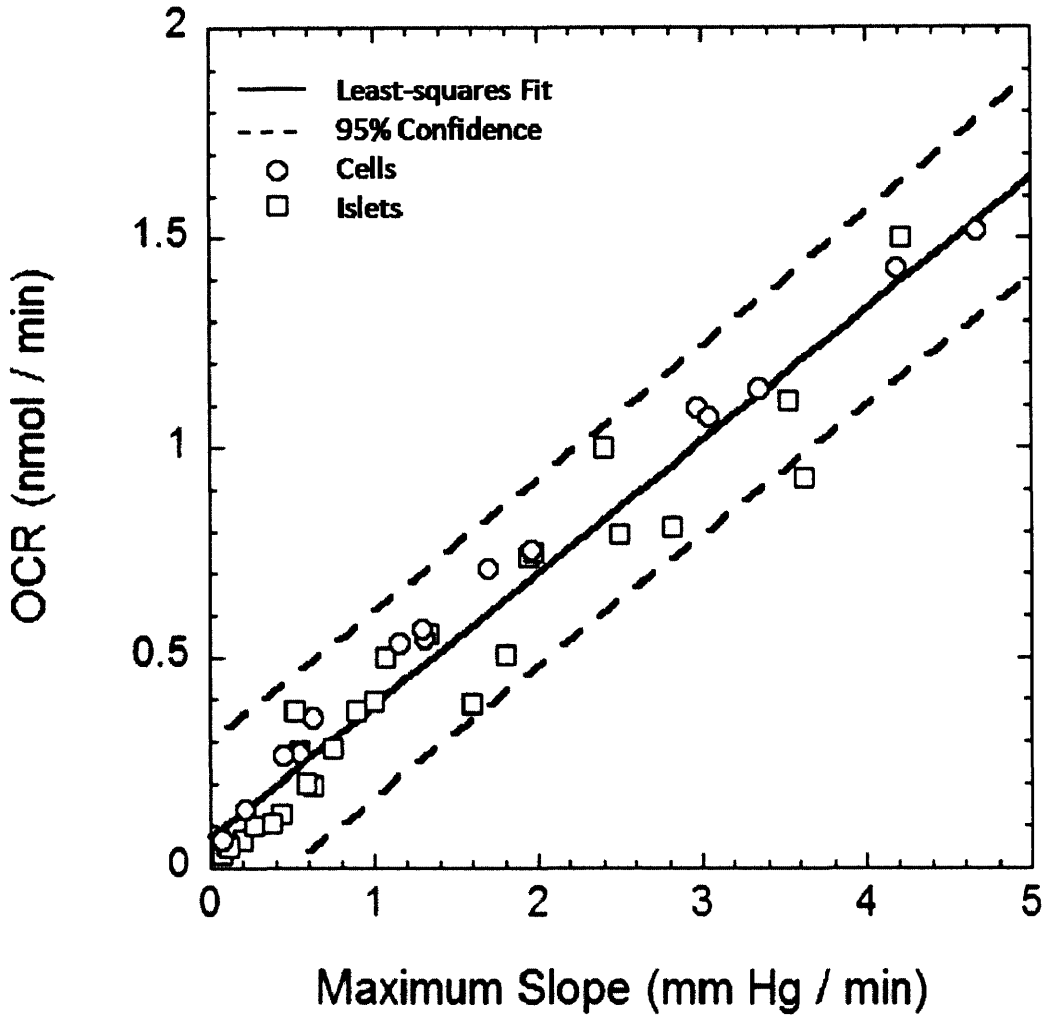

Figure 4.16. Correlation between OCR measured with stirred chamber and maximum slope measured with OBS for INS-1 cells and islets combined. The least-squares fit gives the expression OCR = (0.315±0.011)Slope + (0.071±0.023), where OCR is nmol/min and the maximum slope if mm Hg/min. The 95% confidence prediction interval is also plotted.

4.4 Discussion

In this study we have performed transient OBS experiments with INS-1 cells and both human and rat islet tissue and analyzed the transient pO_2 response in a more systematic approach to minimize errors associated with fitting a line to nonlinear data. The rate of pO_2 change lagged initially, reached a maximum within the first 20 - 60 min, and decreased until steady-state conditions were achieved. The

relative error associated with estimating the rate of pO_2 change was approximately 1% when analysis parameters were varied to determine optimal values. Ultimately it was shown that a simpler method of estimating the maximum rate of pO_2 change, by fitting data between 20 – 60 min (unless pO_2 reached 0 before 60 min had elapsed), produced similar results with far less time and resources for data analysis. The difference between the two methods was approximately 2%.

Data from stirred chamber OCR measurements were also subjected to a systematic analysis of the rate of pO_2 change and it was shown that the rate of change decreased 5 - 10% over the span of one single measurement. The relative error associated with estimating the rate of pO_2 change was minimized by spanning a large number of time points and was approximately 0.2%. Given that stirred chamber pO_2 data is more linear than OBS pO_2 data, it is not surprising that the relative error of estimating the rate of pO_2 change is approximately five times smaller for stirred chamber data.

Stirred chamber OCR measurements were conducted in parallel with transient OBS measurements and it was determined that the OCR and maximum OBS slope were linearly correlated. This empirical relationship is the first that correlates transient OBS measurements with a direct measure of OCR that is known to be accurate and enables us to generate a calibration curve where the output from a transient OBS experiment can be 'converted' to an accurate OCR measurement. This expands the potential application of OBS transient measurement of tissue from relative viability experiments requiring an experimental control, to absolute measurements of tissue viability.

Calibration curves for INS-1 cells and islets were sufficiently similar, that they could both be described by the same relationship. This suggests that OBS measurements are fairly insensitive to tissue geometry and dimensions and confirms similar theoretical findings (see Chapter 3). Although cells and islets followed the same calibration curve, islets exhibited significantly greater variability. The source of this variability was explored by comparing the current data with historical data obtained by Papas using the stirred chamber. The similar features of both data sets suggests that islet sampling is a fundamental source of variability in any islet viability assay and that sampling a sufficiently large amount of viable tissue significantly reduces this variability. Greater viable tissue also offers advantages that the maximum OBS slope is more pronounced (steeper maximum), less error associated with estimating maximum slope, and that the total time to conduct the experiment is reduced. These advantages are

offset by the higher tissue requirements, which is a significant consideration for islet quality assessment assays where islet tissue is limited.

5. Conclusions

This project was based on the hypothesis that transient OBS measurements of cells and islet tissue could accurately measure oxygen respiration as a marker of tissue viability in a high-throughput, convenient manner. The transient measurement was chosen because the long time necessary to reach steady-state in the OBS device makes steady-state measurements prohibitive for everyday use.

Rappel had previously evaluated several assumptions invoked to facilitate steady-state determination of OCR from pO_2 measurements with the use of theoretical steady-state models. Theoretical models were created to evaluate several of these assumptions in a transient model. The tissue thickness could effectively be ignored as in steady-state analysis, however, the silicone rubber thickness exerted a significant effect on transient behavior as opposed to steady-state where it could be ignored. Additionally, the curvature of both the silicone rubber and the air-medium interface were characterized and modeled to determine their effect on transient OBS experiments. It was concluded that the curvature of both interface has only a minor effect on the transient behavior and can effectively be ignored.

Flat OBS plates were fabricated to make actual geometry more closely resemble the assumed simple, 1-D geometry. The meniscus formed at the air-medium interface was removed by treating the polystyrene surface of the well to increase its hydrophobicity. Flat silicone rubber discs with embedded oxygen-sensitive fluorophor were fabricated, however, the discs could not seal sufficiently to either the sidewalls or bottom of the wall (or both) for the well to be experimentally useful. Dry, cell-free transient experiments with such flat silicone rubber plates did exhibit transient behavior that would be expected of 1-D, slab oxygen diffusion, suggesting that despite best efforts, wells were still not truly 1-D and that there existed alternate pathways for oxygen transport.

Additionally, a long and slow transient increase in pO_2 during dry, cell-free experiments was observed, which highlighted the primary difficulty of trying to model experimental data with theoretical OBS models. The complexity of even a dry, cell-free experiment is such that it is difficult to account for all the variables that influence transient OBS behavior. These, together with uncertain parameter values and potentially slow thermal equilibrations make it difficult to theoretically model behavior that matches closely with experimental data.

Theoretical models were developed to vary the silicone rubber height, liquid medium volume, and OCR density to evaluate their effects on transient behavior. By adjusting these parameters and qualitatively observing their effect it was possible to develop guidelines for transient OBS experiments that enable practical experiments and easy analysis of transient analysis.

When less silicone rubber is used, the transient response is faster and produces a steeper rate of pO_2 change that is easier to analyze. However, the rate of pO_2 change decreases rapidly for thin silicone rubber, whereas the rate of decrease is more constant (albeit smaller) for thicker slabs of silicone rubber. If the user is able fabricate his/her own OBS plates and control silicone rubber thickness then these tradeoffs between thick and thin silicone rubber must be considered. In most instances, the silicone rubber thickness is not adjustable and is determined by manufacturing specifications of the commercially-available OBS plate.

Greater medium volumes increases the likelihood that oxygen diffusion through the medium column is insufficient to meet the demands of tissue so that the measured pO_2 in the OBS well is 0. This will result in a steeper rate of pO_2 change and reduce the total time needed for measurement. It is recommended that at least 200ul medium be used for all transient OBS measurements.

Adding more viable tissue will cause a steeper pO_2 descent and reduce the time needed for measurement. Additionally, experimental data demonstrated that loading OBS wells with more tissue will reduce the coefficient of variation associated with any OCR prediction based on the transient OBS slope.

Experimental analysis of transient OBS data revealed that pO_2 does not decrease linearly, but has a maximum rate of decrease typically between 20 – 60 min. A systematic process was developed to determine the maximum rate of decrease while minimizing the error associated with estimating this maximum decrease, however, when compared with a significantly more straightforward method of estimating the slope, the two approaches were nearly indistinguishable from one another. Therefore, estimating the maximum slope by fitting data between 20 – 60 min is a good approximation of the maximum transient slope that requires very little time or effort.

Maximum OBS slope data were shown to linearly correlate with stirred chamber OCR data. A calibration curve was generated for both INS-1 cells and islets so that OBS measurements can be

converted into accurate, absolute measurements of OCR. The uncertainty associated with the calibration curve was larger for islet tissue and demonstrated to exhibit similar behavior to previously published data of stirred chamber measurement uncertainty. The uncertainty of any islet viability assay is caused by the difficult of sampling a small number of islets from a non-uniform solution of islets. The magnitude of this uncertainty can be decreased by sampling larger amounts of islet tissue when performing viability assays.

References

1. Pisania, A., *Development of Qualitative Methods for Quality Assessment of Islets of Langerhans*, in *Chemical Engineering*. 2007, Massachusetts Institute of Technology: Cambridge.
2. Papas, K.K., et al., *Human Islet Oxygen Consumption Rate and DNA Measurements Predict Diabetes Reversal in Nude Mice.* Am J Transplant, 2006.
3. Shapiro, A.M.J., et al., *Strategic opportunities in clinical islet transplantation.* Transplantation, 2005. **79**(10): p. 1304-1307.
4. Shapiro, A.M.J., et al., *Islet transplantation in seven patients with type 1 diabetes mellitus using a glucocorticoid-free immunosuppressive regimen.* New England Journal of Medicine, 2000. **343**(4): p. 230-238.
5. Knazek, R., *The human pancreatic islet cell resource consortium.* Diab Technol Ther, 2002. **4**(4): p. 551-552.
6. Weber, D., M. RD, and I. Irony, *Selected Food an Drug Administration review issues for regulation of allogeneic islets of Langerhans as somatic cell therapy.* Transplantation, 2002. **74**: p. 1816-1820.
7. Ricordi, C., et al., *Requirements for success in clinical islet transplantation.* Transplantation, 2005. **79**: p. 1298-1300.
8. Hedeskov, C., L. Hertz, and C. Nissen, *The effect of mannoheptulose on glucose-and pyruvate-stimulated oxygen uptake in normal mouse pancreatic islets.* Biochim Biophys Acta, 1971. **261**: p. 388-397.
9. Hellerstrom, C., *Oxygen consumption of isolated pancreatic islets of mice studies with the cartesia-diver micro gasometer.* Biochem J, 1966. **98**(1): p. 7C-9C.
10. Hellerstrom, C., *Effects of carbohydrates on the oxygen consumption of isolated pancreatic islets of mice.* Endocrinology, 1967. **81**(1): p. 105-112.
11. Welsh, M., C. Hellerstrom, and A. Andersson, *Respiration and insulin release in mouse pancreatic islets of mice. Effects of L-leucine and 2-ketoisocaproate in combination with D-glucose and L-glutamine.* Biochim Biophys Acta, 1982. **721**: p. 178-184.
12. Hutton, J.C. and W.J. Malaisse, *Dynamics of O2 consumption in rat pancreatic islets.* Diabetologia, 1980. **18**: p. 395-405.
13. Papas, K.K., et al., *Towards the development of a bioartificial pancreas: I. Effects of glucose on long-term entrapped βTC3 cell cultures.* Biotechnol Bioeng, 1999. **66**(4): p. 219-230.
14. Papas, K.K., et al., *Towards the development of a bioartificial pancrease: II. Effects of oxygen on long-term entrapped BTC3 cell cultures.* Biotechnol Bioeng, 1999. **66**(4): p. 231-237.
15. Panten, U. and H. Klein, *O2 consumption by isolated pancreatic islets, as measured in a microincubation system with a Clark-type electrode.* Endocrinology, 1982. **111**: p. 1595-1600.
16. Dionne, K.E., C.K. Colton, and L. Yarmush, *A microperifusion system with environmental controls for studying insulin secretion by pancreatic tissue.* Biotechnol Prog, 1991. **7**: p. 359-368.
17. Sweet, I.R., et al., *Regulation of ATP/ADP in pancreatic islets.* Diabetes, 2004. **53**: p. 401-409.
18. Papas, K.K., et al., *A stirred microchamber for oxygen consumption rate measurements with pancreatic islets.* Biotechnol Bioeng, 2007. **98**(5): p. 1071-82.
19. Alderman, J., et al., *A low-volume platform for cell-respirometric screening based on quenched-luminescence oxygen sensing.* Biosens Bioelectron, 2004. **19**(11): p. 1529-35.

20. Deshpande, R.R. and E. Heinzle, *On-line oxygen uptake rate and culture viability measurement of animal cell culture using microplates with integrated oxygen sensors.* Biotechnol Lett, 2004. **26**(9): p. 763-7.
21. Deshpande, R.R., et al., *Microplates with integrated oxygen sensors for kinetic cell respiration measurement and cytotoxicity testing in primary and secondary cell lines.* Assay Drug Dev Technol, 2005. **3**(3): p. 299-307.
22. Hutter, B. and G.T. John, *Evaluation of OxoPlate for real-time assessment of antibacterial activities.* Curr Microbiol, 2004. **48**(1): p. 57-61.
23. Hynes, J., et al., *Fluorescence-based cell viability screening assays using water-soluble oxygen probes.* J Biomol Screen, 2003. **8**(3): p. 264-72.
24. John, G.T., et al., *Integrated optical sensing of dissolved oxygen in microtiter plates: a novel tool for microbial cultivation.* Biotechnol Bioeng, 2003. **81**(7): p. 829-36.
25. O'Riordan, T.C., et al., *A cell viability assay based on monitoring respiration by optical oxygen sensing.* Anal Biochem, 2000. **278**(2): p. 221-7.
26. Papkovsky, D.B., T. O'Riordan, and A. Soini, *Phosphorescent porphyrin probes in biosensors and sensitive bioassays.* Biochem Soc Trans, 2000. **28**(2): p. 74-7.
27. Ramanathan, A., C. Wang, and S.L. Schreiber, *Perturbational profiling of a cell-line model of tumorigenesis by using metabolic measurements.* Proc Natl Acad Sci U S A, 2005. **102**(17): p. 5992-7.
28. Wodnicka, M., et al., *Novel fluorescent technology platform for high throughput cytotoxicity and proliferation assays.* J Biomol Screen, 2000. **5**(3): p. 141-52.
29. Guarino, R.D., et al., *Method for determining oxygen consumption rates of static cultures from microplate measurements of pericellular dissolved oxygen concentration.* Biotechnology and Bioengineering, 2004. **86**(7): p. 775-787.
30. Dike, L.E., et al., *Rapid method for assessing oxygen consumption rate of cells from transient-state measurements of pericellular dissolved oxygen concentration.* Cytotechnology, 2005. **49**(2-3): p. 133-141.
31. Fraker, C., et al., *The use of the BD oxygen biosensor system to assess isolated human islets of langerhans: oxygen consumption as a potential measure of islet potency.* Cell Transplant, 2006. **15**(8-9): p. 745-58.
32. Wang, W., et al., *Increased oxygen consumption rates in response to high glucose detected by a novel oxygen biosensor system in non-human primate and human islets.* J Endocrinol, 2005. **185**(3): p. 445-55.
33. Jorjani, P. and S.S. Ozturk, *Effects of cell density and temperature on oxygen consumption rate for different mammalian cell lines.* Biotechnol Bioeng, 1999. **64**(3): p. 349-56.
34. Rappel, M.J., *Maintaining Islet Quality During Culture*, in *Chemical Engineering*. 2007, Massachusetts Institute of Technology: Cambridge.
35. Gupta, M. and K.K. Gleason, *Initiated chemical vapor deposition of poly(1H,1H,2H,2H-perfluorodecyl acrylate) thin films.* Langmuir, 2006. **22**(24): p. 10047-52.
36. Wilson, D.F., et al., *The oxygen dependence of mitochondrial oxidative phosphorylation measured by a new optical method for measuring oxygen concentration.* J Biol Chem, 1988. **263**(6): p. 2712-8.
37. Avgoustiniatos, E.S., *Oxygen diffusion limitations in pancreatic islet culture and immunoisolation*, in *Chemical Engineering*. 2001, Massachusetts Institute of Technology: Cambridge.
38. Colton, C.K. and R.F. Drake, *Effect of boundary conditions on oxygen transport to blood flowing in a tube.* Chemical Engineering Progress Symposium Series, 1971. **67**(114): p. 88-95.

39. Devore, J.L., *Probability and Statistics for Engineering and the Sciences*. 5th ed. 2000, Pacific Grove, CA: Duxbury.